



Norwegian University of
Science and Technology

Use of 3D models obtained with photogrammetric methods in an industrial mineral mine

Alicja Maria Wycisk

Civil and Environmental Engineering

Submission date: June 2016

Supervisor: Terje Skogseth, BAT

Co-supervisor: Erik Stabell Ludvigsen, GEO
Knut Ragnar Holm, BAT

Norwegian University of Science and Technology
Department of Civil and Transport Engineering



Report Title: Use of 3D models obtained with photogrammetric methods in an industrial mineral mine	Date: 28.06.2016		
	Number of pages (incl. appendices): 105		
	Master Thesis	x	Project Work
Name: Wycisk Alicja			
Professor in charge/supervisor: Terje Skogseth			
Other external professional contacts/supervisors: Erik Stabell Ludvigsen, Knut Ragnar Holm			

<p>Abstract:</p> <p>3D models in underground mine could become an alternative or addition for mine surveying works. Furthermore, the data could be collected by less specialized mine workers, while generated photogrammetric products support other disciplines in the mining sector.</p> <p>The primary subject of this thesis was to establish a method which could enable a monitoring progress of exploitation works in terms of mapping drifts using 3D models. The method provides essential information about the direction in which drifts are excavated and enable to control the minimum distance between neighboring drifts before the next surveying measurements are conducted. First steps for establishing the method took place in a testing tunnel at NTNU and they consisted of setting up photo acquisition pattern and georeferencing 3D models. Among two cameras which were tested, GoPro camera was chosen as the most adequate to apply during a research in the mine. Moreover, there were two application Context Capture and Agisoft PhotoScan employed to produce 3D models. By comparison of the results between two programs, it was decided to use Context Capture for processing data captured in the mine. The test in NTNU tunnel showed some imperfections in data acquisition patter, thus some improvements were implemented.</p> <p>The research conducted in the mine proved that the method works in real conditions. Models presenting the situation in drifts were produced. Pictures taken before every blast allow us to prolong model and show the progress of exploitation works. However, due to many faces in production during the research period the accuracy of mapping was assessed only on a base of data captured for 3 blasts, which was close to the accuracy provided by total station measurements. For that reason, it was decided to conduct additional tests in an already excavated drift to obtain an accuracy indicator of mapping with 3D models concerning the longer part of a drift. The long model of the excavated drift was generated and the results brought surprisingly good accuracy for mapping 150 meters long drift.</p> <p>This master thesis also provides proposals of other applications of 3D models in underground mine connected to the mining operations. Especially, topics concerning geology such as structural analysis, geological interpretations, surveillance and documenting rock mechanics problems.</p>

Keywords:

1. 3D modelling
2. Underground mine
3. Mine surveing
4. Photogrammetry underground

MASTER DEGREE THESIS

Course TBA4925 Geomatics, master thesis

Spring 2016

for

Student: Alicja Maria Wycisk

**Use of 3D models obtained with photogrammetric methods
in an industrial mineral mine****BACKGROUND**

Recent technological developments in consumer cameras and in processing large data files open new methods for 3D modelling of underground mines. The actual underground mine is well suitable for testing different equipment and photogrammetric methods for georeferencing and building 3D models.

TASK

The candidate is going to investigate the use of modern photogrammetric methods in mining.

The main focus for the thesis is as follows:

If pictures covering the last part of a tunnel are taken just before starting drilling, and a georeferenced model is created from these pictures:

Is it possible to extend that model with new sets of pictures taken before the next blasts?

If so, how many sets of pictures can be joined before a new set of pictures have to be georeferenced?

The thesis will also demonstrate other applications connected to the mining operation, where the technology used in the main part can be applied.

Task description

Aspects to be examined are (key words), see below

Theoretical part: The candidate shall describe and discuss: Historical view on photogrammetric methods and developments and basic concept of digital photogrammetry.

Data capture and processing:

- *The test tunnel at NTNU:* Establish a method for the taking of the photos and for the georeferencing of the 3D models, check out the best choice of camera, where a super wide angle camera (GoPro) and a compact camera of high resolution are two of the most actual choices, and look into programs for developing the 3D models.
- *The underground mine:* Use the experience from the test tunnel and develop the methods further, if necessary. Use suitable programs to develop and produce the final 3D models, and for demonstrating other applications connected to the mining operation, such as geological applications.

Startup and submission deadlines

Startup: January 19th 2016. Submission date: Digitally in DAIM at the latest June 14th 2016 (prolonged to June 30th, owing to late start of the fieldwork).

Supervisors

Supervisor at NTNU: Terje Skogseth

Co-supervisors: Erik Stabel Ludvigsen, Department of geology, NTNU, and Knut Ragnar Holm, NTNU.

Department of Civil and Transport Engineering, NTNU. Date 19.01.2016 (revised June 2016).

Terje Skogseth
(signature)

Abstract

3D models in underground mine could become an alternative or addition for mine surveying works. Furthermore, the data could be collected by less specialized mine workers, while generated photogrammetric products support other disciplines in the mining sector.

The primary subject of this thesis was to establish a method which could enable a monitoring progress of exploitation works in terms of mapping drifts using 3D models. The method provides essential information about the direction in which drifts are excavated and enable to control the minimum distance between neighboring drifts before the next surveying measurements are conducted. First steps for establishing the method took place in a testing tunnel at NTNU and they consisted of setting up photo acquisition pattern and georeferencing 3D models. Among two cameras which were tested, GoPro camera was chosen as the most adequate to apply during a research in the mine. Moreover, there were two application Context Capture and Agisoft PhotoScan employed to produce 3D models. By comparison of the results between two programs, it was decided to use Context Capture for processing data captured in the mine. The test in NTNU tunnel showed some imperfections in data acquisition patter, thus some improvements were implemented.

The research conducted in the mine proved that the method works in real conditions. Models presenting the situation in drifts were produced. Pictures taken before every blast allow us to prolong model and show the progress of exploitation works. However, due to many faces in production during the research period the accuracy of mapping was assessed only on a base of data captured for 3 blasts, which was close to the accuracy provided by total station measurements. For that reason, it was decided to conduct additional tests in an already excavated drift to obtain an accuracy indicator of mapping with 3D models concerning the longer part of a drift. The long model of the excavated drift was generated and the results brought surprisingly good accuracy for mapping 150 meters long drift.

This master thesis also provides proposals of other applications of 3D models in underground mine connected to the mining operations. Especially, topics concerning geology such as structural analysis, geological interpretations, surveillance and documenting rock mechanics problems.

Acknowledgments

Many people were involved in this master thesis and I would like to express my sincere gratitude for all of them.

Firstly, I would like to thank my main supervisor, Terje Skogseth, for all his invested time, patience, motivation and encouragement to reach the goal.

I am grateful to my co-supervisor, Erik Stabell Ludvigsen, for providing me the possibility to do this thesis in the real conditions and also for the assistance and help during research period in the mine.

I would like to express my sincere gratitude to my co-supervisor, Knut Ragnar Holm, for all his advice concerning photogrammetry, and also for all those small talks about life.

I am grateful to my Polish supervisor, Agnieszka Malinowska, for giving me the inspiration to study and write this thesis abroad.

Finally, I would love to thank my parents, sisters and all close friends from Poland, but also those who I met here in Norway for providing me huge support and continuous encouragement throughout the process of researching and writing this thesis.

I would also like to acknowledge with great appreciation for the help with English always available from Matthew Peters.

Contents

1	Introduction	1
1.1	Background	1
1.2	Task description	3
1.3	Objectives of the study	4
2	Theory	5
2.1	Photogrammetry development	5
2.1.1	UAV in photogrammetry	6
2.2	Basic concept of digital photogrammetry	7
2.2.1	Interior orientation	8
2.2.2	Exterior orientation	8
2.3	Data acquisition practices	9
2.3.1	Field of view (FOV)	10
2.3.2	Camera resolution and Ground Sampling Distance (GSD)	11
2.3.3	Object distance	11
2.3.4	Photo overlap	12
3	Designing the image acquisition plan	13
3.1	Equipment	13
3.1.1	GoPro Hero 4 Black	14
3.1.2	Sony Alpha NEX-3	15
3.2	Camera calibration	16
3.3	Evaluation of the overlap and the ground distance between camera stations	17
3.3.1	Theoretical approach	17
3.3.2	Practical approach	18
3.3.3	Conclusions	20
3.4	Camera settings test	21
3.4.1	GoPro Hero 4 Black	21
3.4.2	Sony Alpha NEX-N3	24
4	Test in NTNU tunnel	26
4.1	Description	26
4.2	Data capture	27

4.2.1	Location and measurement of targets	27
4.2.2	Image capture	29
4.3	Data processing	32
4.3.1	Agisoft PhotoScan software	32
4.3.2	Context Capture software	34
4.4	Results	35
4.4.1	GoPro camera	35
4.5	Final comments	41
5	Test in the mine	44
5.1	Camera settings tested in the mine	44
5.2	Mapping the progress of exploitation works	46
5.2.1	Description	46
5.2.2	Ground Control Points	47
5.2.3	Surveying	47
5.2.4	Data capture	50
5.2.5	Data processing	52
5.2.6	Results - Drift A	55
5.2.7	Results - Drift B	60
5.2.8	Comments	65
5.3	Mapping the already excavated drift	66
5.3.1	First attempt	66
5.3.2	Second attempt	69
5.3.3	Results and comments	70
5.4	Use of 3D models in other disciplines	76
5.4.1	Geological mapping and inspection	76
5.4.2	Documenting rock mechanics problems	79
5.5	Final comments	82
5.6	Future recommendations	84
	Appendices	87
	A GoPro calibration report from Agisoft PhotoScan	88
	B Sony calibration report from Agisoft PhotoScan	89
	C Report of targets network adjustment in GISLINE software	90

List of Figures

1.1	Illustration of the mining method applied in the industrial mineral mine	2
2.1	Panorama of San Francisco after the earthquake and Lawrence’s kites. (Source: PAPA-International (2016))	5
2.2	(1) Microdrone MD4-200 (Remondino et al. (2011)), (2) SUBARU RPH2 (Nagai et al. (2002))	6
2.3	Collinearity	7
2.4	Triangulation	7
2.5	Relationship between measuring system and photo coordinate system	8
2.6	Relation between image and Ground Coordinate System	9
2.7	Field of view with two components: horizontal width and vertical view	10
2.8	The relation between data acquisition parameters	11
2.9	Overlap between two photos (O - overlap[%], W - horizontal width of photo, B - distance between cameras, od - overlap distance)	12
3.1	The pictures used in camera calibration for the GoPro (left image) and the Sony (right image)	16
3.2	The comparison of practical horizontal width obtained in the field work with theoretical values for both cameras	20
3.3	The differences in the image between ISO values: 1) ISO 800 2) ISO 400 3) ISO 100	22
3.4	<i>White Balance</i> options: 1) 3000K 2) 5500K 3) 6500K 4) NATIVE	23
3.5	<i>Color</i> options: 1) GOPRO 2) FLAT	23
3.6	<i>Sharpness</i> options: 1) LOW 2) MEDIUM 3) HIGH	24
4.1	Imitation of the front face in the NTNU tunnel	27
4.2	Sketch of the targets’ location in the NTNU tunnel	28
4.3	The locations of the photo stations represented by one photo set	30
4.4	The locations of the photo stations represented by two overlapping sets of images	31
4.5	The sparse point clouds and the cameras’ positions for GoPro (1) and Sony (2) photo sets generated by Agisoft PhotoScan	33
4.6	3D mesh model produced from photos captured with GoPro provided by Context Capture	36

4.7	Residuals on the Check Points from photos captured with GoPro provided by Context Capture	36
4.8	3D mesh model produced from photos captured with GoPro provided by Agisoft PhotoScan	37
4.9	Residuals on the Check Points from photos captured with GoPro provided by Agisoft PhotoScan	38
4.10	Warning information about reconstruction process failure appearing in Context Capture	39
4.11	3D mesh model produced from photos captured with Sony provided by Context Capture	39
4.12	3D mesh model generated from photos captured with Sony provided by Agisoft PhotoScan	40
4.13	Residuals on the Check Points from photos captured with Sony provided by Agisoft PhotoScan	41
4.14	Top view of the spare point cloud presenting bending wall	41
5.1	White Balance comparison (1) AUTO (2) 3000K (3) 5500K (4) 6500K	45
5.2	ISO value comparison (1) ISO100 (2) ISO200 (3) ISO400 (4) ISO527	45
5.3	Approximate dimensions of drifts in the mine	46
5.4	Location of Ground Control Points in the drift	47
5.5	The equipment used during the measurement on the known points . .	48
5.6	The fix point with the prism mounted on the bolt	48
5.7	The location of fix points (FM7002 and FM7003) and Ground Control Points (10-17) in Drift A	49
5.8	The location of fix points (FM7000 and FM7001) and Ground Control Points (20-27) in Drift B	49
5.9	The mobile drilling rig with LED lamps	50
5.10	Positions of each camera explaining the images acquisition pattern . .	51
5.11	The drilling rig's location as a reference to acquire new sets of photos	52
5.12	3D view generated in Context Capture after the <i>Aerotriangulation</i> process	53
5.13	3D view generated in Context Capture after <i>Aerotriangulation</i> process consisting of two sets of photos	54
5.14	The inside view of the first model in Drift A	55
5.15	The outside view of the first model in Drift A	56
5.16	The inside view of the second model in Drift A	56
5.17	The outside view of the second model in Drift A	57
5.18	The difference between the first and the second model of Drift A showing progress of exploitation works (top view)	57
5.19	The location of Check Points in Drift A	58
5.20	Vectors presenting the residuals on the Check Points in Drift A . . .	59
5.21	The inside view of the first model in Drift B	60
5.22	The inside view of the second model in Drift B	60
5.23	The inside view of the third model in Drift B	61

5.24	The difference between the three models of Drift B showing progress of exploitation works after each blast (top view)	62
5.25	The location of Check Points in Drift B	63
5.26	Vectors presenting the residuals on the Check Points in Drift B	64
5.27	The data acquisition pattern performed during the first attempt	67
5.28	Model presenting the left side of the drift	68
5.29	Model presenting the right side of the drift	68
5.30	Low-quality texturing due to poor light conditions	68
5.31	Setup of the LED lamps during the second attempt	69
5.32	Data acquisition pattern during the second attempt	70
5.33	Top view of the drift's model with Check Points' location	71
5.34	Side view of the drift's model	71
5.35	Inside view of the drift's model	72
5.36	Another inside view of the drift's model	72
5.37	Location of the Check Points in the drift	73
5.38	Vectors presenting the residuals on the Check Points in the drift	74
5.39	Plane portraying approximate course of biotite layer	77
5.40	Direct measurement of the layer's thickness	77
5.41	3D models provide information about lithology	78
5.42	Fault consisting of biotite layer	78
5.43	Recumbent fold presented on the 3D model	79
5.44	Identifying loosed bolts on the ceiling	80
5.45	Joints clearly visible on the ceiling	80
5.46	The way of taking pictures for the pillar's model	81
5.47	Pillar's 3D mesh model	81
5.48	Loosened rocks stand out from the pillar's surface	82

List of Tables

3.1	Specification of GoPro Hero 4 Black (Source: CNET (2016a))	14
3.2	Specification of Sony Alpha NEX-3 (Source: CNET (2016b))	15
3.3	The results of camera calibration	17
3.4	Theoretical FOV of single photo	17
3.5	The base distance for theoretical values of horizontal width when distance from the object = 5 m	18
3.6	The base distance for theoretical values of horizontal width when distance from the object = 7.5 m	18
3.7	The base distance for theoretical values of horizontal width when distance from the object = 10 m	18
3.8	The real values of the horizontal width obtained in the field work . .	19
3.9	The base distance for practical values of horizontal width when distance from the object = 5 m	19
3.10	The base distance for practical values of horizontal width when distance from the object = 7.5 m	19
3.11	The base distance for practical values of horizontal width when distance from the object = 10 m	20
3.12	ISO value and Mode settings of GoPro camera	22
3.13	Test of the GoPro ProTune Settings	23
3.14	Sony settings test	25
4.1	The numbers of images included in the separate photo sets	31
5.1	The residuals on the Check Points in Drift A	58
5.2	The residuals on the Check Points in Drift B	64
5.3	The residuals on the Check Points in the drift	73

Chapter 1

Introduction

3D models are commonly used in a wide variety of fields, from the medical industry, through architecture, to construction projects such as buildings, bridges, tunnels, and the mining industry. Conventional methods used in mining surveying are considered time consuming, high-priced, require professional equipment and operators. Poor light conditions in underground mines also bring skeptical attitudes in terms of implementing digital photogrammetry methods. However, due to economical reasons and time saving factors, there is a need for inventory techniques which could reduce costs and the workload of the mine surveyor's. The recent developments in camera technology, data processing acceleration, and memory capacity of computers have brought new opportunities for using close range digital photogrammetry methods also in the mining sector. By applying specific software, it is possible to create a three-dimensional model from sets of overlapping photos which is efficient and reliable. As a result, the real dimensions and spatial geometry of geological structures of a drift or a tunnel could be obtained.

1.1 Background

The main idea for the theme of this thesis comes from an investigation into whether consumer electronics, which are inexpensive and easily accessible, can be used as a tool for 3D modelling in the underground mining industry. According to the Haugen and Ludvigsen (2015) :

Mining is conducted in three-dimensional space which makes 3D planning essential. Recent technological developments, especially related to consumer electronics, open new methods for 3D modelling. The geodetic basis for modelling has to be established by a specialized surveyor, but due to the technology that is now, the details for building the models can be captured by less specialized workers. Data should be captured when they appear, preferably by those present at that time and as a part of the working cycle.

The opportunity has arisen for testing capabilities of building 3D models by acquiring

data in real mine conditions. In this respect, the research was conducted in Norway and the place can be described as an ordinary industrial mineral mine. The topics presented in the thesis are universal for that type of mining. For not coming in conflict with the mine's confidentiality policy, information on the company, the location and the mining method is minimized.

The mining method used in this mine can be characterized as room and pillar. From a central ramp there are drifts driven towards both sides (See Figure 1.1). The direction of the ramp is controlled by geology, however there is a minimum distance between the drifts that should not be exceeded.

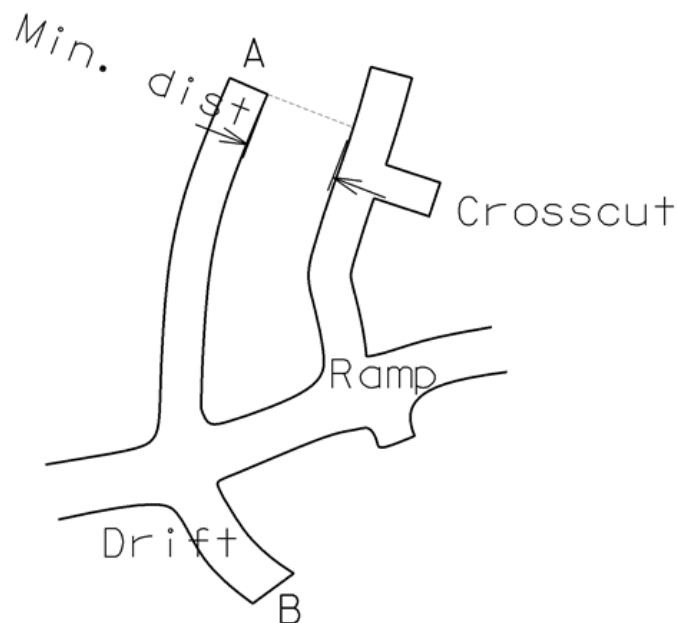


Figure 1.1: Illustration of the mining method applied in the industrial mineral mine

The surveying in the mine is performed in an ordinary way by prolonging traverses in the direction of the new drifts and the ramp with new points permanently mounted in the walls. The measurements are held with use of total station and prisms which enables mapping the course of each drifts' walls. In addition, some points on the floor are measured in order to verify the depth (height below sea level). The surveyor updates the mine map every 2-3 weeks or if some special needs appear.

The mine was available for the purpose of this research for a three-week period, only a month before the thesis had to be completed. To gain experience and find a way of performing in real situations, there was a need to run pre-tests in a test tunnel located in Trondheim at Gløshaugen (Norges teknisk-naturvitenskapelige universitet campus). The main purpose of these pre-tests was to become familiar with cameras and software as well as examining procedures concerning capturing photos and

georeferencing models. The description of the works is presented in Chapters 3 and 4.

An explanation of some of the terms implemented in this thesis are listed below:

- Drift - a horizontal opening in or near an ore body and parallel to the course of the vein or the long dimension of the ore body.
- Tunnel - a horizontal, or near-horizontal, underground passage, that is open to the surface at both ends.
- Crosscut - an entry perpendicular to the vein or the long dimension of the ore body.

1.2 Task description

The main focus for the thesis is as follows: If photographs covering the last part of a tunnel are taken just before starting drilling, and a georeferenced model is created from these pictures:

- Is it possible to extend that model with new sets of pictures taken before the next blasts?
- If so, how many sets of pictures can be joined before a new set of pictures have to be georeferenced?

The thesis will also demonstrate other applications connected to the mining operation, where the technology used in the main part can be applied.

In order to accomplish these tasks, two main parts of this thesis will be distinguished:

First, a method for capturing the photos and for the georeferencing of the 3D models were tested in the NTNU tunnel. In addition, the best choice of camera was examined including an ultra-wide angle camera (the GoPro), and a compact camera of high resolution (the Sony). Moreover, programs for developing the 3D models were investigated.

Second, applying the research from the test tunnel, and the improved method of data acquisition from the test tunnel in the final underground mine. With use of Context Capture, the final 3D models were produced, and demonstration of other applications connected to the mining operation, such as geological investigation, was portrayed.

1.3 Objectives of the study

- Establishing a practical method for a mine worker to map drifts with use of 3D models.
- Assessing the accuracy of the new method.
- Testing available software: Context Capture (Version: x64 04.01.00.514) and Agisoft PhotoScan (Version: x64 1.2.4.2399).
- Experimenting with cameras: GoPro Hero 4 Black and Sony Alpha NEX-C3.

Chapter 2

Theory

2.1 Photogrammetry development

The origin of photogrammetry can be traced back to the 1480 meanwhile Leonardo da Vinci developed the concept and the principle of perspective, and projective geometry. However, Daguerre's invention of photography in 1839 contributed to the fact that photogrammetry experienced a breakthrough. Fairly soon after, the first tryouts of aerial photography using balloons or kites were conducted, for instance, the devastation of San Francisco after the earthquake and fire was captured by George R. Lawrence, using a camera attached to a string of kites high above the city, as shown in Figure 2.1. In addition, Colonel Aime Laussedat was nicknamed the "Father of Photogrammetry", since he handled the first experiments for topographical mapping using photographs. A new epoch of modern aerial photogrammetry started in 1903, when the airplane was invented. The most significant developments of instruments, techniques, and equipment began with the digital age (Mikhail et al. (2001); Wolf and Dewitt (2000)).

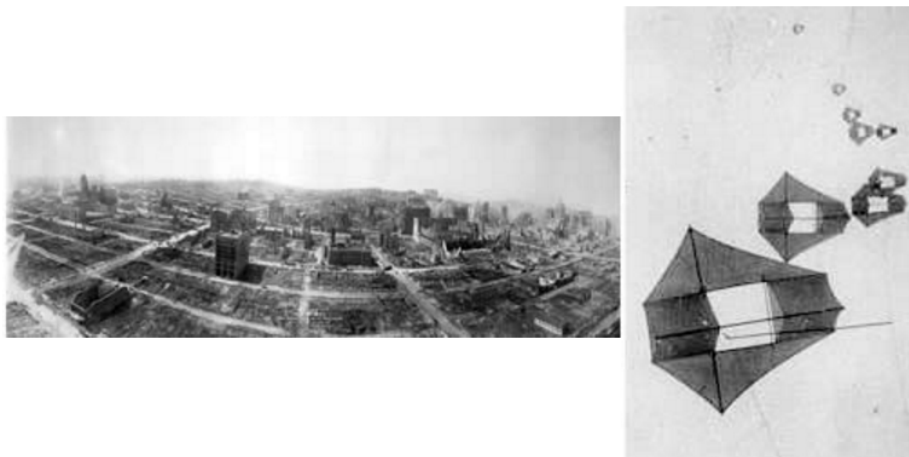


Figure 2.1: Panorama of San Francisco after the earthquake and Lawrence's kites. (Source: PAPA-International (2016))

The blistering pace of the technological progress is visible in various branches of geomatics, especially in digital elevation modelling. According to Westoby et al. (2012), due to rapid developments in traditional ground surveying, such as the advent of differential GPS measurements and robotic total stations, the acquisition of topographic data was revolutionized by a new approach to remote sensing technologies. The quality of Digital Elevation Models (DEMs) in terms of spatial extent, resolution, and accuracy was boosted thanks to terrestrial and airborne laser scanning. These methods became an incentive for the advancement of hydrographic surveying, including the use of single and multi-beam sonar scanning.

In addition, the practice of acoustic soundings to capture data spacing was used. The generated 3D point clouds became accurate enough to construct exact, continuous, and highly precise terrain models of mixed areas, both terrestrial and aquatic. Finally, in recent history, the most revolutionary method of obtaining photogrammetric data appeared by deploying different types of imaging sensors on low-priced, and lightweight, unmanned aerial vehicles called UAVs. A more detailed description of UAVs will be presented in Chapter 2.1.1.

2.1.1 UAV in photogrammetry

Colomina et al. (2008) notes that UAV brings a new angle of looking at applications in close-range photogrammetry as well as finding a new low-cost substitute for classical, unmanned aircraft. According to Eisenbeiß (2009), UAVs used in photogrammetry could be defined as a photogrammetric measurement platform, designed to be operated remotely without a pilot on board. Rapid development is mostly caused by production of low-cost platforms and mounting on them amateur cameras and GNSS/INS systems which enable navigating UAVs within the desired area of interest (Remondino et al. (2011)). These systems do not need to be so advanced and professional to provide data in order to generate photogrammetric products for instance, Digital Surface Model, Digital Terrain Model, textured 3D models, contour maps as well as for vector data. Moreover, by employing a more heavy, and stable UAV with a gasoline engine, it is possible to mount professional DSLR cameras or even LiDAR systems which enable highly precise surveying (Nagai et al. (2002)).



Figure 2.2: (1) Microdrone MD4-200 (Remondino et al. (2011)), (2) SUBARU RPH2 (Nagai et al. (2002))

2.2 Basic concept of digital photogrammetry

This thesis is dedicated to the group of people working in the mine, who are not so familiar with using photogrammetry as a measurement tool. The basics of photogrammetry would be practical for better understanding how the 3D models are obtained from the overlapping photos.

Digital photogrammetry starts with two fundamental principles:

1) The Collinearity principle - the assumption that the object point (T), the projection center (C), and the projected point (t) are collinear. In other words: Points lie on a straight line. The graphical representation is shown in Figure 2.3.

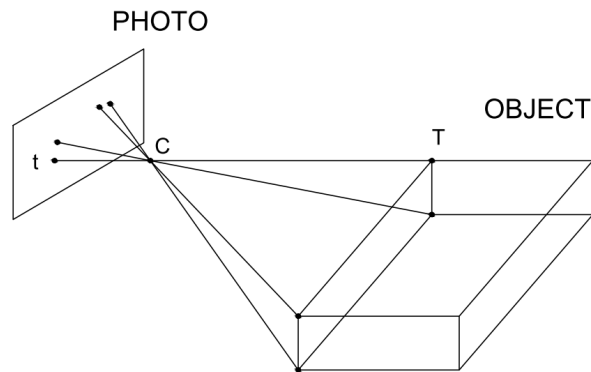


Figure 2.3: Collinearity

2) The Triangulation principle - one measurement of image coordinate (x,y) is too little to determine the object point coordinates (X,Y,Z). There is a need to have at least two measurements (two photos from different locations) of the same object point to obtain three dimensional coordinates of an object point. The graphical representation is shown in Figure 2.4.

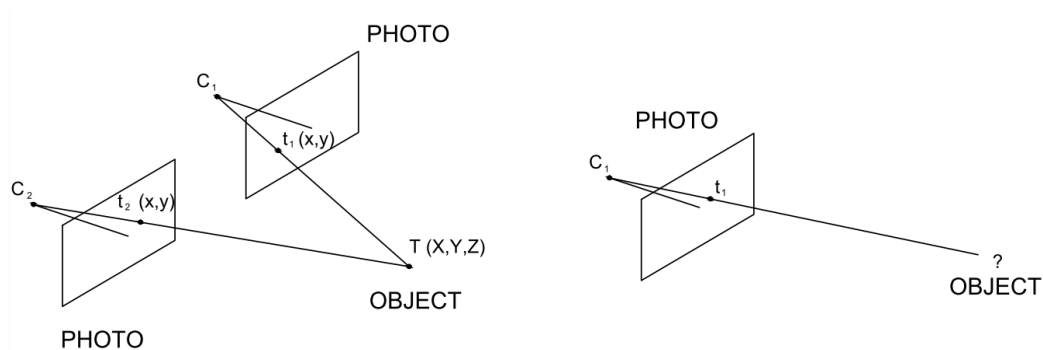


Figure 2.4: Triangulation

2.2.1 Interior orientation

According to Schenk (2005), the parameters of interior orientation are defined during camera calibration process. Kraus (2000) describes the parameters which can be listed as:

- 1) c - principal distance - the distance between the projection center, and the principal point of the photograph (called by Schenk (2005) as focal length), and
- 2) x_0, y_0 - image coordinates of the principal point.

In addition, as physical lenses are not perfect, the radial and discentering distortion of the lens is also treated as a parameter of interior orientation. All these parameters to be known to enable precise reconstructing of the bundle rays going through the projection center, image points ending up in the object space (real situation on the ground).

According to Kraus (2000), interior parameters define the location of the projection center with reference to the image plane. Due to the imperfect physics of the camera, it is impossible to measure photo coordinates directly on the photo. Main goal of determining these parameters is to set up a relations (to be specific a 2D transformation) between direct measurement on photo (measuring system) and the photo coordinate system (See Figure 2.5).

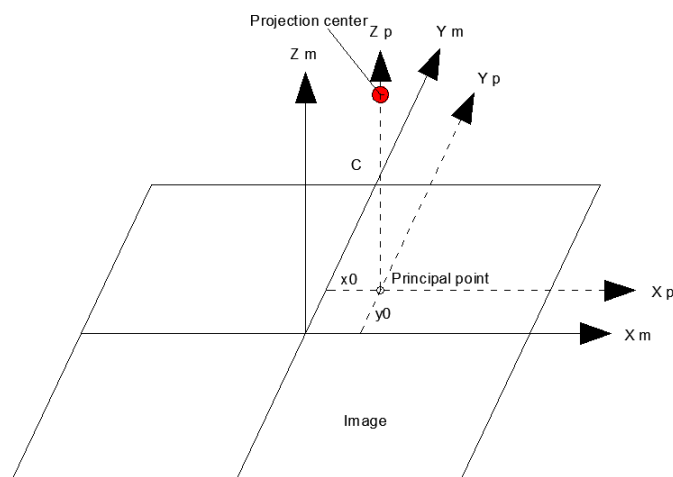


Figure 2.5: Relationship between measuring system and photo coordinate system

2.2.2 Exterior orientation

According to Elnima (2015): "exterior orientation of an image refers to its position and orientation related to an exterior coordinate system". Instead of "Exterior co-

ordinate system” in this case, Ground Coordinate System would be a more precise statement. Schenk (2005) notes it as a definition and relation between photo and object space (See Figure 2.6). According to Kraus (2000), there are six parameters of exterior orientation:

- 1) X_0 , Y_0 , Z_0 - coordinates of the camera position in Ground Coordinate System, and
- 2) ω , ϕ , κ - rotations of the photo.

The parameters of exterior orientation could be obtained directly by surveying, which is possible only in terrestrial photogrammetry. However, an alternative method would be indirectly applying Ground Control Points for which both coordinates in the Ground Coordinate System, and the image coordinates system need to be known.

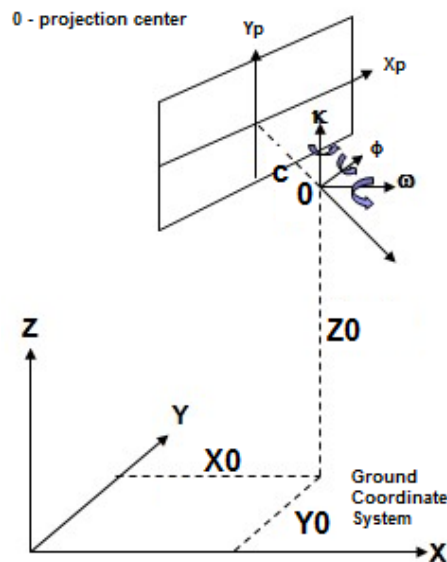


Figure 2.6: Relation between image and Ground Coordinate System

2.3 Data acquisition practices

Nevertheless, the technology of obtaining 3D models is today a highly automatized process. In this sense, it is extremely important to design an appropriate acquisition plan. The better coverage of photos, the better result obtained. However, the user should be aware that set of photos covering the same area could vary enormously in terms of processing cost. The higher number of photos acquired, the longer the processing time. Nevertheless, enough images must be captured to successfully reconstruct the object. The challenge is to find out the optimal solution concerning both.

As some of the parameters and statements will be used in this thesis, the terms will be described below, which is essential to explain them for better case understanding. The four fundamental parameters such as FOV, GSD, camera resolution, and object distance are closely related. The fourth parameter is determined by the rest of the three parameters. This chapter was written with the information obtained from website Geodetic Systems (2016).

2.3.1 Field of view (FOV)

FOV is a part of the scene which is visible through the camera at a distinct position and orientation in space. In photography, the field of view (FOV) is defined as a function of the focal length (f) and the size of the digital sensor(s):

$$FOV = \frac{sD}{f} \quad (2.1)$$

For a given size sensor, a longer focal length lens has a more narrow field of view. Equivalently, for a given lens, the larger the sensor, the larger the field of view becomes. In addition, FOV directly affects the number of photos which need to be taken in order to get sufficient overlap between photos, which is presented in Chapter 2.3.4. The illustration of FOV is shown in Figure 2.7.

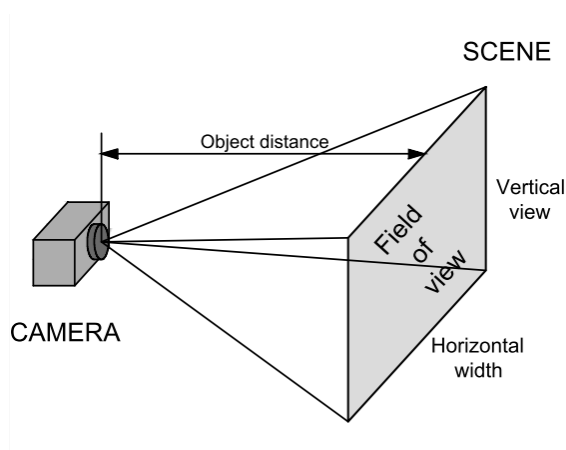


Figure 2.7: Field of view with two components: horizontal width and vertical view

There are various types of lenses available on the market, which could be divided into three groups: narrow, medium, and wide angle lenses. Practically, a dependency between the field of view of a lens and accuracy exists. Wide angle lenses need less space around the object, which is extremely useful in a tunnel or a drift. However, they tend to be less accurate due to larger distortion. Nowadays, many applications deal with that problem by reducing the negative effect of distorted photos with the help of mathematical algorithms.

2.3.2 Camera resolution and Ground Sampling Distance (GSD)

Camera resolution is essential in terms of obtaining more detailed 3D models. The higher camera resolution is available, the more precise results are gained. Moreover, it also allows the use of longer object distance, or an enlarged flight altitude for UAVs or airborne vehicles. Camera resolution is described as the size of the image in pixels, while knowing the linear extent of one pixel. As a result, the real size of the sensor is known as well.

To conduct the pre-assessment of the accuracy and quality of the photogrammetric product (such as point cloud or orthophotomap), Ground Sampling Distance (GSD) is crucial. A close relation between Field of View and Ground Sampling Distance exists since GSD is the distance between two consecutive pixel centers projected on the ground surface. For instance, GSD is equal to 10 cm if the single image pixel represents, in reality, 10 cm on the ground. The most common unit of GSD is centimeters per pixel or, for less accurate products, meters per pixel.

2.3.3 Object distance

The distance between an object being photographed and the lens of a camera is called object distance. Equivalently, in airborne photogrammetry or UAV, the name flight altitude is used. In most of the cases, the object distance is determined by the rest of the data acquisition parameters, since it requires the least effort to adapt. However, in the tunnel or mine drift environment due to space limitation, object distance will be determined in advance. The relation between object distance, focal length, size of sensor, and field of view is illustrated in Figure 2.8.

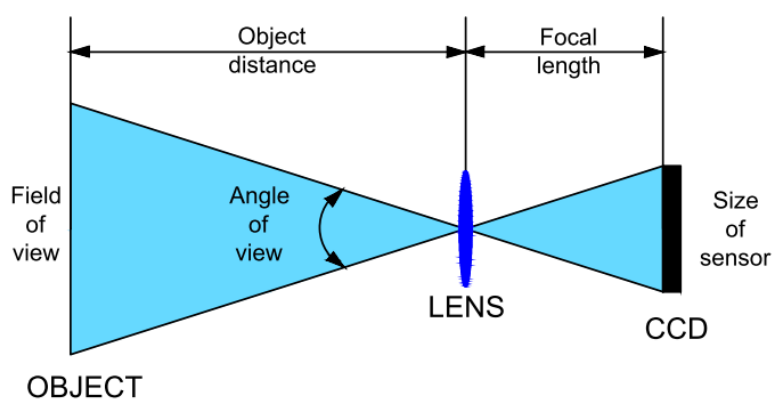


Figure 2.8: The relation between data acquisition parameters

2.3.4 Photo overlap

At least two photos of the same object need to be taken from different locations to obtain 3D information. There is significant influence on the certainty and accuracy of the computed geometry on the overlap between the photos (the higher the overlap, the better the accuracy). The 3D mapping algorithm demands for each point to be visible in multiple images in order to create a 3D model.

The overlap is the amount by which one photo includes the area covered by another photo. There are two kinds of the overlap which could be distinguished: forward overlap (between photos taken along the same direction or 'flight line') and sidelap (between neighboring rows). Both are quantified as percentage of horizontal width or vertical view (See Figure 2.7). The simple formulas to evaluate the overlap and the base between photos are presented below.

$$od = O * W \quad (2.2)$$

$$B = W - od \quad (2.3)$$

The illustration of two overlapping pictures and explanation of parameters used in the formulas are presented in Figure 2.9.

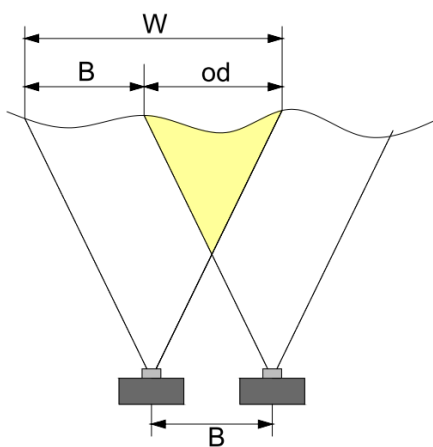


Figure 2.9: Overlap between two photos (O - overlap[%], W - horizontal width of photo, B - distance between cameras, od - overlap distance)

Chapter 3

Designing the image acquisition plan

In this chapter, the specification of cameras applied in the research will be presented. Some evaluations concerning overlap between photos determined for various object distances were performed, which gave indication about the base distance between camera positions, essential for data acquisition pattern. The values of the base distance will be separately presented for both cameras concerning theoretical and practical approaches. In addition, there were simple tryouts of camera settings conducted in order to set up cameras for the test in NTNU tunnel.

3.1 Equipment

Data acquisition was conducted by two different types of cameras: GoPro Hero 4 Black and Sony Alpha NEX-3. Detailed specification of the equipment is presented in Chapters 3.1.1 and 3.1.2. The main reasons for selection of these cameras were diverse focal length and Field of View (FoV). Due to the challenge concerning limited space and short distances between walls in a tunnel, wide angle lenses were demanded to cover as large an area as possible. Nevertheless, optical design of wide angle lenses causes optical distortion that deforms and bends physically straight lines and transforms them into curvy images, which could have affected the results of 3D models. Accordingly, it seemed to be reasonable to use both fisheye and frame cameras in the research to observe how various software handle the problem.

The aim of the study is to obtain a low-cost method, instead of employing professional and costly cameras. In order to achieve this, low-budget and easily accessible cameras were implemented. In addition, sport cameras, such as the GoPro Hero 4 Black, are well adjusted to work in harsh conditions, such as in dust, water, and moisture, which are prevalent in underground mines. The short names for cameras are used in this thesis as *GoPro* for GoPro Hero 4 Black, and *Sony* for Sony Alpha NEX-C3.

3.1.1 GoPro Hero 4 Black

The newest and the most efficient model of GoPro cameras available on the market. The manufacturer adopted the processor, which is twice more powerful to compare with the previous version of the camera. As a result, video recordings might be conducted in 4K(Ultra HD) resolution at 30 frames per second. In addition, SuperView mode enables the camera to maximize its sensor area to obtain an ultra-wide angle of view. Moreover, it takes 12-megapixel stills as individual shots in intervals to generate time-lapse movies. The camera is equipped with Wi-Fi and Bluetooth connectivity allowing remote operation with use of a mobile device, or the separately available Smart Remote. More precise specifications are given in Table 3.1.

Table 3.1: Specification of GoPro Hero 4 Black (Source: CNET (2016a))

GENERAL	
Optical Sensor Type	CMOS
Wireless Connection	Bluetooth, Wireless LAN
Image Recording Format	JPEG
Interfaces Provided	HDMI, composite video/audio
Max Video Resolution	3840 x 2160
Interfaces Provided	Composite video/audio, HDMI
Effective Photo Resolution	12.0 MP
EXPOSURE & WHITE BALANCE	
Light Sensitivity	ISO 100, ISO 200, ISO 400, ISO 800
Exposure Metering	spot
Exposure Modes	automatic
Special Effects	Flat
White Balance	automatic, presets
White Balance Presets	3000K, 5500K, 6500K
Min Shutter Speed	30 sec
CARRYING CASE	
Underwater Depth	up to 131.2 ft
LENS SYSTEM	
Type	Wide-angle lens
Mode: 4 x 3 Wide	Vertical FOV 94.4 deg Horizontal FOV 122.6 deg
Focus Adjustment	focus free
Features	distortion reduce
MISCELLANEOUS	
Protection	shockproof, waterproof
MEMORY	
Supported Memory Cards	microSD Card, microSDHC Card, microSDXC Card

Image Storage	JPEG 4000 x 3000, 3000 x 2250, 2560 x 1920
EXPOSURE PARAMETERS	
Exposure Metering	spot
Exposure Compensation	+/- 2 EV range, in 1/2 EV steps
Exposure Modes	automatic

3.1.2 Sony Alpha NEX-3

The Sony NEX-C3 is one of the small-sized, changeable-lens cameras with an APS-C sized sensor. It offers digital single lens reflex cameras (DSRL) image quality in a much compact and lighter package. The battery life is extended to 400 shots. A detailed description of the specifications is listed in Table 3.2.

Table 3.2: Specification of Sony Alpha NEX-3 (Source: CNET (2016b))

GENERAL	
Depth	1.3 in
Sensor Resolution	16.2 Megapixel
Optical Sensor Type	Exmor APS HD CMOS
Effective Sensor Resolution	16200000 pixels
Optical Sensor Size	15.6 x 23.5mm
Sensor Features	Anti-Dust coating, Dust Reduction (image sensor vibration)
Digital Zoom	10 x
Auto Focus Points Qty	25
Image Recording Format	JPEG, RAW, RAW + JPEG
Max Video Resolution	1280 x 720
Interfaces Provided	HDMI, USB 2.0
Flash Type	detachable flash
EXPOSURE & WHITE BALANCE	
Light Sensitivity	ISO 200-12800, ISO auto (200-1600)
Exposure Metering	center-weighted, multi-segment, spot
Exposure Modes	aperture-priority, automatic, bulb, manual, program, shutter-priority
White Balance	automatic, custom, presets
Max Shutter Speed	1/4000 sec
Min Shutter Speed	30 sec
Exposure Compensation	+/-2 EV range, in 1/3 EV steps
Auto Exposure Bracketing	3 steps in 1/3 or 2/3 EV steps
X-sync Speed	1/160 sec
Exposure Range	EV 0-20 (ISO 100)

LENS SYSTEM	
Lens type	Wide-angle lens - 16 mm
Lens Aperture	f/2.8
Focus Adjustment	automatic, manual
Max View Angle	83 degrees
Features	aspherical lens

3.2 Camera calibration

As the base for the approximate calculations being held in Chapter 3.3, the real dimension of focal length, the sensor size, and the pixel size for both cameras were needed. Some of the parameters were directly given by the manufacturer, however, to make sure that they were reliable, the camera calibration process was conducted with the use of Agisoft PhotoScan. The process was done separately for GoPro and Sony cameras.

In order to create a dataset for camera calibration, eight photos of white, black chessboard were captured. The photos were taken from eight directions (capturing a photo every 45 degrees), covering only the area of the chessboard, without any background. The samples of the dataset from both cameras are illustrated in Figure 3.1. The next step was uploading the dataset from both cameras independently and running the camera calibration process.

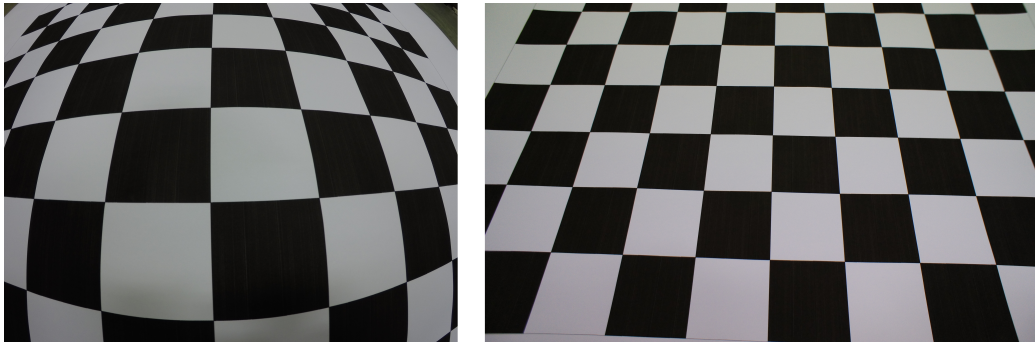


Figure 3.1: The pictures used in camera calibration for the GoPro (left image) and the Sony (right image)

The result reports for the GoPro camera are presented in Appendix A, while for the Sony camera in Appendix B. The final results, which were applied in further evaluation are shown in Table 3.3.

Table 3.3: The results of camera calibration

Parameter	GoPro Hero 4 Black	Sony Alpha NEX-C3
focal length [mm]	3	16
pixel size [mm]	0.00173066	0.00489089
image size [pix]	4000x3000	4912x3264
width of sensor [mm]	6.92	15.96
height of sensor [mm]	24.02	5.19

3.3 Evaluation of the overlap and the ground distance between camera stations

3.3.1 Theoretical approach

Before the fieldwork was performed there was a need to set up a base distance between photos to achieve adequate overlap, which would lead to reliable results. Due to space limitation, the evaluations are based on probable width of the drift. Thus, three different object distances, 5 m, 7.5 m, and 10 m were taken into consideration.

Theoretical Field of View (FOV) was calculated as the product of horizontal width and vertical view. The width and height of the sensor were transformed to the ground dimensions with use of the focal length according to the object distance. The theoretical background concerning the calculations is presented in Chapter 2.3.1.

Table 3.4: Theoretical FOV of single photo

Object distance (m)	GoPro Hero 4			SonyNEX-C3		
	Hz width (m)	V view (m)	FOV(m^2)	Hz width (m)	V view (m)	FOV(m^2)
5	11.54	8.65	99.84	7.51	4.99	37.45
7.5	17.31	12.98	224.64	11.26	7.48	84.27
10	23.08	17.31	399.36	15.02	9.98	149.81

The base distance is the distance between camera stations. In general, it is determined by photo overlap. For the approximate evaluations only, forward overlap was taken into account since the purpose of this project assumes that the images will be photographed along the drift direction just in one row. It will be identified in further studies of data acquisition. The theoretical values of the base distance concerning both cameras according to different object distances are presented in Tables 3.7, 3.6, and 3.7.

Table 3.5: The base distance for theoretical values of horizontal width when distance from the object = 5 m

		Overlap (%)			
		60	70	80	90
Camera	Hz width (m)	Base distance (m)			
GoPro	11.54	4.62	3.46	2.31	1.15
Sony	7.51	3.00	2.25	1.50	0.75

Table 3.6: The base distance for theoretical values of horizontal width when distance from the object = 7.5 m

		Overlap (%)			
		60	70	80	90
Camera	Hz width (m)	Base distance (m)			
GoPro	17.31	6.92	5.19	3.46	1.73
Sony	11.26	4.50	3.38	2.25	1.13

Table 3.7: The base distance for theoretical values of horizontal width when distance from the object = 10 m

		Overlap (%)			
		60	70	80	90
Camera	Hz width (m)	Base distance (m)			
GoPro	23.08	4.62	3.46	2.31	1.15
Sony	15.02	6.01	4.50	3.00	1.50

3.3.2 Practical approach

Due to suspicion of ultra-wide angle of the GoPro camera and the enormous extent of the Field of view visible with the naked eye, a simple field test was performed to gain the practical dimension of the horizontal width for both cameras.

The long wall of a building was applied to mark the last visible place on the photo. With help of a measuring tape the approximate distances between the marks were measured. The test was made for three various object distances separately to enable the comparison with theoretical values of the horizontal width presented in Chapter 3.3.1. The results of the field test are shown in Table 3.8. The accuracy of the results is within decimeters for the GoPro, while within centimeters for Sony.

Table 3.8: The real values of the horizontal width obtained in the field work

Object distance (m)	Practical horizontal width (m)	
	GoPro Hero 4	Sony NEX-C3
5	17.27	7.23
7.5	26.50	10.91
10	34.70	14.79

Employing the same way of calculation as in Chapter 3.3.1 applying the new, practical values of horizontal width the base distances and overlaps were evaluated. The results are given in Tables 3.9, 3.10 and 3.11.

Table 3.9: The base distance for practical values of horizontal width when distance from the object = 5 m

		Overlap (%)			
		60	70	80	90
Camera	Hz width (m)	Base distance (m)			
GoPro	17.27	6.91	5.18	3.45	1.73
Sony	7.23	2.89	2.17	1.45	0.72

Table 3.10: The base distance for practical values of horizontal width when distance from the object = 7.5 m

		Overlap (%)			
		60	70	80	90
Camera	Hz width (m)	Base distance (m)			
GoPro	26.50	10.60	7.95	5.30	2.65
Sony	10.91	4.36	3.27	2.18	1.09

Table 3.11: The base distance for practical values of horizontal width when distance from the object = 10 m

Camera	Hz width (m)	Overlap (%)			
		60	70	80	90
		Base distance (m)			
GoPro	34.70	13.88	10.41	6.94	3.47
Sony	14.79	5.92	4.44	2.96	1.48

3.3.3 Conclusions

The tables presented in Chapters 3.3.1 and 3.3.2 bring to a conclusion that the Sony camera covers around 65% of theoretical horizontal width represented by the GoPro camera, whereas the practical values show the coverage of around 42%.

The investigation exposes the fact that the theoretical value of horizontal width is extremely comparable to the real value for the Sony camera. The tiny difference could be caused by measuring errors in the field work. However, the values of the horizontal width for the GoPro camera are almost twice as large as the values obtained from the theoretical calculations. The main reason is probably the ultra-wide angle of view given by the fisheye lens. The comparison of the practical and theoretical values of the horizontal width for both cameras within different object distances is presented in Figure 3.2.

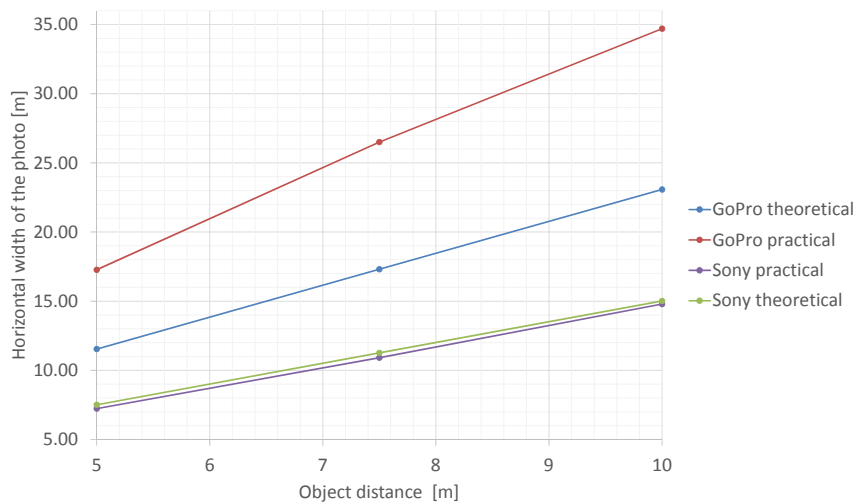


Figure 3.2: The comparison of practical horizontal width obtained in the field work with theoretical values for both cameras

Even though the software providers require a minimum 60-80% overlap between photos, the first test (described in Chapter 4) is going to be run with the higher overlap percentage. The ground base distance is decided on 1 m to be used with both cameras. This value seems to be reasonable for the 5 m long object distance which is imposed by the tunnel's dimensions. Once, with a 1 meter long base distance the horizontal width implies the overlap of 90% (for theoretical value) and 94% (for practical value) using the GoPro camera. Meanwhile, the photos captured with the Sony camera represent an 86% overlap. All the presented values are assumed as sufficient in order to accomplish building the mesh models task. The test in the NTNU tunnel is going to verify the overlap assumptions.

3.4 Camera settings test

The major role in terms of resulting 3D mesh models is the quality of photos and their spatial configuration. In addition, the images should be taken with maximum possible resolution. There is a need to avoid unwanted noise on the image as well. To find the way of capturing high quality photos with use of available cameras, the settings test was conducted, particularly to learn the possibilities with the GoPro camera, which stands out from other DSLR cameras in regards to ordinary settings. The tests were performed on the same photo station (despite of of the second step of the GoPro test, which was conducted later resulting in a different scene) applying tripod to ensure stability as well as consistency conditions. The camera was placed on a non-perpendicular direction to the wall in order to get different object distances. The same scene was photographed on every photo and the same light conditions were provided. On the wall, six black-red targets were lodged to provide visible, explicit edges to compare the sharpness between the test images.

3.4.1 GoPro Hero 4 Black

Due to large amount of options, the test of the GoPro camera was performed in two steps. In the test, the photos are taken with 12MP Wide (default). The first step consists of electing an ISO Value and a Type of Mode which brings sharp photos. In the test, nine photos were taken with various settings presented in Table 3.12.

Table 3.12: ISO value and Mode settings of GoPro camera

Photo	Type of Mode	ISO value
1	Single default settings Shutter speed: AUTO	100
2		400
3		800
4	Night default settings Shutter speed: AUTO	100
5		400
6		800
7	Night default settings Shutter speed: 2sec	100
8		400
9		800

The tested *Single Mode* and *Night Mode* with *AUTO shutter speed* bring similar results. Nevertheless, it seems to be more relevant to employ *Night Mode* for the scenes captured in the poor light conditions as the tunnels or drifts represent. The *Night mode* with *2 seconds shutter speed* (which is the slowest available option despite the *AUTO* settings) resulted in extremely bright, overexposed photos.

It is observed in every mode, that as the ISO value rises, the image sharpness becomes worse. The edges are represented by higher number of pixels spread on a larger area, which impedes their recognition. In Figure 3.3, the comparison of various ISO values taken with *Night Mode* with *AUTO shutter speed* is exposed.

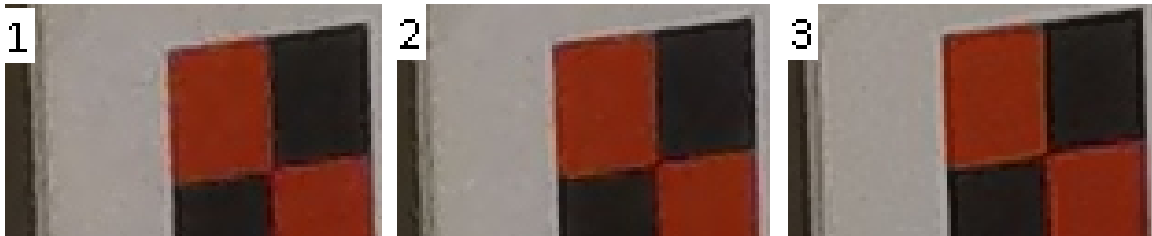


Figure 3.3: The differences in the image between ISO values: 1) ISO 800 2) ISO 400 3) ISO 100

As a result of the first step the *Night Mode* with *AUTO shutter speed* and ISO value equal to 100 were chosen.

The second step of the test was based on the results from the first step meaning that all the photos were captured by *Night Mode* with *AUTO shutter speed* and ISO 100. The *Night Mode* allows to pick up ProTune settings such as *Color*, *Sharpness*, *White Balance* and *EV Compensation*. However, only the first three options were tested. The diverse variants of the available options which were verified are presented in Table 3.13. The images were captured with default options, while only the tested variable changed. The photographed images representing photo sets for one ProTune

Setting were compared with each other in order to elect the photo which represents the best quality of the real colors.

Table 3.13: Test of the GoPro ProTune Settings

Photo	ProTune Settings	Available option
1	Color	GOPRO
2		FLAT
3	Sharpness	HIGH
4		MEDIUM
5		LOW
6	White Balance	3000K
7		5500K
8		6500K
9		NATIVE



Figure 3.4: *White Balance* options: 1) 3000K 2) 5500K 3) 6500K 4) NATIVE



Figure 3.5: *Color* options: 1) GOPRO 2) FLAT



Figure 3.6: *Sharpness* options: 1) LOW 2) MEDIUM 3) HIGH

The photos captured in the test are presented in Figures 3.5, 3.5, and 3.4. The *Color* is way brighter and not natural for the *FLAT* setting to compare with default *GO-PRO*. The resulting images taken with available options of the *Sharpness* are quite alike and it is hard to see the difference between them with the naked eye. However, there is very little inequality between *HIGH* and *LOW*, meaning the *MEDIUM* option could be the most relevant. The *White Balance* settings bring the most diverse resulting images and it is crucial to not use the *AUTO* option as it could contribute to the color variation between the overlapping photos. The observation leads to the conclusion that the real scene in terms of color similarity is represented by the photo using *White Balance* equal to 3000K.

As a result of the GoPro camera settings test *Night Mode* with *AUTO* shutter speed, ISO 100, *Color: GOPRO, Sharpness: MEDIUM* and *White Balance: 3000K* were chosen.

3.4.2 Sony Alpha NEX-N3

The Sony represents a DSLR camera type which is well-equipped with manually changing options and much more advanced than the GoPro camera in terms of professional photography. As a result, it was way easier to predict its behavior. As the light conditions in the drift or tunnel are the biggest challenge, it is crucial to catch as much light for the scene as possible and get a sharp image at the same time. To simplify this, setting the camera at a half-automatic shoot mode called *Aperture priority* was employed. This allows for a specific aperture value to be adopted, while the shutter speed is automatically adjusted, ensuring a proper exposure. The aperture value enables the user to control the depth of field, or change the range of focus and amount of background blur. A larger aperture value brings all the foreground and background into focus, while a smaller value blurs the background and isolates it from the foreground where the object is sharp.

In the test, nine photos were captured, whereas five of them were used to elect a suitable ISO value and four of them were used to pick up the relevant aperture value. The settings taken under consideration are shown in Table 3.14.

Table 3.14: Sony settings test

Photo	F-number Aperture	ISO value
1	F8	200
2		800
3		3200
4		6400
5		12600
6	F8	800
7	F11	800
8	F18	800
9	F22	800

The picture with ISO 12600 became yellowish and heavy noise appeared which affect the visibility of the targets' edges, and could cause matching problems in the software. On the other hand, the image with ISO 200 is extremely sharp and clear. The observations show the same results as in the GoPro's test meaning that ISO value should be as low as possible to enable capturing the sharpest photo.

The tested aperture values started with F8 since the lower values would blur the background scene on the tunnel's wall. As the resulting images portray the value, F22 seems to be too high for such a short object distance. In addition, with large values the photos become darker which is probably caused by not enough light available during the shoot. The aim was to elect the value which would be high enough to reach the focus exactly on the wall. Even though the photos represented by values F8 and F11 are alike and both of them give sufficient focus on the wall, it is better to take lower value which enable to grasp more light from a scene. The captured pictures show the most optimal aperture value is F8.

Due to the tests, the test shows the *Aperture priority Mode* with an aperture value equal to F8 and an ISO value equal to 200 were chosen.

Chapter 4

Test in NTNU tunnel

The test was used as an attempt before the final test in the mine was to be conducted. The NTNU tunnel was selected as an appropriate place, where the first steps to establish the method permitting to build 3D models in the poor light condition were to be taken. The main reason to launch investigation in the tunnel was dictated by its availability. In addition, data collected during the test allowed testing available options of the two software providers. This investigation was done to develop more experience in a mine, to evolve a method, and discover problems and limitations that could occur in the actual mine.

4.1 Description

The NTNU tunnel is located in Trondheim at Norges teknisk-naturvitenskapelige universitet campus Gløshaugen. The dimensions of the NTNU tunnel are represented by 5.80 m width, 4.02 m height, and around 80 m length. The only light source are the lamps mounted on the ceiling.

Due to the fact that the NTNU tunnel was already built, there was a need to create an artificial front face (wall) which could cover the visible scene of the whole tunnel. The imitation of the front face was built to simulate the rock surface, which is going to change position after every blast in the real mine. To fulfill that requirement, two blackboards mounted on wheels were used (See Figure 4.1). According to the information (one blast prolongs drift by 5 m) delivered by the mine during the data acquisition, the blackboards were moved 5 meters per one blast along the tunnel direction and simulated the progress of rock exploitation works. More detailed information is going to be presented in Chapter 4.2.



Figure 4.1: Imitation of the front face in the NTNU tunnel

4.2 Data capture

Data acquisition is the most essential part of the procedure to generate 3D models. If the set of pictures is taken in an improper way, the results could be affected or even make it impossible to reconstruct a 3D model. A proposal of the pattern concerning data acquisition is going to be presented and in the NTNU tunnel will validate the approach. It will also help disclose some imperfections, if any occur. In addition, data acquisition could also implement some improvements to the next test in the mine, if needed.

4.2.1 Location and measurement of targets

28 targets were installed on the walls along the tunnel. They were split into seven profiles, and the profiles were located approximately every 10 m in the tunnel. One profile is described as four targets lying approximately on the same plane, which is placed across the direction of the tunnel. Figure 4.2 shows how the targets were placed in the tunnel.

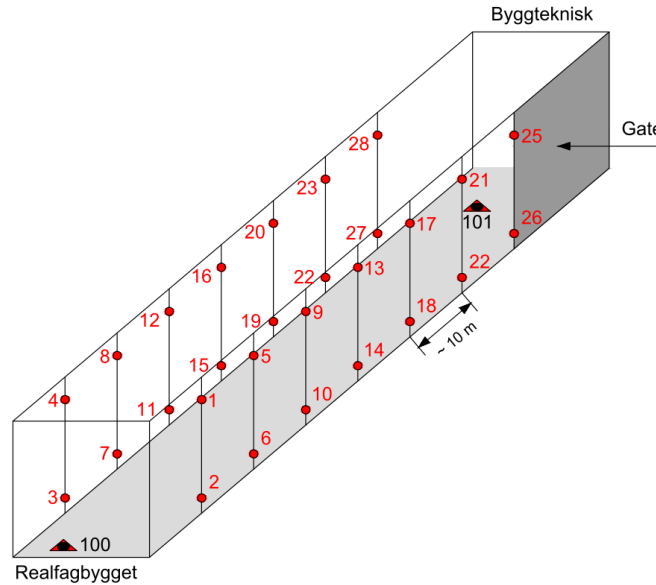


Figure 4.2: Sketch of the targets' location in the NTNU tunnel

To ensure the stability of the targets and simplify the measurement in narrow corridor, the targets were mounted on the bolt placed in wooden slats, which were attached to the walls. The bolts are produced with universal joints to allow mounting plastic target support. The targets number 10, 14, and 18 were installed on the bolt screwed on the steel, triangle support feet. In addition, there were two absolute points (100 and 101) marked on the ground (their role is going to be described below).

The next step was to conduct the measurement of targets with use of reflectorless, highly precise Leica TCRP 1201+R1000 total station and Leica 360 prism. Every target was supposed to be measured separately from station 100 and 101 meaning that all the targets were measured twice to get a control measurement and remove possible errors. However, it was impossible to get the control measurement of point numbers 5, 6, and 13 (since they were measured only from one station). The surveying between absolute points was conducted with the use of the Leica 360 prism mounted on a tripod, while the target measurement was performed by reflectorless option provided by the total station.

Afterwards, the evaluation part was executed. To establish a local coordinate system two absolute points (100 and 101) were set up. The X-axis of the system is parallel to the line linking these two points. The direction of the X-axis is determined as the direction of vector $= [100,101]$. The two absolute points were treated as known and the coordinates for them were assigned in advance. The point 100 is represented by coordinates: $X = 100\text{m}$, $Y = 100\text{m}$, and $Z = 100\text{m}$. The coordinates of point 101 were evaluated from the distance 100-101, as a result $X = 168.856\text{m}$, $Y = 100\text{m}$. The Z coordinate was calculated during network adjustment.

To obtain the coordinates of all targets, a 3D network adjustment was run with use of GISLINE v.5.3. The network adjustment report is presented in Appendix C. As a result of the measurements and evaluations, the coordinates of the targets and standard deviations were obtained. The prior errors were set up as 1.2 mgon (angular measurement error), 5 mm + 5 ppm (distance measurement error), and 2 mm (height measurement error). The assumed standard deviation of 3D adjustment was equal to 1, while the estimated standard deviation of 3D adjustment was equal to 2.1567. The value of estimated standard deviation should have been quite comparable to the assumed value. In this case the difference was noticeable. However, as it does not influence the coordinates directly, the weight base on the prior measurement errors were not optimally selected. The prior errors should have been probably taken from the specification of the instrument. The values given in the specification table says 0.3 mgon angular measurement error, and 2 mm + 2ppm distance measurement error.

All in all, it brings to a conclusion that the targets' accuracy varies within 1 cm, which is relatively high in terms of the purpose of the research. Targets 21-28 were served as Ground Control Points (GCP) and their main purpose was to provide georeference to the project (setting up the scale, the orientation, and the position of the model to enable extracting the real dimensions of tunnels). While targets 1-20 were assigned as Check Points, they were not taken into account during the georeference process. They only enabled the comparison of the 3D model coordinates and the coordinates from surveying to verify accuracy of mapping with 3D model.

4.2.2 Image capture

The pattern which will be presented below was performed in the same way with both cameras (GoPro and Sony). As a result, separate sets of photos for the cameras were acquired to compare their possibilities in terms of building 3D models. The photos were taken using the settings found during the tests showed in Chapter 3.4.

Every image was captured approximately 1.2 m above the ground. To ensure stability and lower the chances of moving the camera during exposure resulting in blurry photos, the camera was mounted on the tripod. In addition, while capturing the photos, the self-timer was turned on in the Sony camera, while the GoPro camera was controlled remotely by a mobile phone.

The locations of photo stations are determined by the dimension of the tunnel and the evaluations done in Chapter 3.3, meaning that the object distance was approximately 5 m, and the base distance was equal to 1 m.

To capture the west side of the tunnel, a line parallel to the tunnel's wall was es-

tablished by placing measuring tape around 1.2 m from the west wall. Small dots were marked in every meter along that line signaling the locations of photo stations. Correspondingly, the technique was proceeded for the east side of the tunnel, while the measuring tape was placed 0.7 m from the east wall. This approach was adopted to keep the same object distance and constant overlap between the photos.

Due to the simulation of exploitation work progress, separate sets of photos were successively captured right before each blast. Thus, the number of sets of images is equal to the number of blast performed in the tunnel. By one blasts the tunnel was prolonged by 5 m, meaning that each photo set brings 5 m long part of the new wall which needed to be mapped. Before capturing the new set of photos the blackboards were moved 5 m further along the tunnel direction.

One set of pictures taken right before the blast consisted of 21 photos (eight photos of the west side, eight photos of the east side, and five photos of the front face). These five images presenting the front phase are also captured from the line parallel to the front face, which was placed five meter apart from it. While, the photo stations were located approximately on every one meter of the line. The sketch of the photo station location creating one photo set is presented in Figure 4.3. However, the first set of photos were only georeferenced by eight GCP (21-28 points). That set of images was composed of 45 photos (20 photos of the west side, 20 photos of the east side, and five photos of the front face).

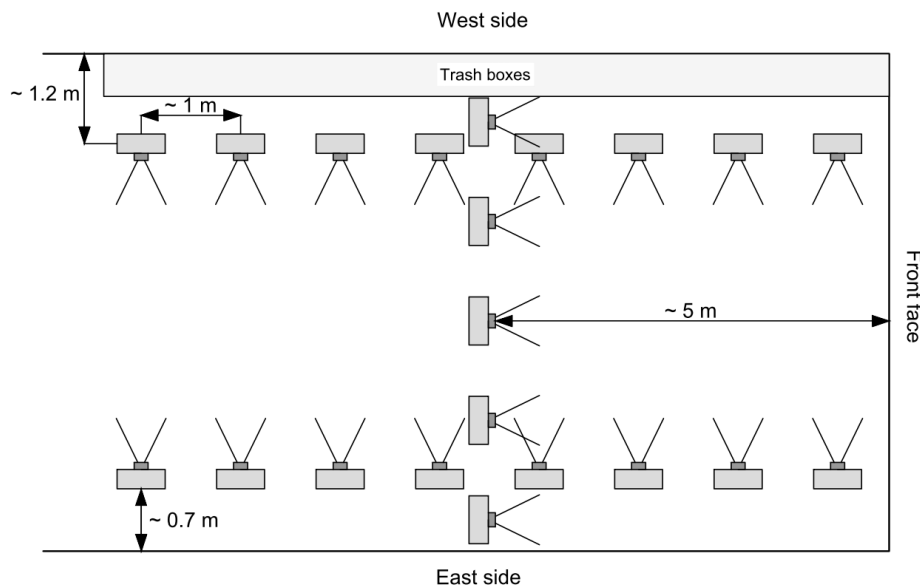


Figure 4.3: The locations of the photo stations represented by one photo set

The separate sets of photos created before each blast needed to overlap (the new images had to represent part of the scene from the previous photo set) in order to enable prolonging the model and map the exploitation progress. To reach that

requirement, six images of the new photo set (three from the east side and three from the west side) were photographed from exactly the same photo stations of the previous photo set. The locations of the photo stations are illustrated in Figure 4.4.

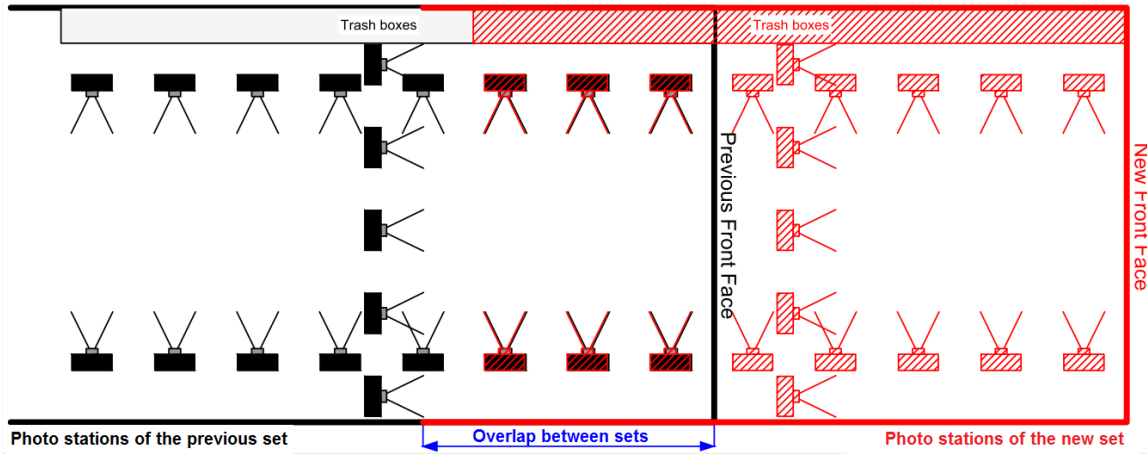


Figure 4.4: The locations of the photo stations represented by two overlapping sets of images

As a result of acquiring photos in the tunnel, a separate set of 104 photos was taken with the GoPro camera, and a set of 105 photos was acquired with the Sony. The numbers of captured images with different cameras are shown in Table 4.1.

Table 4.1: The numbers of images included in the separate photo sets

Set of photos	Number of photos	
	Sony	GoPro
1st	45	44
2nd	21	21
3rd	21	21
4th	21	21
5th	21	21
6th	21	21
7th	21	21
TOTAL	171	170

Both pictures captured with the GoPro and the Sony consisted of seven photo sets representing exploitation progress prepared as an input data to obtain 3D models in two types of software. The 1st photo set taken with the Sony covered the area of eight GCP (21-28) with 45 photos, while the 1st photo set captured with the GoPro was covering the same part of the tunnel and was represented only by 44 photos since one image presenting the middle of the front face was not stored. However, the missing photos did not affect the data processing thanks to the high overlap between

the images taken by the GoPro. Every next set of photos (from 2nd to the 7th) for both cameras contained 21 images.

4.3 Data processing

All the captured data were processed simultaneously in two types of modern software. These types of software were able to perform photogrammetric processing of digital images, and allow for the production of high resolution 3D models of existing, real-world conditions.

The first application was called Context Capture (version x64 04.01.00.514). The application was provided by Bentley Systems which is a software development company that supports the professional needs of different branches of industry and infrastructure including roadways, bridges, airports, skyscrapers, industrial power plants, as well as utility networks. The second software was called Agisoft PhotoScan Professional (version x64 1.2.4.2399), and was provided by the Russian company Agisoft LLC. The company is among the pioneers of digital photogrammetry solution developers, and their package was implemented for various industrial, and socially meaningful cases. Both applications were updated to the latest versions available during the research period.

4.3.1 Agisoft PhotoScan software

In this subsection, the workflow completed with the use of the Agisoft PhotoScan Professional (version x64 1.2.4.2399) will be presented. The main steps in the software and procedure of adding new photo sets presenting the exploitation work progress were conducted separately for GoPro photo sets, and Sony photo sets, however, they were performed in the same way. Thus, the general work flow that was conducted with one photo set will be described. The manual provided by AgisoftLLC (2016) was supportive in that case.

The first set of photos was loaded into a *Chunk* in the application. In the *Camera Calibration* dialog box (command from *Tools* menu), the *Camera type* was chosen as *Frame* for Sony and *Fisheye* for GoPro, otherwise the distortion caused by the fisheye lens would have not been considered. The next step was performed with the *Add marker* option. The coordinates of the Ground Control Points were imported to the software from a text file and markers were placed on the Ground Control Points 21-28. Each of GCP was manually marked on five photos where the middle point was distinctly visible. In addition, when the targets were illustrated on the sides of the images, they were not used due to its visibility from different angles, which prohibits pointing exactly in the middle.

The camera positions and their orientation were evaluated by using *Align photos*. Images were aligned with *Accuracy: High* and *Pair preselection: Disabled*. If the *Pair preselection: Generic* would have been used, it could have taken less time resulting in lower accuracy of matching photos. As a result, a sparse point cloud was produced and displayed. Then, in the *Reference* pane, the tool *Optimize Cameras* was applied to recalculate the camera calibration parameters.

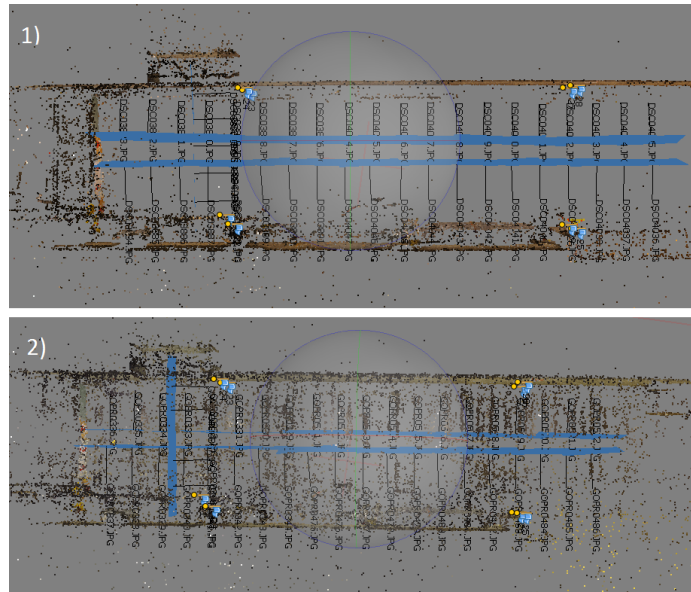


Figure 4.5: The sparse point clouds and the cameras' positions for GoPro (1) and Sony (2) photo sets generated by Agisoft PhotoScan

Afterwards, the *Chunk* was cloned containing all the photos and steps described above. Firstly, the photos overlapping with first photo set and presenting the front face were removed from the cloned *Chunk*. Thus, the five photos taken perpendicularly to the old front face and three images photographed with the GoPro on each side were excluded (See Figure 4.4). While for the sets of photos captured with the Sony camera there were only two photos excluded on the sides, as it was enough to omit the visible front face. Secondly, the images from the second set of photos representing the new front face were added instead. Thirdly, the options *Align photos* as well as *Optimize Cameras* were used again to adjust new camera positions and their parameters, but also to merge a new set of photos with the old one. This procedure was repeated until the last photo set was reached. As a result, the cloned chunks were representing the progress of exploitation works and became ready to build the models.

Separately, for each cloned chunk, the Dense Point Cloud was produced by using a workflow option called *Build Dense Cloud* with *Accuracy: High* and *Depth filtering: Aggressive*. When the task was completed, mesh models were built on the base of the Dense Point Clouds with the setting as *Source Data: Dense Cloud*, *Surface type:*

Arbitrary, Face count: Medium, and Interpolation: Enabled.

4.3.2 Context Capture software

Simultaneously, the sets of photos were run with the second type of software Context Capture (version x64 04.01.00.514). Again, the main steps in the software were universal for both photo sets acquired with GoPro and Sony and they are going to be presented below. The manual provided by BentleySystems (2016) was helpful to deal with the process.

The first set of photos was loaded to the program which has appeared as a *Photogroup* in the *Block*. In the settings of the photogroup, *Camera model type* was chosen as *Fisheye* for GoPro and *Perspective* for Sony. The next step was to run the editor from the *Control Points* pane and *Spatial Reference System* was set as default *Cartesian* due to the local coordinate system established for the task. Afterwards, a text file with the coordinates of the Ground Control Points was loaded into the editor. Each of the eight Ground Control Points (21-28) visible on the photo set was marked separately on five pictures. When the marking process was finished, the pictures were already prepared for *Aerotriangulation* process where all of the options in the *Aerotriangulation definition* window were kept as default. The bundle adjustment was performed in the *Aerotriangulation* process by choosing the option *Use control points for adjustment*. As a result, the new *Block-AT* was built and in the *Control Points editor* the statistics concerning the accuracy of the adjustment were presented.

Afterwards, the *Block-AT* was cloned. Firstly, the images overlapping with first set of photos and presenting the front face were removed from the *Photogroup* cloned *Block-AT*. The same pattern of excluding pictures within one photo set was applied as it was explained in Chapter 4.3.1 (five photos taken perpendicular to the old front face, six photos photographed with the GoPro, four captured with Sony). Secondly, the images from the second photo set representing the new front face were added as new *Photogroup*. It was essential to change the *Camera model type* in every created *Photogroup* according to the data captured with different cameras. This procedure was repeated until the last photo set was reached.

The last step was to build 3D mesh models for every new block which was prolonging the tunnel. For that reason, *New Reconstruction* was established and in the pane *Processing settings* all the options were set as default. By applying option *Submit a new production* where the *3D mesh model* was chosen, the software provided a textured, georeferenced 3D mesh model of the tunnel.

4.4 Results

The photos captured with Sony and GoPro were processed in both application Context Capture and Agisoft PhotoScan. In this chapter, the results such as models and residuals on Check Points provided by software are going to be presented. The most interesting part concerns the largest area of the tunnel mapped with the 3D model. Thus, the maximum number of photo sets which was possible to reconstruct is portrayed. To insert the same input data into the reconstruction procedure (bundle adjustment), the same photos were used for georeferencing in both programs. The figures shown in this chapter present screen shots from the applications. Important note referring the results portrayed in programs, namely the position of residuals for X and Y coordinate, are switched. Thus, the residuals of X coordinate which are shown in figures within this chapter refer to the residuals of the Y coordinate and vice versa.

4.4.1 GoPro camera

Photos acquired with the GoPro camera enabled combining six photo sets together in both programs. The models generated by Context Capture and Agisoft PhotoScan were based on the same pictures, thus it is expected to obtain similar results. The Check Points (13-20) are located in the area mapped with the 3D models (See Figure 4.2).

4.4.1.1 Context Capture

Context Capture struggled with adding the seventh photo set captured with GoPro by giving a warning that a number of photos cannot be used for reconstruction. However, on the base of six sets of photos consisting of 104 images, it was possible to obtain a well-reconstructed model (See Figure 4.6). For eight Ground Control Points (21-28), the RMS of 3D error (average distance in meters between estimated 3D position of the GCP in the model and surveyed values of GCP coordinates) was equal to 0.003m (horizontal error 0.002m, vertical error 0.003m).



Figure 4.6: 3D mesh model produced from photos captured with GoPro provided by Context Capture

By pointing on five photos presenting each Check Point, it was possible to extract the model's coordinates of these points. The software provided the residuals on the Check Points (13-20) which were calculated as the difference between the model's coordinates and the surveyed coordinates. The residuals are shown as a 3D horizontal error and a 3D vertical error in Figure 4.7.

Name	Category	Check point	Given X	Given Y	Given Z	Horizontal accuracy [u]	Vertical accuracy [u]	Estimated X	Estimated Y	Estimated Z	RMS of reproj. error [px]	RMS of dist. to rays [u]	3D error [u]	3D horizontal error [u]	3D vertical error [u]
13	Full	<input checked="" type="checkbox"/>	103.927	129.579	101.538	0.010	0.010	103.926	129.557	101.519	11.05	0.027	0.029	0.022	-0.019
14	Full	<input checked="" type="checkbox"/>	103.527	129.666	99.269	0.010	0.010	103.525	129.655	99.253	8.72	0.019	0.019	0.011	-0.016
15	Full	<input checked="" type="checkbox"/>	99.403	129.444	99.154	0.010	0.010	99.412	129.440	99.138	7.48	0.018	0.019	0.010	-0.016
16	Full	<input checked="" type="checkbox"/>	99.405	129.430	101.177	0.010	0.010	99.418	129.420	101.161	6.40	0.016	0.023	0.016	-0.016
17	Full	<input checked="" type="checkbox"/>	103.889	141.362	101.587	0.010	0.010	103.889	141.356	101.580	3.74	0.009	0.009	0.006	-0.007
18	Full	<input checked="" type="checkbox"/>	103.479	141.327	99.286	0.010	0.010	103.612	141.387	99.243	31.35	0.066	0.152	0.146	-0.043
19	Full	<input checked="" type="checkbox"/>	99.393	141.382	99.173	0.010	0.010	99.400	141.380	99.168	2.77	0.007	0.009	0.007	-0.005
20	Full	<input checked="" type="checkbox"/>	99.397	141.377	101.195	0.010	0.010	99.409	141.371	101.191	2.40	0.006	0.014	0.013	-0.004

Figure 4.7: Residuals on the Check Points from photos captured with GoPro provided by Context Capture

The highest horizontal residual is portrayed on Check Point number 18 which is probably due to the fact that the target was mounted on the bolt screwed onto a triangular support feet, and the object was too thin to be reconstructed. The rest of the residuals do not exceed 2.2 cm in the horizontal plane and -1.9 cm in the vertical plane. They are rather close to the accuracy provided with the total station measurement. There is a tendency that the residuals gets larger when the distance from the Ground Control Points increases.

4.4.1.2 Agisoft PhotoScan

As with production conducted in Context Capture, images acquired with the GoPro camera enabled prolonging the model with six photo sets also in Agisoft PhotoScan. When the seventh set of photos was added, the sparse point cloud did not resemble the tunnel any longer, as the pictures were disordered. Thus, the model consisted of 105 photos captured with GoPro (See Figure 4.8). For eight Ground Control Points (21-28), the RMS of 3D error (average distance in meters between estimated 3D position of the GCP in the model and surveyed values of GCP coordinates) was equal to 0.0048m (X error 0.0033m, Y error 0.0026m, Z error 0.0022m). The accuracy of georeferencing is close to the values gained for the same GoPro images georeferenced in Context Capture presented in Chapter 4.4.1.1.



Figure 4.8: 3D mesh model produced from photos captured with GoPro provided by Agisoft PhotoScan

To comment on the accuracy of mapping with use of the 3D model, the Check Points (13-21) were applied. The coordinates from surveying were treated as reference values during the comparison with coordinates delivered by the model. Again, by pointing on five photos presenting each Check Point Agisoft PhotoScan, delivered the residuals on Check Points and called them as X Error, Y Error, and Z Error (See Figure 4.9).

Markers	X err (m)	Y err (m)	Z err (m)
<input type="checkbox"/> 13	0.019226	-0.039234	0.032659
<input type="checkbox"/> 14	0.009981	-0.036004	0.032101
<input type="checkbox"/> 15	0.009308	-0.035237	0.034472
<input type="checkbox"/> 16	0.014933	-0.034103	0.038316
<input type="checkbox"/> 17	0.003086	-0.008978	0.008254
<input type="checkbox"/> 18	0.174971	0.029497	-0.038017
<input type="checkbox"/> 19	0.003195	-0.010712	0.011110
<input type="checkbox"/> 20	0.004304	-0.010134	0.015062

Figure 4.9: Residuals on the Check Points from photos captured with GoPro provided by Agisoft PhotoScan

As before, the largest residuals are portrayed on Check Point number 18 due to the thin object where the target was mounted. Thus, the values for Check Point number 18 are not reliable and are treated as gross error. The residuals on Check Points (17,19, and 20), which are situated closer to the Ground Control Points, represent smaller values than the residuals obtained for the rest. In general, the values of residuals do not exceed -4 cm in the horizontal plane and 3.8 cm in vertical plane. To compare these with the results gained in Context Capture, the values are slightly higher, especially on Check Points 13-16 located at the end of the tunnel.

4.4.1.3 Sony camera

The photos captured with the Sony camera brought more problems concerning reconstruction of and generating 3D models. Some of the results which were possible to obtain with the programs are going to be presented. Once more, the same images were applied in both programs to georeference models by marking on them the Ground Control Points in order to provide equivalent input data.

4.4.1.4 Context Capture

Unfortunately, in Context Capture it was impossible to generate 3D models even for the first set of photos. There was an information box appearing on the screen saying that part of the photos could not be used for reconstruction purposes (See Figure 4.10). Presumably, the main reason for that was the improper way of capturing images. There should have been additional photos taken from different angles covering the corners between the front face and tunnel's walls.

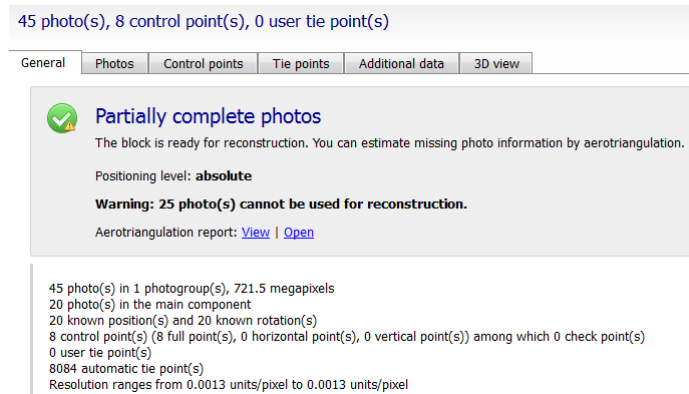


Figure 4.10: Warning information about reconstruction process failure appearing in Context Capture

In general, it was decided to do not intervene with manual tie points since the aim was to generate the most optimal process of acquiring photos, in order to simply the steps of data processing in the programs. At least, this example allowed to draw conclusions that the data acquisition pattern should be improved. However, just to show the overview of how the model produced in Context Capture would look, there were eight manual tie points added into the reconstruction process. This intervention enabled the model to be produced from 45 photos belonging to the first photo set captured with Sony (See Figure 4.11). The manual tie points were located on the two blackboards (imitation of the front face) connecting the pictures from the side rows with the row presenting only the front face.



Figure 4.11: 3D mesh model produced from photos captured with Sony provided by Context Capture

Since the reconstruction was possible with additional tie points, it indicates that the

overlap between photos was sufficient. Thus, it brings to conclusion that the only problem was generated by an inappropriate data acquisition pattern.

4.4.1.5 Agisoft PhotoScan

For a change, Agisoft PhotoScan enabled to prolong the tunnel with six sets of photos captured with Sony camera. Thus, the model was consisting of 105 photos (See Figure 4.12). For eight Ground Control Points 21-28, the RMS of 3D error (average distance in meters between estimated 3D position of the GCP in the model and surveyed values of GCP coordinates) was equal to 0.0122m (X error 0.0025m, Y error 0.0033m, Z error 0.0114m).

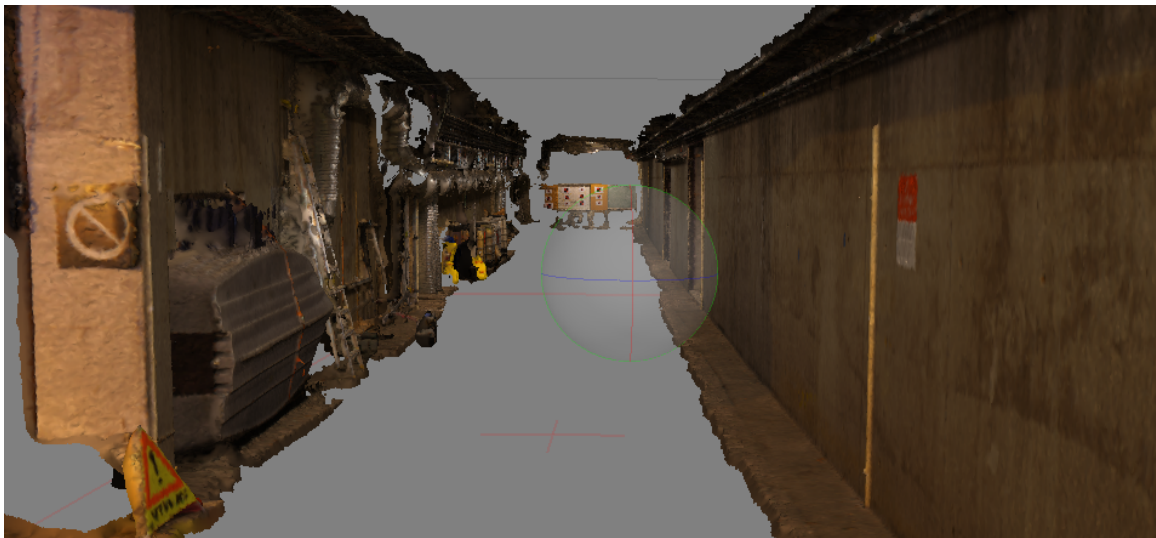


Figure 4.12: 3D mesh model generated from photos captured with Sony provided by Agisoft PhotoScan

As it was conducted previously to give comments on the accuracy of mapping provided by the 3D model, the Check Points 13-20 were employed. The coordinates from surveying were the reference values during the comparison with the model's coordinates. Each Check Point was marked on five photos and the residuals were presented in the software. The results are shown in Figure 4.13.

Markers	X err (m)	Y err (m)	Z err (m)
<input type="checkbox"/> 13	0.222124	-0.655969	0.239219
<input type="checkbox"/> 14	0.199149	-0.681523	0.126910
<input type="checkbox"/> 15	-0.264874	0.736553	0.258486
<input type="checkbox"/> 16	-0.267793	0.763834	0.148861
<input type="checkbox"/> 17	0.062142	-0.189629	0.087270
<input type="checkbox"/> 18	0.057863	-0.213475	0.021466
<input type="checkbox"/> 19	-0.093855	0.233881	0.098358
<input type="checkbox"/> 20	-0.091264	0.251349	0.034143

Figure 4.13: Residuals on the Check Points from photos captured with Sony provided by Agisoft PhotoScan

As the values show, the further from the Ground Control Points the larger residuals are obtained. The magnitude of the residuals is extremely large since, on some Check Points, they reach almost 80 cm. This model could not be used for mapping purposes at all. As it was already explained in Chapter 4.4.1.5 this is caused by improper data acquisition since again there was a problem with connecting the front face imitation with the tunnel's walls. Figure 4.14, shows the top view of the sparse point cloud, where it is visible that the wall is bending at the end of the tunnel (close to the front face imitation).

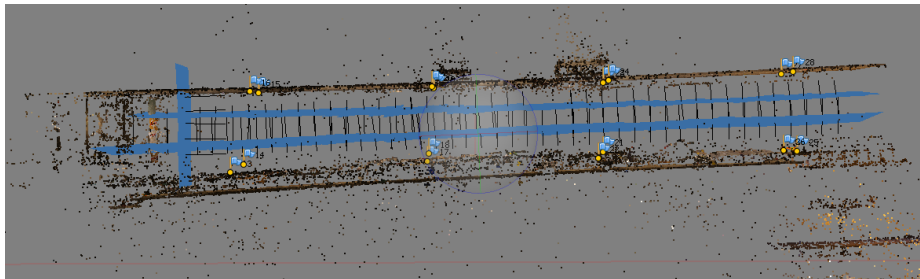


Figure 4.14: Top view of the sparse point cloud presenting bending wall

As it was already mentioned in Chapter 4.4.1.5, the intervention with manual time points could be performed in the application and the residuals on the Check Points probably would become smaller. However, it would bring additional work in data processing would defeat the purpose.

4.5 Final comments

The test conducted in the NTNU tunnel brought many valuable experiences concerning the data acquisition patterns, as well as a broadened knowledge of the software.

Data acquisition is crucial in order to obtain reliable results. The pictures taken with the Sony camera demonstrated some inadequacy in the utilized data acquisition pattern. Thus, it is essential in the next test to capture some additional pictures presenting the corners between front face and walls of the tunnel. This intervention will ensure the proper reconstruction, as well as increase the accuracy of mapping.

In terms of comparison of the programs used in the test, there are some advantages and disadvantages which have been noticed both for Context Capture and Agisoft PhotoScan. Context Capture informs the user if the images were acquired in inappropriate ways, and refuse the reconstruction - a benefit for non-experienced professionals. The Agisoft PhotoScan, on the other hand, reconstructs poorly acquired photo sets without direct information for the user. The Check Points were the only way to find out the large distortion in the model. This may be an advantage for some purposes, however, if the accuracy of the resulting model is not as demanding. In both programs, there is an option to add manual tie points which could be helpful in reconstructing poor photo sets, while in this thesis, there is a need to apply fully-automated process of generating models. Thus, it is important to find a way to take photos that will avoid additional workload for the user.

The models produced in both software from pictures captured with the GoPro provided a base to compare and comment on accuracy of mapping with 3D models. Even though the georeferencing was performed on the basis of the same photos, and its accuracy was extremely similar in both applications, some differences in residuals' magnitude appeared. In Context Capture, the residuals on the Check Points located at the end of tunnel were a little bit smaller to compare with those represented by the model generated in the Agisoft PhotoScan software. However, it cannot be stated that Agisoft is worse in that case since there is not enough data to prove this.

In terms of visual comparison of the models created in both applications unambiguously, the conclusion can be drawn that the mesh models produced in Context Capture software constructed the best reality. The models seem to be more detailed and eye-friendly. Also, the model's textures give an impression that they are brighter and more precise.

Due to some arguments presented above and the fact that the mine where the next tests will be held uses Bentley software, it was decided to process the data captured in the mine with the use of the Context Capture software.

There were two cameras applied in the test: GoPro (as a representation of consumer electronics with a fisheye lens), and Sony (a more advanced DSLR camera with better parameters and a wide angle lens). Due to various extensions in Field of View and Focal Length, the resulting overlap between the sets of photos acquired were different for each camera. It was predicted that the camera with a wider angle lens would be more adequate for the tasks conducted in narrow corridors. However, there were doubts

that the fisheye distortion would affect the outcomes. Nevertheless, the results from both applications has shown that the algorithms properly dealt with the distortion caused by the ultra-wide angle lens in the GoPro camera. As the main goal of the test in the NTNU tunnel was to establish an optimal data acquisition method to generate 3D models, the GoPro camera was applied for the real mine conditions. The GoPro camera offered a larger Field of View which allowed for a lower number of pictures to make the 3D model. The lower number of photos results in a shorter acquisition time, which is essential in mine operations. In addition, it is a huge advantage that the GoPro is waterproof and dust proof as conditions in the mine are harsh. All in all, the consumer electronic camera was added into the test in the NTNU tunnel as an experiment, however, it transpired to be the best tool available.

Chapter 5

Test in the mine

The previous chapters introduced the preparations for a practical situation in the mine where all factors need to be well-organized and be as efficient as possible. Some improvements in the data acquisition pattern were implemented to ensure problem-free production of the 3D models. As it was already decided during the research in the mine, only GoPro camera was employed to reduce time of data acquisition. The data processing was performed with Context Capture since the mine already uses Bentley products in their daily basic works. As long as the goal is to introduce this method to a mine's routines, it is more convenient to use known software environment. In this chapter general workload, changes in data acquisition adopted in the situation, as well as results obtained during the research period will be presented.

5.1 Camera settings tested in the mine

As the conditions in the the mine were different from, the test tunnel the first step of data acquisition was to establish appropriate camera settings to capture good quality pictures. During the settings test two LED lamps 10 m apart from each other were mounted on the tripods. The GoPro was placed on the tripod in the middle between the lamps.

White Balance was the first feature taken into consideration. As a quick test four photos (See Figure5.1), with various *White Balance* options, were photographed. They presented the same scene in stable light conditions. The rest of the settings in the camera were set as *Single Mode; Shutter speed: AUTO; ISO 100; Sharpness: Medium; Color: GOPRO*.

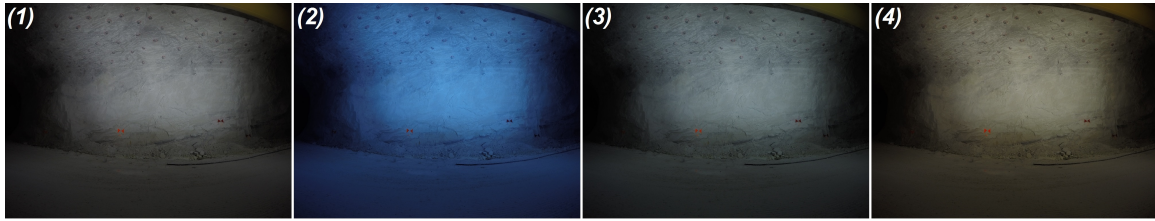


Figure 5.1: White Balance comparison (1) AUTO (2) 3000K (3) 5500K (4) 6500K

As it is visible in the figure, the value *3000K* gives unnatural, blueish color which cannot be accepted due to enormous deviation from the norm. Meanwhile, the value *6500K* presents a more yellowish scene not comparable to the reality. *AUTO* and *5500K* bring extremely similar images which could be an indicator that the camera automatically adjusted *White Balance* to the value close to *5500K*. As there is a need to possibly keep the acquired overlapping photographs with the same settings, the value *5500K* was chosen most appropriate.

The *ISO value* was the second option taken into account. There were four images (See Figure 5.2) acquired presenting the same scene. The rest of the settings in the camera were set as *Single Mode*; *Shutter speed: AUTO*; *White Balance: 5500K*; *Sharpness: Medium*; *Color: GOPRO*. The *ISO value* is supposed to brighten the photo when the value increases, however at the same time, the sharpness of the photo decreases (as seen in the results of a similar test presented in Chapter 3.4.1 shows).

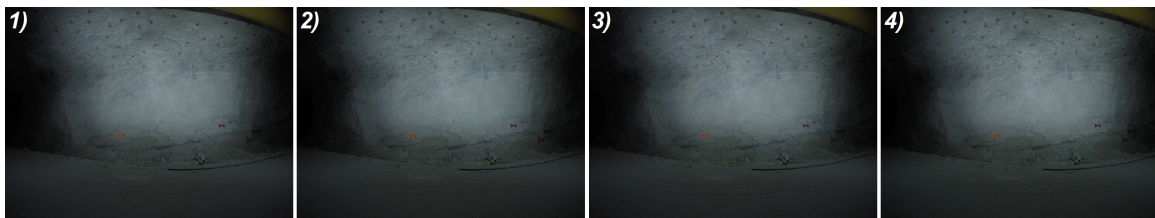


Figure 5.2: ISO value comparison (1) ISO100 (2) ISO200 (3) ISO400 (4) ISO527

The images with diverse *ISO value* do not present considerable variation since the *AUTO shutter speed* probably compensates it. The *Shutter speed* gets longer when the *ISO value* is increased. It can be observed that slightly more light appears on the edges when the value is higher, nonetheless this cannot be treated as a significant change. In addition, the *Shutter speed* is equal to 6 seconds when the *ISO100* is set. While the *ISO800* was set, the *Shutter speed* reached its maximum 30 seconds (the highest allowed in the GoPro camera), and registered the highest possible value equal to *ISO527*. As the presented photos indicate the differences are barely noticeable, it was decided to focus on sharpness of the photo and choose an *ISO100*.

During research in the mine, all photos were acquired with camera settings which are presented at the beginning of Chapter 5.2.4.

5.2 Mapping the progress of exploitation works

In this chapter, the method of prolonging the model of the tunnel by adding new sets of photos tested in the NTNU tunnel (See Chapter 4) is going to be applied. This will be presented as part of a daily routine, in a real situation, right before drilling and blasting. Due to different dimensions of the drift and safety requirements some modifications have been performed. The description of workload, results, and accuracy obtained by the method will be presented.

5.2.1 Description

Due to geological variations, the exploitation work plan could change since the excavated rocks bring new information with each blast. As a result, the direction of the drifts could suddenly change with every blast. There is a need to keep a minimum distance between other rooms which are driven in neighboring area. Every blast prolongs the drift with 5 m, while during one week, 2-3 blasts are performed. The surveyor updates the mine map every 2-3 weeks or if some special needs appear. Updating a map with photogrammetry would give a better overview where the drift is bending after each blast and decrease the probability of crossing the minimum distance to other drifts. In addition, the geological information would be documented. The approximate dimensions of drifts in the mine are presented in Figure 5.3.



Figure 5.3: Approximate dimensions of drifts in the mine

During the research period in the mine, the pictures were captured in several front faces which were imposed by the location of the drilling rig providing light source. Not all of the results will be shown in the thesis, however it brought essential experience and allowed to establish an optimal way of performing the task by reducing the time for data acquisition from 40 minutes to around 10 minutes.

There were two drifts (Drift A and Drift B) shared by the mine to apply this method.

As the tasks were performed correspondingly in both drifts, the general description of work accomplishment will be presented with reference to one of the drifts.

5.2.2 Ground Control Points

To achieve the most reliable georeference of the models, it is crucial to determine a proper spatial geometry of Ground Control Points. The minimum number of Control Points to fix the georeference is equal to three (though there is no control if any errors occur). It is recommended to use at least four Control Points to enable potential error detection. In order to obtain a stable solid, which was the reference for every next model showing the prolonging process, eight GCP were marked on the drift's walls (as it was also shown in Chapter 4.2.1). The marks were widely spread in the area of the first model resulting in four GCP on each wall. Marking was performed by mine workers using a lift. The distances between GCP were kept as long as it was possible with the light conditions provided by a drilling rig. The configuration of the Ground Control Points on the wall is shown in Figure 5.4.

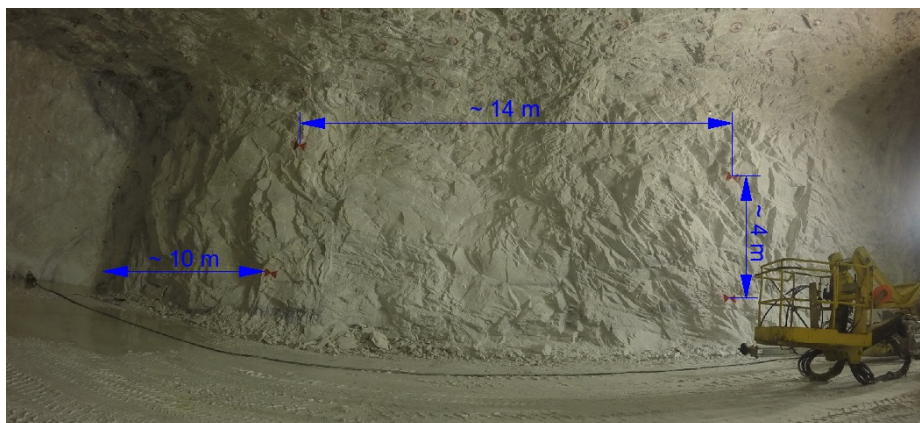


Figure 5.4: Location of Ground Control Points in the drift

The distances provided in Figure 5.4 are approximate. The opposite wall was prepared in the same way.

The next step consisted of measurements to collect coordinates of the Ground Control Points in the mine's coordinate system.

5.2.3 Surveying

All surveying measurements were held with reflectorless total station Leica TCRP 1201+R1000 and two types of Leica prisms (360 round prism and circle prism). As a connection to the mine's network, there were two known points used, already mounted with bolts in the walls by a mine surveyor, in nearby a area (See Figure 5.5).



Figure 5.5: The equipment used during the measurement on the known points

The surveying conducted in both drifts (A and B) was held with similar principle. Two short, separate traverses started from known points located on the cross, which splits into Drift A and Drift B. Each traverse was measured to determine the coordinates of new fix points based in the drifts. As a result, two fix points per drift were stable mounted with the bolts close to the area of Ground Control Points (See Figure 5.6).



Figure 5.6: The fix point with the prism mounted on the bolt

These fix points were prepared as reference points to set up a free station in order to collect coordinates of eight Ground Control Points applying reflectorless option provided by total station. Another purpose of mounting the fix points was to conduct future measurements of the Check Points. This was completed for the sake of assessing the accuracy of mapping the drift with 3D model (See Chapters 5.2.6 and 5.2.7). Additionally, ordinary measurements to update the mine map were conducted, which included lines along the walls, ceiling, and floor in the drift. This enabled Microstation V8i (SELECTseries 4) to produce a map and draw sketches. The sketches present location of the fix points and GCP in Drift A (See Figure 5.7) and Drift B (See Figure 5.8).

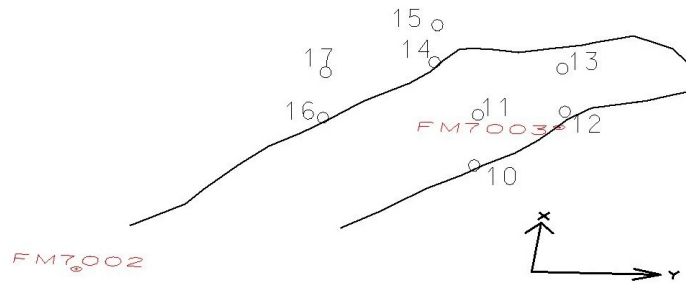


Figure 5.7: The location of fix points (FM7002 and FM7003) and Ground Control Points (10-17) in Drift A

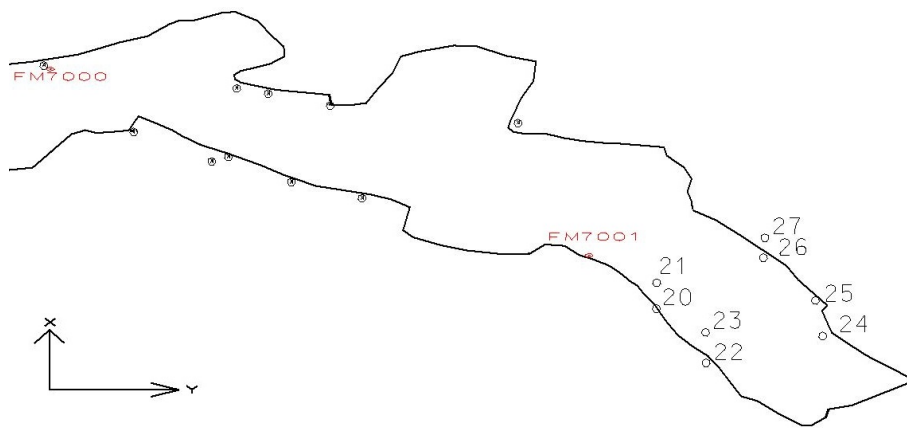


Figure 5.8: The location of fix points (FM7000 and FM7001) and Ground Control Points (20-27) in Drift B

The results from measurements were calculated in the software GEMINI Oppmåling v.5.3 and GISLINE v.5.3. As a result of the surveying part, the coordinates of two fix points each drift were determined (Drift A - FM7002 and FM7003, Drift B - FM7000 and FM7001). On their base, the coordinates of the Ground Control Points in each drift were calculated (Drift A - 10-17, Drift B - 20-27). In addition, the coordinates of fix points were treated as error free. Furthermore, the accuracy of the GCP was assessed from the instrument specification (0.3 mgon angular measurement error and 2 mm + 2 ppm distance measurement error) also taking into consideration distance to the points and geometry. Thus, the accuracy of each Ground Control Points is equal to +/- 1 cm.

The same approach concerning the coordinates' accuracy was also used for the Check Points which were marked and measured when the last blast in each drift during the research period occurred. The coordinates of the Check Points were collected in order to compare them with the model's coordinates. Their location is going to be presented in Chapters 5.2.6 and 5.2.7.

Due to company privacy, the coordinates cannot be announced.

5.2.4 Data capture

Each photograph was captured with the same camera settings such as: Aperture F2.8; Mode: SINGLE; 12MP Wide; SPOT METER: ON; PROTUNE: ON; White Balance 5500K; Color: GOPRO; ISO100; Sharpness: MEDIUM; and, EV Comp: 0.

The data acquisition process was implemented as a part of mine routine and the time for capturing pictures had to be as short as possible to withdraw delaying the production process. Sets of photos were taken for every blast in the drift during the research period. Each set of photos presenting the actual appearance of the drift was acquired when the scaling works (removing all the loosen parts of the rocks) and bolting works had finished, and right before the drilling and blasting works were performed. The one and only source of light was provided by powerful LED lamps mounted on a drilling rig (See Figure 5.9). The rig's front wheels were stopped 30-35m from the front face. Moreover, drilling booms and a basket crane were placed on the ground to avoid occluding the drift's walls.



Figure 5.9: The mobile drilling rig with LED lamps

Due to the rock mechanics issues and safety requirements, some limitations concerning the location of photo stations during data capture arose. Since the exact planning of the base distance between photo stations and the object distance resulting in approximate percentage of overlap was hard to implement in the real situation, the experience gained during the test in the NTNU tunnel became crucial. For that reason, the sets of photos were captured intuitively.

At the beginning deliberately more pictures were photographed to assure appropriate overlap. There were two approaches taken into consideration: 1) the camera pointing in a horizontal direction and 2) the camera tilted towards ceiling (seeing that the part of the floor was still visible on the picture). The findings demonstrated that the second approach prevented potential gaps in the ceiling, which occurred by applying camera pointing in a horizontal direction. Therefore, it was determined to apply the tilted camera method as an optimal technique during data acquisition.

The general pattern introduced during the process of images capturing corresponded to all sets of photos and will be described below. One set was represented by 40-60 tilted pictures which were taken in three main rows pointing perpendicularly to the front face as well as to the walls (See Figure 5.10 generated by Context Capture). In addition, 2-3 pictures of each corner were captured from slightly different angles in order to ensure correct connection between walls and the front face. The base distance between photos in a row was reaching 1 - 1.8 m. Meanwhile, the object distance (the distance to the walls) varied from 10 to 14m. The row of photos portraying the front face was placed around 5 to 8 m away. The overlap between photos was approximately 90%.

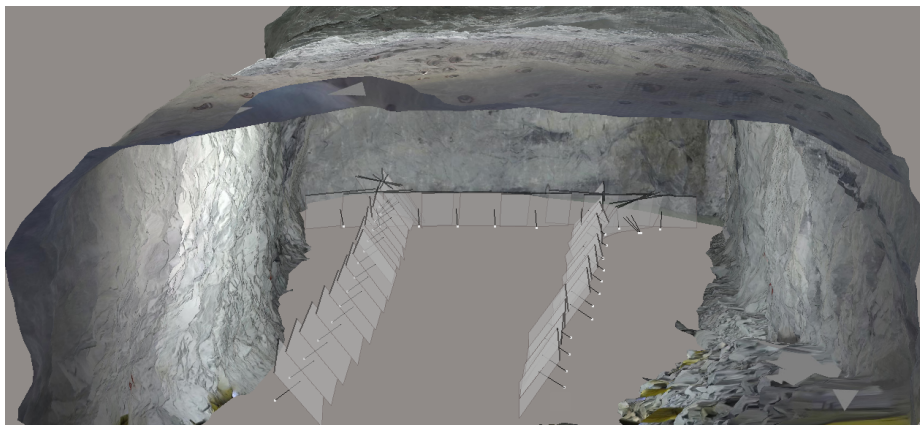


Figure 5.10: Positions of each camera explaining the images acquisition pattern

To map the progress of exploitation works, the separate sets of photos were captured before each blast. A new photo set (presenting a new front face) needs to overlap with an old photo set in order to match them together and prolong the model. It was achieved by marking a position of the rig's front wheels on the walls, while capturing each set of photos. Thanks to these signs, the reference position was determined (signaling where the previous set of photos was captured). Starting the data capture process, the new position of a rig was assigned by the previous sign, placing the front wheels approximately 5 meters away from it. When the rig was located in a desired place, the acquisition of the new set of images started and the first camera position was placed at the end of one of the drilling rig's boom (around 8 m from the front wheels) as is presented in Figure 5.11. Afterwards the general data acquisition pattern described previously in this section was employed.

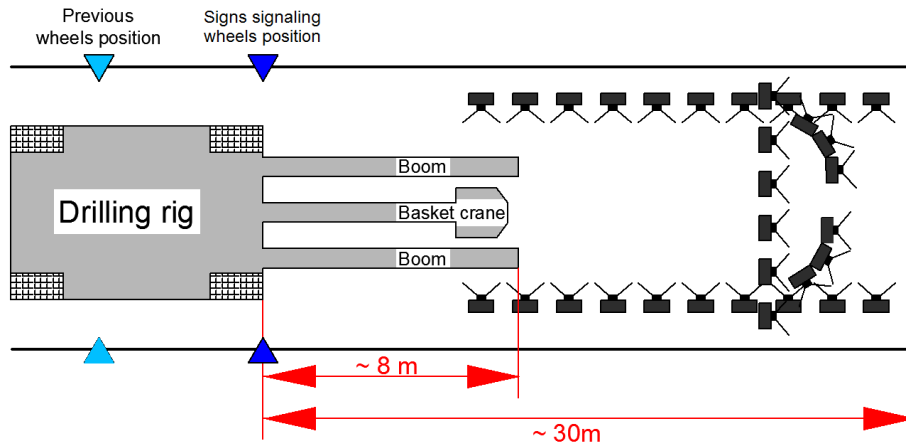


Figure 5.11: The drilling rig’s location as a reference to acquire new sets of photos

5.2.5 Data processing

All the data collected in the fieldwork was prepared to be processed with Context Capture software in order to generate georeferenced 3D mesh models of the drift. This chapter explains the procedure conducted in the program which enabled prolonging the model of the drift where the exploitation works had taken place. The main idea was to re-build a previous model by adding new information provided with each blast. Thus, the first model was covering the area where the eight GCP were located as well as the front face present at that time. The second model presented the freshly excavated part with new front face, but also the area already mapped in the first model (without the old front face). Analogically, for every new blast (set of photos), the next model was taking longer and was covering a larger area of the drift. The detailed description of the steps which had to be undertaken in the software to generate these models will be presented below.

5.2.5.1 One set of photos

The new project was created in the software and the new *Block* was established. The first set of photos was loaded to the program which has appeared as a *Photogroup*. In the settings of the photogroup, the *Camera model type* was chosen as *Fisheye*. The next step was to run the editor from the *Control Points* pane. Based on experience, it was essential to choose the right *Spatial Reference System* (both horizontal and vertical system) from the database first, and afterwards import a text file with the coordinates of the Ground Control Points into the editor. Otherwise the coordinates would have been treated as they belonged to the Cartesian Coordinate System (default) which affects the results of the *Aerotriangulation* process. Both the horizontal and the vertical accuracy of the coordinates were set as 1cm. Next, each of the eight Ground Control Points visible on the photo set was marked separately on five pictures which was a base to georeference the model. When the marking out process was fin-

ished, the pictures were already prepared for the *Aerotriangulation* process. All of the options in the *Aerotriangulation definition* window were kept as default despite the *Key point density* which was changed into *High* (it is recommended for places with poor light conditions). The bundle adjustment was performed in the *Aerotriangulation* process by choosing the option *Use control points for adjustment*. As a result, the new *Block-AT* is built and in the *Control Points editor* the statistics concerning the accuracy of the adjustment are presented. In addition, the software generated 3D view where the sparse point cloud consisted of the key points was shown as well as the positions of the camera (See Figure 5.12).

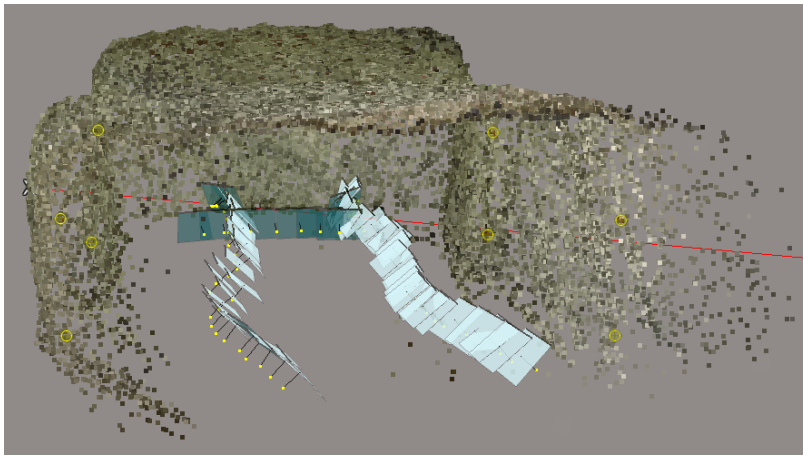


Figure 5.12: 3D view generated in Context Capture after the *Aerotriangulation* process

While the *Aerotriangulation* process was completed the *New Reconstruction* was established within the *Block-AT*. In the *Spatial Framework* pane the *Mode: Regular planar grid* was selected since it enables producing the mesh model in cubic tiles. The size of tiles have been determined and adjusted to the maximum RAM available on the computer. This option brings huge advantage when the dataset consist of high number of pictures. As a result, there is no need to use an extremely powerful computer since it is just a matter of adjusting the tile size to the available capacity before the production is submitted. In the pane *Processing settings*, all the options were set as default except from *Geometric precision* which was set as *Medium* again due to the same fact concerning poor light conditions. When all the settings were adjusted, the option *Submit a new production with the 3D mesh model* was chosen. As a result, the program produced a textured, georeferenced 3D mesh model of the drift.

5.2.5.2 Adding a new set of photos

As the exploitation works were proceeding, the new photo sets were arriving and the model was prolonged. The recipe of adding new set of photos is universal and was

applied for every next set of photos.

The *Block - AT*, created during preparation of the previous model, was cloned. In the cloned block, the pictures presenting the previous front face had been removed from the *Photogroup*. The photos on which a little part of the front face was visible (covering up to 1/5 of the photo's area) were accepted, otherwise most of the photos would have been excluded due to large the Field of View provided by the wide angle lens. The most important step was to remove the row of photos parallel to the face as well as the 4-6 photos covering the corners. As a result, 12-28 pictures remained from the old photo set. Later, the new set of photos was uploaded to the new *Photogroup* where the *Camera type model* was again set as *Fisheye*.

As the GCP were located intentionally only at the beginning of the model's area and were already saved in the cloned block, there was no need to mark any GCP on the new photos. Due to low number of blasts acquired during the research period in the mine, it was decided to test the method when only pictures from first set of photos was georeferenced and the rest of the photo sets were added only by matching. Actually, if the GCP are clearly visible close to the middle of the photo area, it is advised to mark each one also on the pictures belonging to the other set of photos. The accuracy of the georeferencing could most likely be increased if high number of the photo sets would have been added to the model. The procedure concerning the *Aerotriangulation* process of the cloned block was followed with the default options suggested by the program despite of *Key point density* which was changed into *High* as before. Consequently, the new sparse point cloud and camera positions of two, matched sets of photos was generated. To distinguish the different photo sets, the new photo set was highlighted with yellow and the old photo set was highlighted with green (See Figure 5.13).

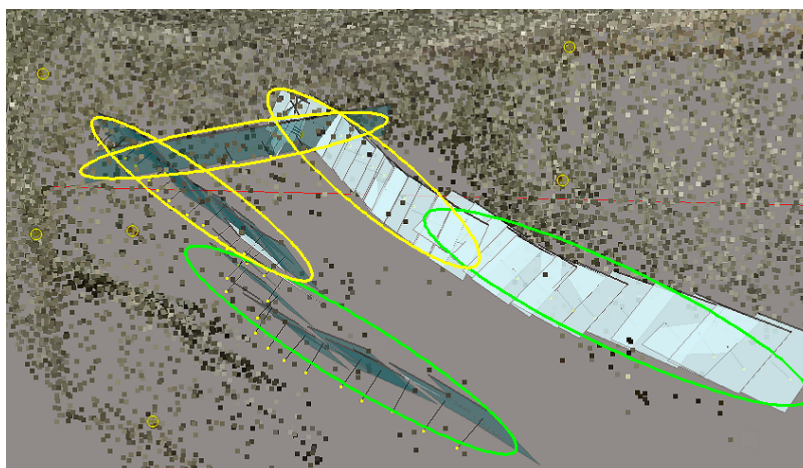


Figure 5.13: 3D view generated in Context Capture after *Aerotriangulation* process consisting of two sets of photos

As it is visible in the figure, approximately two images of each photo set were taken from the same area. The most important factor is to keep continuity of the rows along the walls (without gaps between photo sets), otherwise it increases the change of mismatch between each photo set. The last step was to build the new prolonged 3D mesh model, which was conducted in the same way as it was described for one set of pictures in Chapter 5.2.5.1.

5.2.6 Results - Drift A

During the research period in Drift A, only two blast were performed. Thus, it enabled to catch two sets of photos, resulting in two 3D mesh models produced. Most of the figures presented in the result part of the thesis are generated from screen shots acquired in Context Capture software.

The first model consisted of 44 photos (See Figures 5.14 and 5.15). For eight Ground Control Points the RMS of 3D error (average distance in meters between estimated 3D position of the GCP in the model and surveyed values of GCP coordinates) was equal to 0.004m (horizontal error 0.004m, vertical error 0.001m), meaning that the accuracy of bundle adjustment is within 4mm. This indicates high precision of georeferencing.

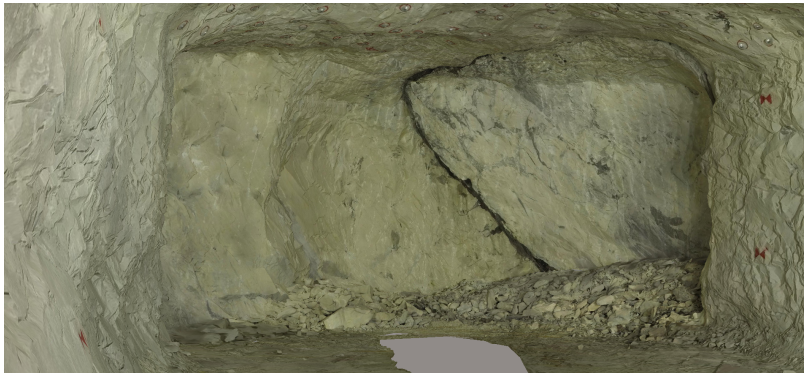


Figure 5.14: The inside view of the first model in Drift A

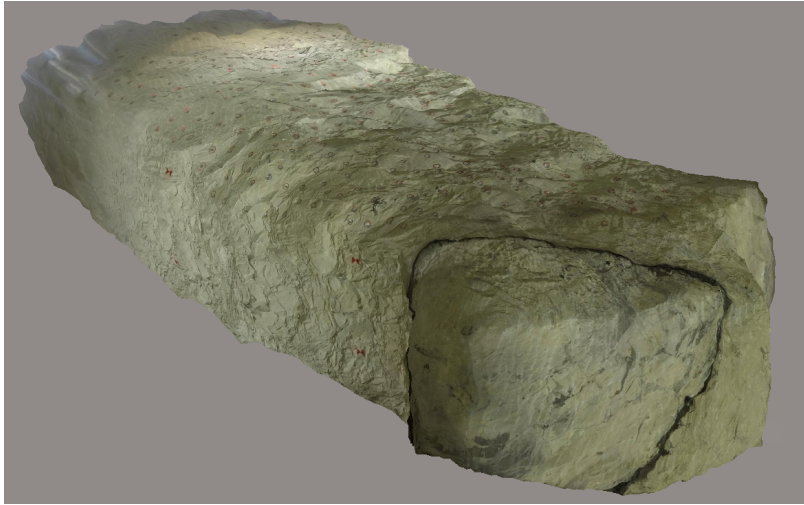


Figure 5.15: The outside view of the first model in Drift A

The second (prolonged) model consisted of 66 pictures (26 from the first set and 40 from the second set of photos). Unfortunately, the second photo set was acquired with use of another drilling rig (less number of LED lamps available) which provided poorer light conditions. However, it was possible to match these two photo sets together. Again, for eight GCP the RMS of 3D error was equal to 0.004m (horizontal error 0.004m, vertical error 0.001m). Meaning that the accuracy of bundle adjustment for the first and second model is extremely similar since the same photos were applied in the georeferencing process. The second model is shown in Figures 5.16 and 5.17.



Figure 5.16: The inside view of the second model in Drift A

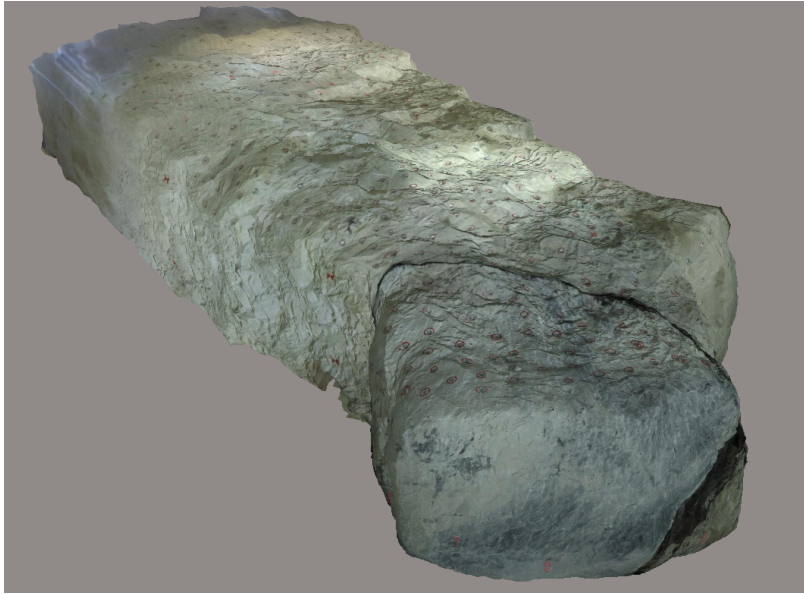


Figure 5.17: The outside view of the second model in Drift A



Figure 5.18: The difference between the first and the second model of Drift A showing progress of exploitation works (top view)

In order to comment on the accuracy of mapping with use of the 3D model, there were six Check Points (101-106) painted on the front face right before the second set of photos in Drift A was captured. The location of the Check Points in Drift A is presented in Figure 5.19. The Check Points were measured from a free station connected to the fix points (FM7002 and FM7003) installed in a nearby area. As a result, coordinates of the Check Points were collected and their accuracy was equal to +/- 1 cm, which was based on total station accuracy.

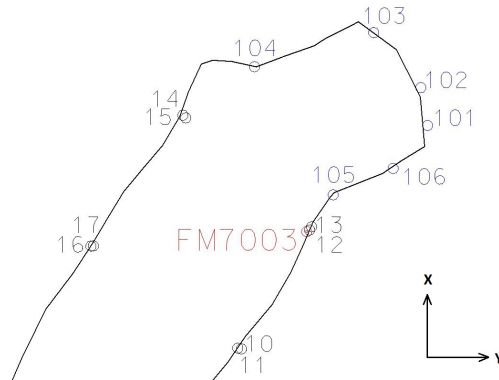


Figure 5.19: The location of Check Points in Drift A

As the coordinates from surveying were the most reliable and the most accurate, they were treated as reference values during the comparison with coordinates delivered by the model. The model coordinates were extracted from the software by pointing on five photos displaying each Check Point. The precision of pointing on the Check Points in each photo was around +/- 1 cm. For each Check Point, the residuals of X, Y and Z coordinate were calculated by a simple evaluation: the value of the model coordinate subtracted from the coordinate obtained by the survey. The residuals on the Check Points are shown in Table 5.1.

Table 5.1: The residuals on the Check Points in Drift A

Point number	Residuals = Model Coordinate - Survey Coordinate		
	Delta X [cm]	Delta Y [cm]	Delta Z [cm]
101	5.4	-2.7	2.7
102	4.9	-4.2	2.3
103	4.3	-5.9	1.9
104	0.7	-6.9	2.4
105	1.9	-2.8	3.9
106	2.3	-1.2	3.6

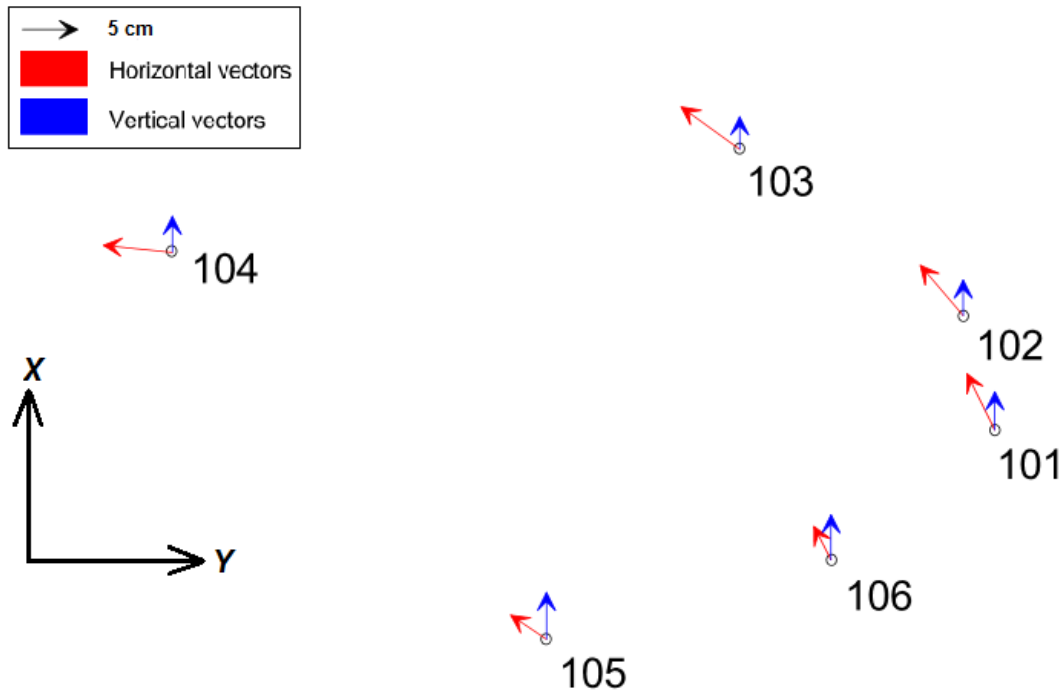


Figure 5.20: Vectors presenting the residuals on the Check Points in Drift A

As it is presented in Table 5.1, the maximum horizontal residual is noticed on Check Point 104 since the Y coordinate reaches around -7 cm. While, the maximum vertical residual appears on point 105 and presents value equal to +3.9 cm. The Figure 5.20 clearly shows that the horizontal vectors for every Check Point tend to northwest direction. In addition, another tendency concerning the vertical residuals is noticeable since all of the points are going upwards. Another observation is that the values of vertical residuals are mostly smaller in comparison with the horizontal ones, despite values represented by points 105 and 106.

As the accuracy of surveyed coordinates and the precision of extracting model's coordinates is within ± 1 cm, it is fair to announce that the differences in coordinates on the Check Points in Drift A are rather significant. This example could give some kind of indication concerning the accuracy of mapping with the model after two blast which would be close to ± 7 cm in the horizontal plane (to base this statement only on those six Check Points) and ± 4 cm in vertical plane. However, these values of residuals are not reliable in terms of assessing the accuracy of mapping with 3D models due to the fact that the different lighting system applied for the second set of photos. The matching between the two photo sets was not performed so accurately and this is probably the main reason why the residuals were reaching quite large values both in the vertical and horizontal planes only after the two blasts.

5.2.7 Results - Drift B

The first model consisted of 60 photos. For eight GCP the RMS of 3D error (average distance in meters between the estimated 3D position of the GCP in the model and surveyed values of GCP coordinates) was equal to 0.003m (horizontal error 0.002m, vertical error 0.003m). Meaning that the accuracy of bundle adjustment is around 3 mm. The first model is presented in Figure 5.21.

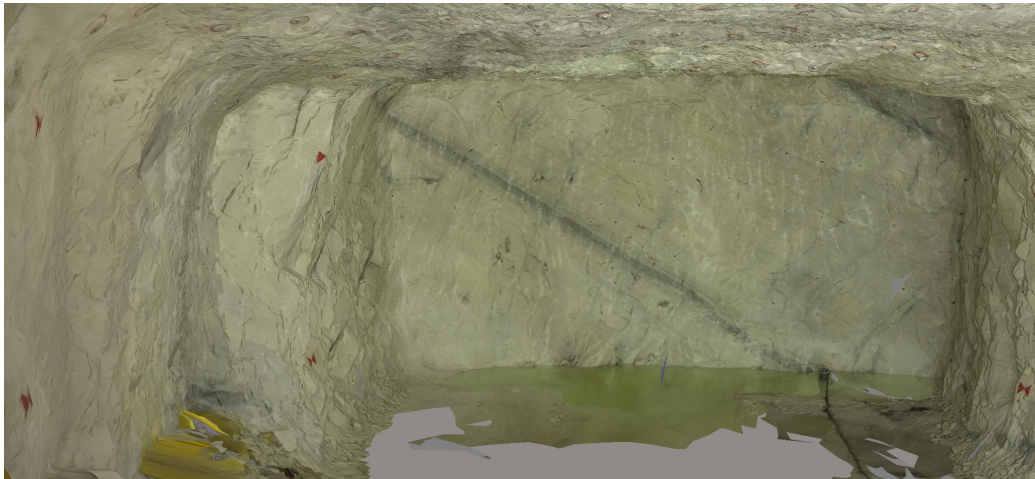


Figure 5.21: The inside view of the first model in Drift B

The second (prolonged) model consisted of 68 pictures (28 from the first set and 40 from the second set of photos). Again, for eight GCP the RMS of 3D error was equal to 0.004m (horizontal error 0.003m, vertical error 0.003m). Meaning that the accuracy of bundle adjustment for the first and second model is extremely alike since the same photos were applied in the georeferencing process. The second model is portrayed in Figure 5.22.

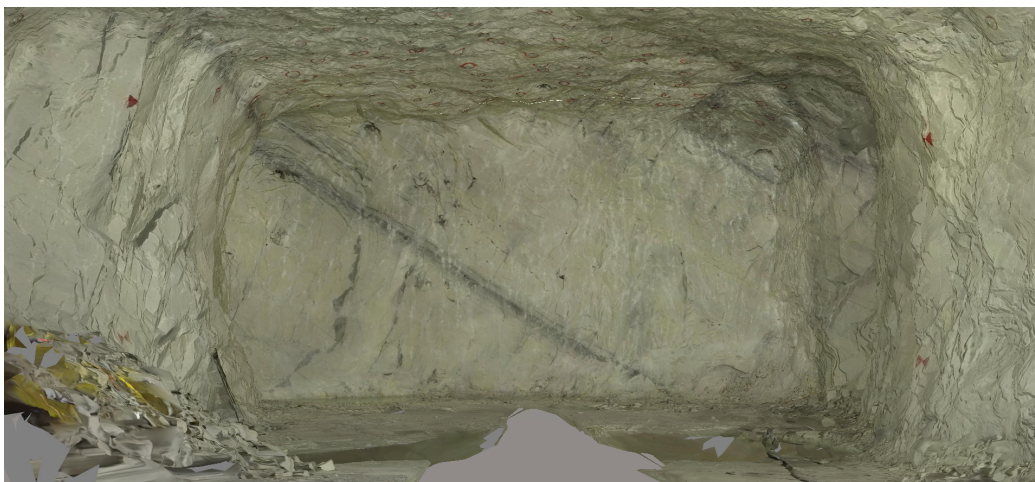


Figure 5.22: The inside view of the second model in Drift B

The third (prolonged) model consisted of 81 pictures (28 from the first set, 12 from the second set, and 41 from the third set of photos). Again, for eight GCP the RMS of 3D error was equal to 0.004m (horizontal error 0.003m, vertical error 0.003m). The accuracy of bundle adjustment for the first, second, and third model differs within milimeters however, the value did not exceed 5 mm for any of them. The third model is shown in Figure 5.23.

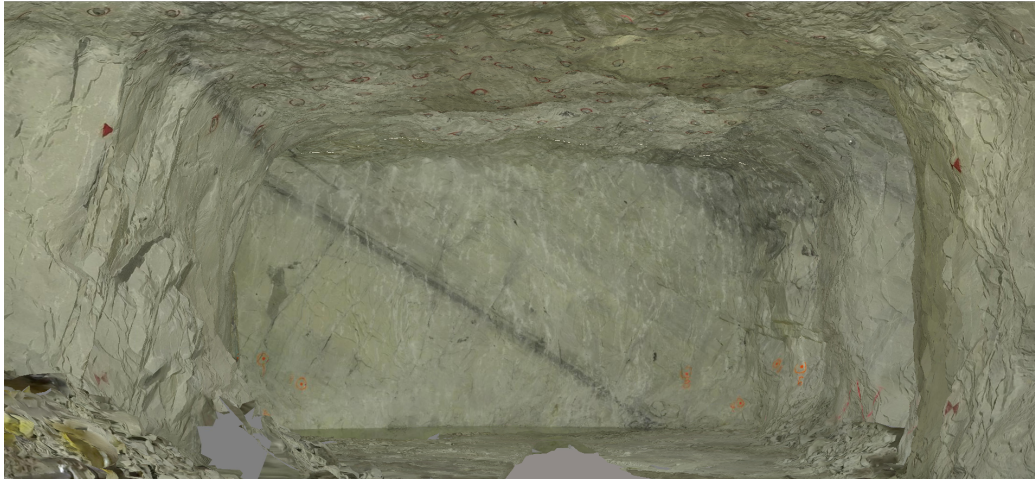


Figure 5.23: The inside view of the third model in Drift B

The best visibility of the progress of exploitation works is provided by the top view of each model. Actually, that could be the way of presenting the mine map. While the new area appearing on every next model is measured in fact it portrays the distance value close to 5 m. Thus, the assumed value by the mine to excavate 5 m during each blast is the real one.

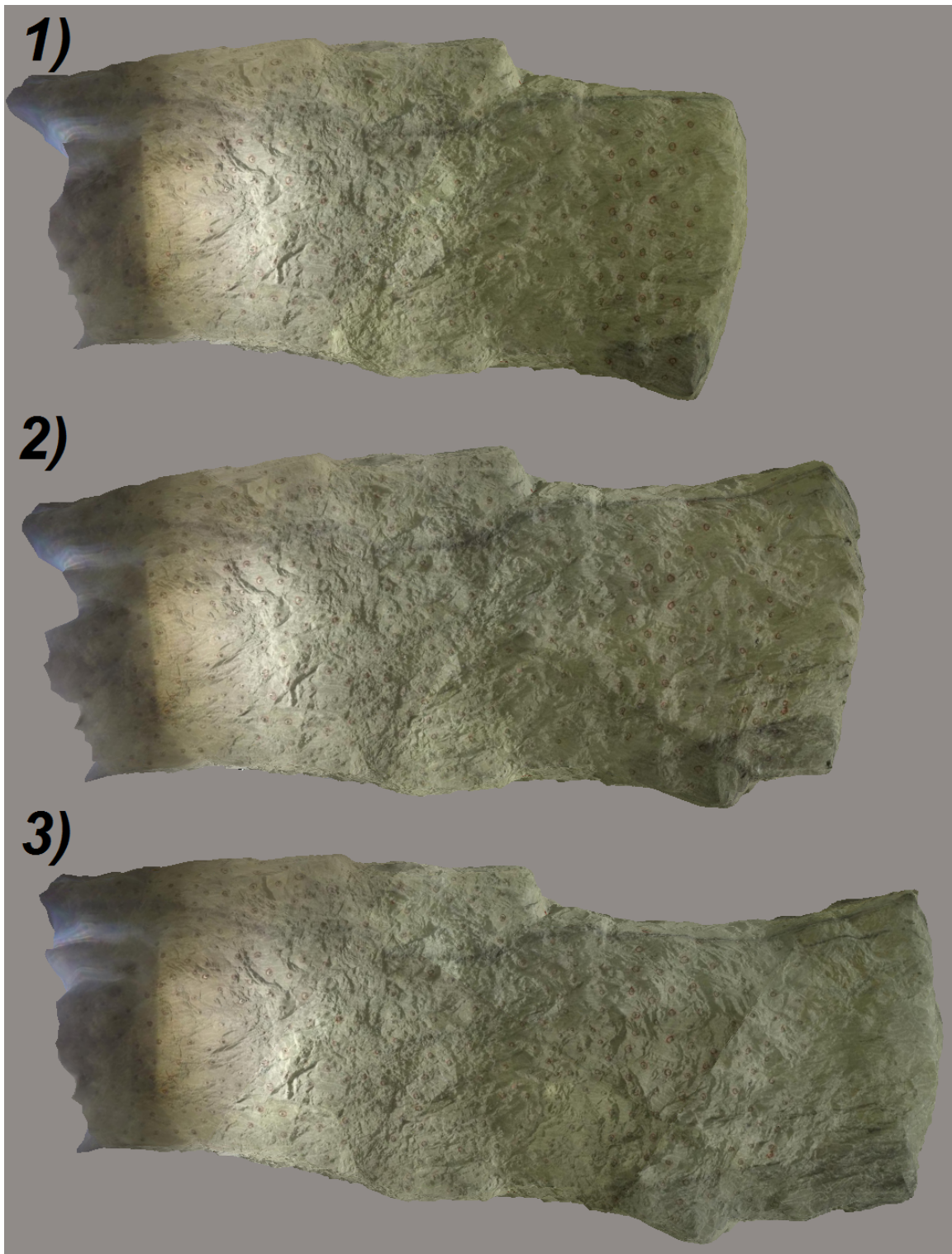


Figure 5.24: The difference between the three models of Drift B showing progress of exploitation works after each blast (top view)

In order to comment on the accuracy of mapping with use of the 3D model, there were eight Check Points (51-58) marked on the front face right before the third set of photos in Drift B was captured. The location of the Check Points in Drift B is presented in Figure 5.25. The Check Points were measured from a free station connected to the fix points (FM7000 and FM7001) installed in a nearby area. As a result, coordinates of the Check Points were collected and their accuracy was equal to +/- 1 cm, which was based on total station accuracy.

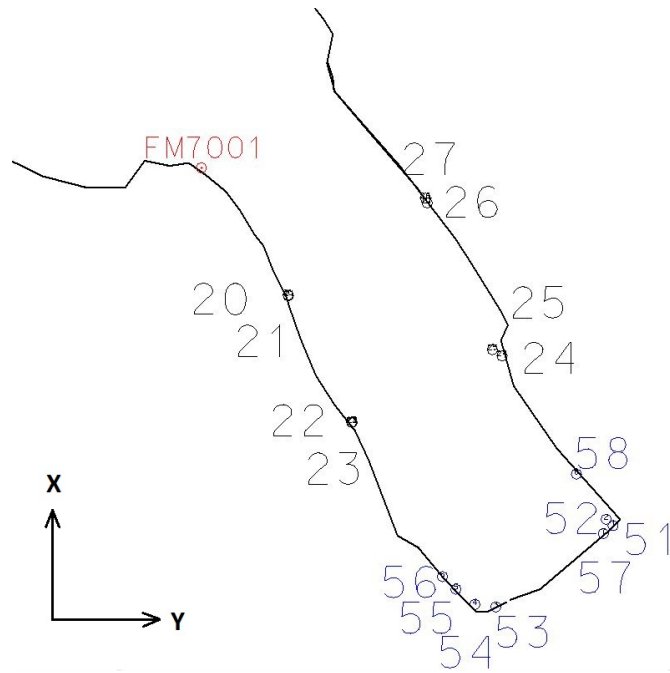


Figure 5.25: The location of Check Points in Drift B

As the coordinates from surveying were the most accurate, they were treated as reference values during the comparison with coordinates delivered by the third model. The model's coordinates were extracted from the software by pointing on five photos presenting each Check Point. The precision of pointing on the Check Points on the photos was around +/- 1 cm. For each Check Point the residuals of X, Y, and Z coordinates were calculated. It was performed by simple evaluation: the value of the model coordinate subtracted from the coordinate obtained from the survey. The residuals on the Check Points in the drift B are shown in Table 5.2.

Table 5.2: The residuals on the Check Points in Drift B

Point number	Residuals = Model Coordinate - Survey Coordinate		
	Delta X [cm]	Delta Y [cm]	Delta Z [cm]
51	-1.8	-1.1	-0.6
52	-1.2	-1.9	-0.1
53	-1.4	-2.4	-0.9
54	-1.2	-2.1	-0.7
55	-1.5	-2.2	-1.3
56	-1.0	-1.3	-1.0

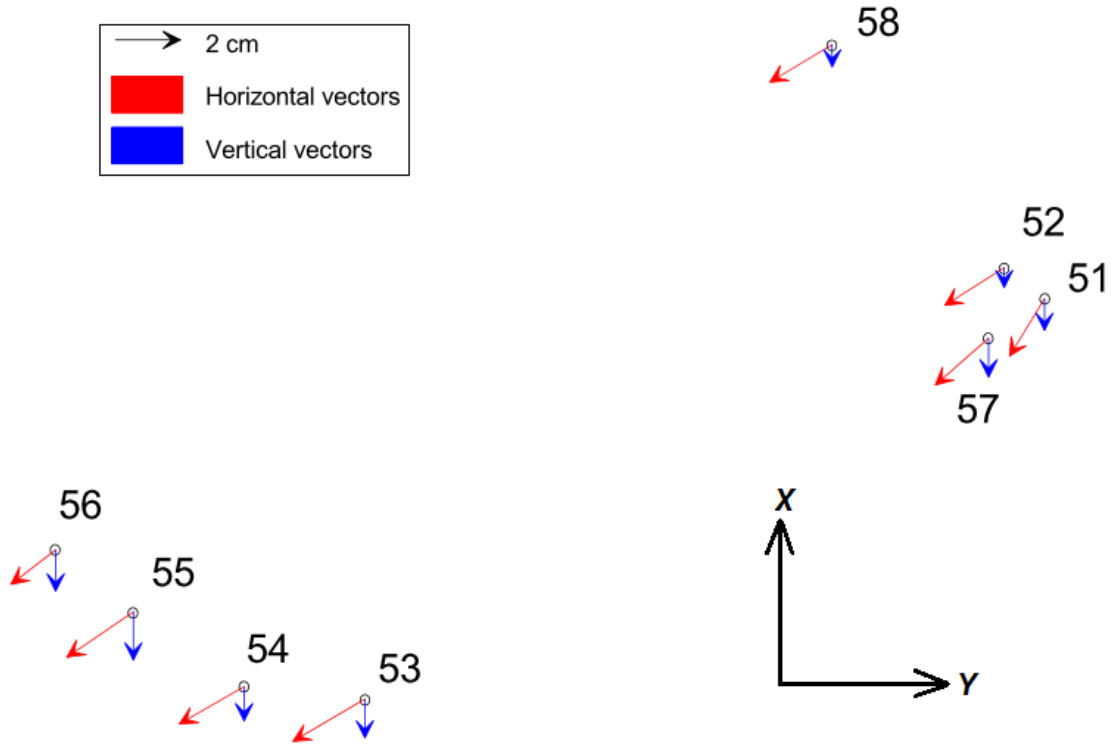


Figure 5.26: Vectors presenting the residuals on the Check Points in Drift B

As it is presented in Table 5.2, the maximum horizontal residual is observed on Check Point 53 where the Y coordinate reaches 2.4 cm. While, the maximum vertical residual appears on point 55 and is equal to 1.3 cm. Figure 5.26 obviously shows that the horizontal vectors for every Check Point tend towards southwest direction. In addition, all of the points are floating downwards, which is opposite direction to the example in Drift A (See Chapter 5.2.6). Once again, it is noticeable that the values of vertical residuals on all of the Check Points are smaller in comparison with values of horizontal residuals. Any significant jumps in the values of the residuals are not noticeable. The magnitude of the residuals is approximately on the same level and

they vary within the interval 0.1-2.4 cm.

The accuracy of the survey coordinates and the precision of extracting the model's coordinates is within ± 1 cm. The values of residuals on the Check Points are rather close to that value, so it is hard to assess whether the differences are significant or not. As a consequence, the accuracy indicator cannot be clearly stated. Nonetheless, the residuals show that the results after three blasts are really promising in terms of using this method as a tool for updating the mine map. Furthermore, the model's coordinates are fairly close to the accuracy given by the total station measurement.

5.2.8 Comments

Both in Drift A and in Drift B, the tendency of horizontal vectors shows drifting towards one direction, which is noticeable on all of the Check Points at once. However, the directions vary between each set of Check Points in Drift A and B. It is rather distinct that both drifts are bending into a direction specific for themselves. In those two examples the direction is different, thus it probably varies from model to model. Additionally, in both cases the vertical residuals were smaller than the horizontal ones.

The magnitude of residuals is clearly higher on the Check Points in Drift A, even though there were only two blasts performed. This indicates that the distance from the Ground Control Points is shorter than in the Drift B. By comparison, the values from Drift A and B prove that the suspicions about different light conditions were right. The large values of residuals in Drift A are caused by changed light conditions for the second set. This is a perfect example of why the provided lighting in each photo set should be performed with the same number and type of lamps. Otherwise, the accuracy of mapping with the model drastically decreases. Even though the residuals are quite large at least in Drift A, the values do not exceed tolerances imposed by the mine in terms of mapping accuracy.

All in all, the procedures in Drift B were performed in accordance with the preliminary ideas. The values bring extremely promising results obtained with this method, as after three blasts, the residuals were reaching centimeters which were close to the accuracy provided by the total station measurement. It could be extremely interesting to observe the residuals after performing more blasts as it was assumed for this research. Nonetheless, for this short distance mapped with the 3D model, the accuracy is surprisingly high.

Finally, the questions stated in the task description can be partly answered. As the previous chapters in this thesis show, it is possible to extend models of a drift with new sets of photos taken before the next blast and the procedure on how to achieve was described previously.

The answer of how many sets can be joined is difficult to find as the obtained results from Drift A and B were satisfying, and did not exceed tolerance limits for mapping. In addition, it is hard to determine an answer because the higher number of captured blasts in one drift was expected, whereas only three blast in the Drift B and two in the Drift A were caught. This slow progress of exploitation works in one particular drift during the research period was due to many faces in production as well as some geological problems in a couple of the drifts appeared.

To provide any indication about the accuracy of mapping a longer part of the drift, it was decided to perform another test in an already excavated drift. This was performed by exploiting the same idea with locating the Ground Control Points (georeferencing) in the beginning of the model, and observing the residuals on the Check Points placed at the end of the model (after mapping a longer distance). The test in the already excavated drift cannot be treated as the case with prolonging the drift's model since there is no excluding photos applied as well as no need to re-build the model after every blast. However, the main idea is quite similar since the further from the location of Ground Control Points the model surface reaches, the longer way of extrapolation and relying on photo matching is needed. The test performed in the already excavated drift will be described in Chapter 5.3.

5.3 Mapping the already excavated drift

Due to the high number of faces in production during the stay in the mine, it was impossible to capture data presenting long parts of a drift mapped with use of 3D models. Therefore, it was decided to check the accuracy of mapping the already excavated drift by using georeferenced points placed only at the beginning of the 3D model. For that reason, the coordinates of the Ground Control Points (20-27) marked in Drift B were used for this purpose.

Since the drilling rig was occupied, there was a need to employ our own lighting system. Thus, two LED lamps mounted on tripods were applied. The one lamp produced 8100 lumens and its opening angle was equal to 45 degrees, while the color temperature was described as 6000K+. Two attempts were accomplished during the research and they introduced two variants of lighting up the drift. Both tries were utilizing the same camera settings as it was presented in Chapter 5.2.4. The particular attempts will be described in Chapter 5.3.1.

5.3.1 First attempt

The data acquisition pattern was extremely similar to the one which was applied in Chapter 5.2.4. Thus, the two rows of tilted images were set along the drift direction covering the right and left sides of the drift separately. The cross cuts appearing on the way were photographed in an additional row resembling a semicircle directed

inside the cross cut. During the collection phase of the photos, the base distance between the photos was 1-1.8 m, while the object distance to the wall varied from 10-14 m.

The lamps were placed around 10 m apart from each other, and the light was pointing in a perpendicular direction to the wall (across from the drift's direction). Meanwhile, the images were captured along the line defined by the lamps. The process of capturing the images started right in front of the first lamp and then continued until the camera reached the second lamp. Subsequently, the first lamp was moved to the new place. The sequence was repeated until one side of the tunnel was photographed. The same procedure was completed in order to obtain the second side of the drift. In consequence, the set of photos consisted of 215 tilted photos.

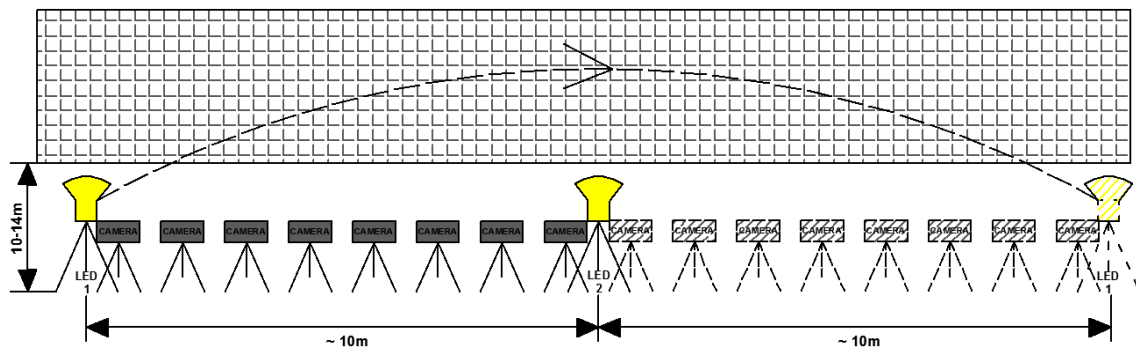


Figure 5.27: The data acquisition pattern performed during the first attempt

Data processing was conducted in the same way as it was described in Chapter 5.2.5.1. Unfortunately, it was impossible to merge the two rows of photos during the *Aerotriangulation* process as it was most likely caused by dark areas near the edges. These dark areas in the photos covered essential ceiling parts where the matching between the two rows was supposed to be performed. This resulted in insufficient overlap and the reconstruction was inaccessible.

Afterwards, it was proposed to try acquiring additional row of photos presenting only the ceiling. For that reason, the additional row was captured in the middle of the drift and vertical images (camera pointing in zenith direction) were captured every 5 m along the drift direction. However, this intervention did not solve the problem of matching both sides of the drift together. Some of the additional pictures presenting the ceiling were matched only with one side of the drift.

Nonetheless, using the acquired pictures as two separate sets of photos (each set represented by the row presenting the left and right side of the drift separately), it was possible to build two georeferenced 3D mesh models presenting each side of the drift. In order to generate the models, the same procedure in Context Capture was applied

as it was described in Chapter 5.2.5.1

First, model presenting left side of the drift (See Figure 5.28) was produced with 100 images and georeferenced with four Ground Control Points (20-23). While, second model portraying the right side of the drift (See Figure 5.29) was generated with 115 photos and was georeferenced with use of four Ground Control Points (24-27).

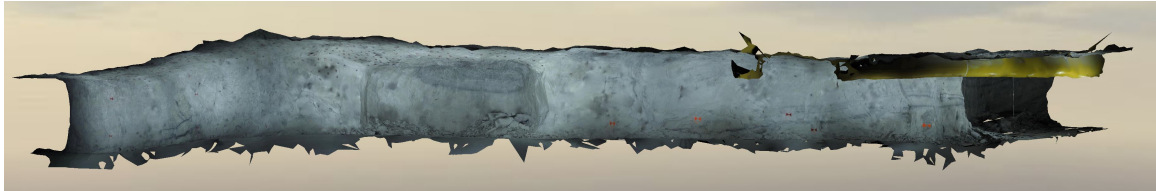


Figure 5.28: Model presenting the left side of the drift

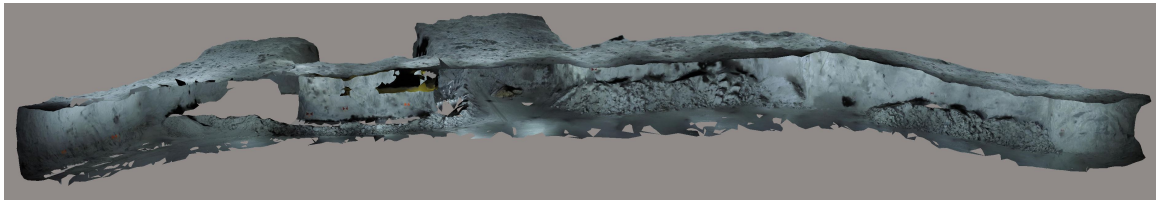


Figure 5.29: Model presenting the right side of the drift

As the resulting models show, the geometry of the tunnel is mostly preserved. Due to the fisheye lens in the GoPro camera, the Field of View allows to cover a larger area, which particularly is an important advantage. However, in this case the two LED lamps were lightening up only a part of the area covered by a single picture. Regardless, it was possible to perform bundle adjustment and match the photos together. Nonetheless, dark sides affected the visual effect of the model. The texture does not show the real situation any longer, which could lead to misunderstandings concerning geology information, as an example in Figure 5.30 is presented.

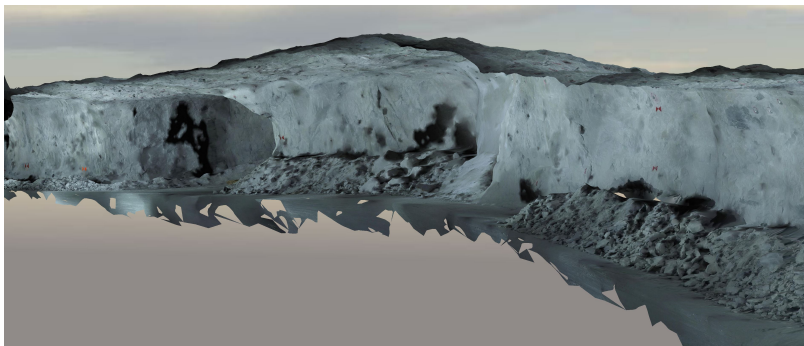


Figure 5.30: Low-quality texturing due to poor light conditions

The distance of 10 meters between the lamps was used due to the fact that larger distances brought visible gaps in the lightening in the middle of the photographs. The approach with lights pointing in the wall's direction could have been more effective if more LED lamps were applied (at least three). This procedure could enlarge the floodlit area. Therefore, it was decided to change the lamp locations and data capture system which will be further explained in Chapter 5.3.2.

5.3.2 Second attempt

Applying the experience from the first attempt there was a need to light up the scene in a more efficient way. For a change, the lamps were pointed along the drift direction (See Figure 5.31) generating a stable light condition on a longer distance (reducing the area of dark sides on the pictures). The lamps were placed around 10 meters from each other close to the walls. The picture acquisition was started approximately six meters away from the line defined by the two lamps and then when the distance between camera and lamps exceeded approximately 18 meters, the positions of lamps were changed by moving them to the new place five meters apart from the last camera position. This kind of loop was repeated until the whole drift was photographed.



Figure 5.31: Setup of the LED lamps during the second attempt

To ensure better overlap, the pattern of capturing pictures slightly changed. On that account, as an addition to the previous approach (using one row presenting each side of the drift), it was extended to two rows per one side of the drift. As a result, tilted images were acquired in four rows. Two rows in the middle of the drift and two on the sides (close to the walls) as is presented in Figure 5.32. The distance between photo stations varied from 1.5-2.5 m, while the object distance varied from 6-14 m. Capturing crosscuts was applied exactly in the same way as it was done in the first

attempt by taking pictures in a semicircle. The whole photographing process lasted around 1.5 hours and during that time 351 photos were captured.



Figure 5.32: Data acquisition pattern during the second attempt

5.3.3 Results and comments

The model presents a 180 m long drift that was generated by the Context Capture that was applied in the same approach described in Chapter 5.2.5.1. The model was built on the photo set that consisted of 351 images (See Figures 5.33; 5.34; 5.35 and 5.36). Georeferencing was performed with use of seven Ground Control Points (20-24 and 26-27) located in Drift B since point number 25 was destroyed. For these seven Ground Control Points, the RMS of 3D error (average distance in meters between estimated 3D position of the GCP in the model and surveyed values of GCP coordinates) was equal to 0.004m (horizontal error 0.004m, vertical error 0.001m). Those values indicate high precision of georeferencing.

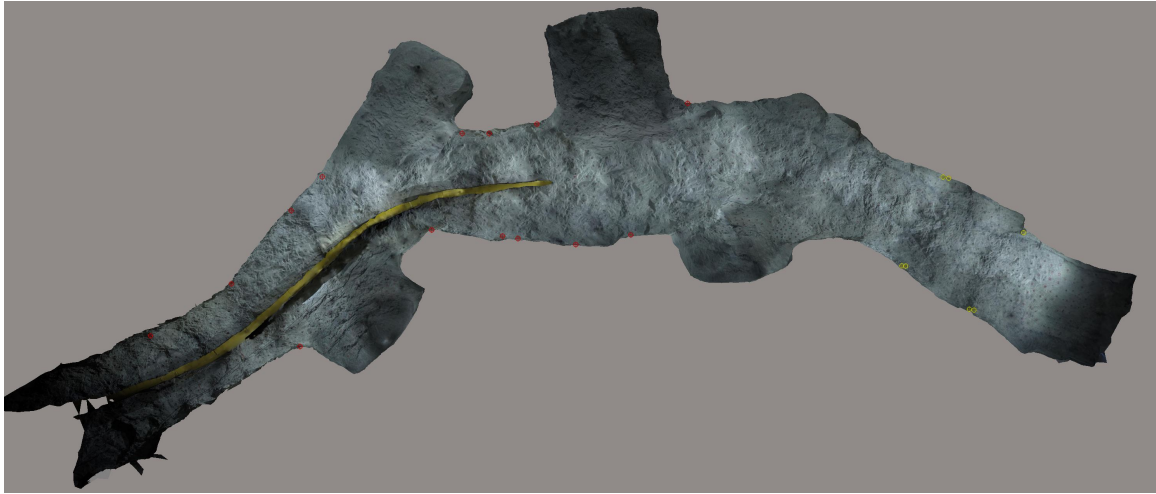


Figure 5.33: Top view of the drift's model with Check Points' location



Figure 5.34: Side view of the drift's model

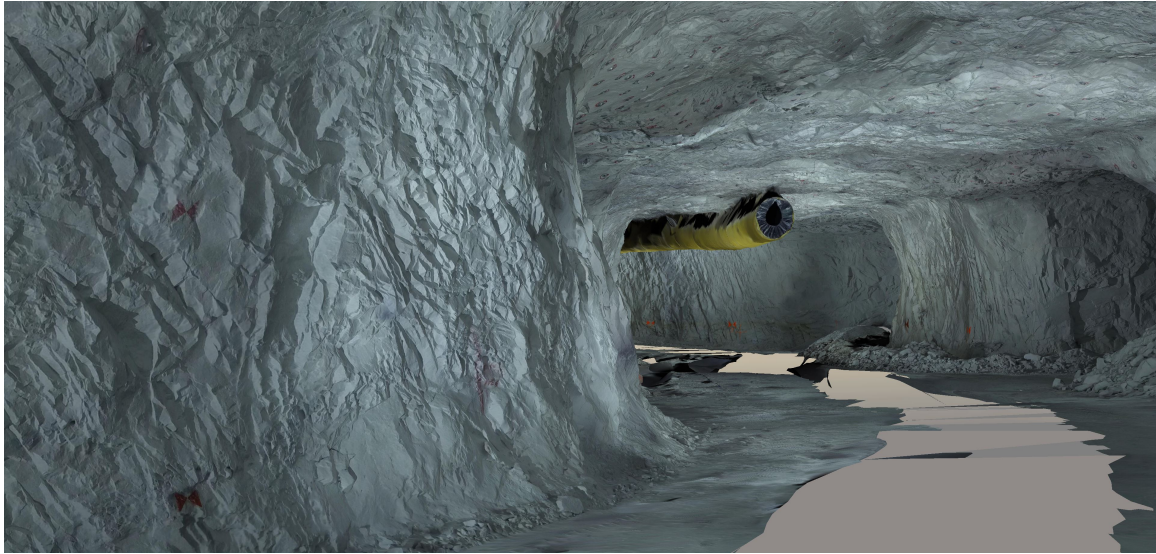


Figure 5.35: Inside view of the drift's model

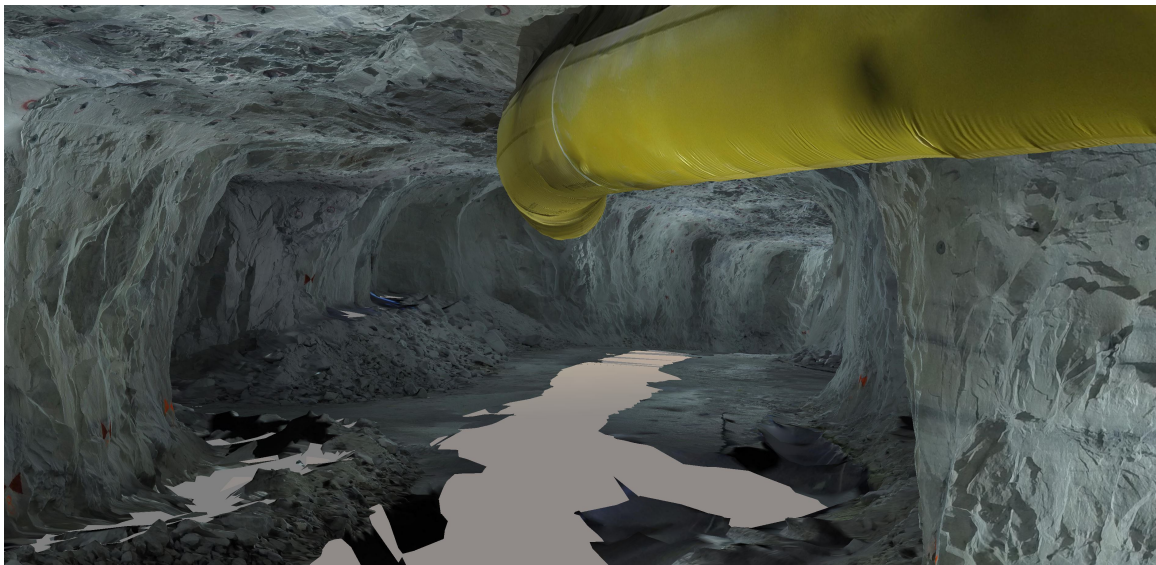


Figure 5.36: Another inside view of the drift's model

In order to comment on the accuracy of mapping with 3D mesh models, it was decided to paint 15 Check Points (1-15) on the walls along the drift before the photo set was captured. The location of the Check Points is portrayed in Figure 5.37. Their coordinates were collected using reflectorless measurements from free stations connected to the two fix points (FM7000 and FM7001). The accuracy of resulting coordinates is equal to ± 1 cm, which was based on total station accuracy.

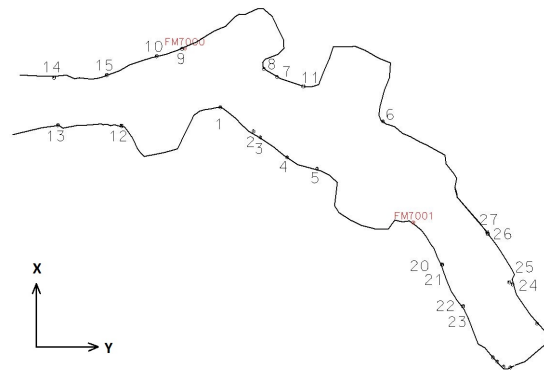


Figure 5.37: Location of the Check Points in the drift

As the coordinates from surveying were the most accurate, they were treated as reference values during the comparison with coordinates delivered by the drift's model. The model coordinates were extracted from the software by pointing on five photos presenting each Check Point, while the precision of pointing on the Check Points on the photos was around +/- 1 cm. It was impossible to obtain the model coordinates for the Check Point number 13 due to shadow, thus it was skipped in the comparison procedure. The residuals of coordinates X, Y, and Z were calculated on each Check Point. The evaluations were done by subtracting the value of the model coordinate from the coordinate obtained from the survey. The residuals on the Check Points in the drift are presented in Table 5.3.

Table 5.3: The residuals on the Check Points in the drift

Point number	Residuals =		
	Model Coordinate - Survey Coordinate		
	Delta X [cm]	Delta Y [cm]	Delta Z [cm]
5	2.5	-5.6	-2.4
6	3.0	-5.3	-2.1
4	2.0	-6.9	-2.2
11	5.3	-6.2	-2.1
2	3.6	-7.8	-1.5
3	3.3	-7.8	-1.9
7	4.2	-7.9	-1.8
1	6.2	-7.2	-2.3
8	3.7	-9.0	-1.6
9	10.3	-10.4	-0.8
10	6.6	-10.7	0.2
12	1.7	-10.9	1.4
15	3.6	-13.2	1.3
14	2.9	-15.9	2.7

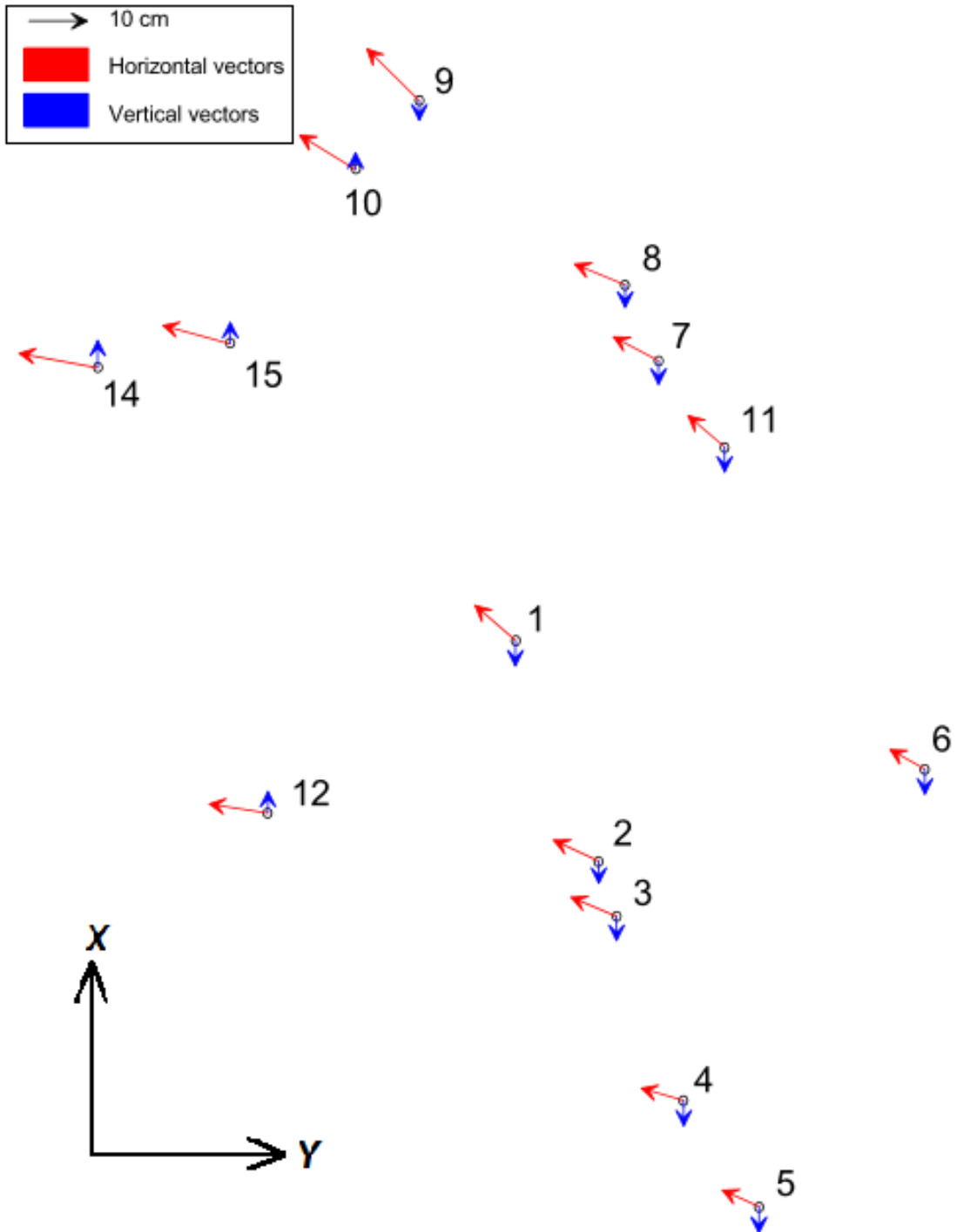


Figure 5.38: Vectors presenting the residuals on the Check Points in the drift

According to Table 5.3 the maximum horizontal residual is noticed on Check Point 14 where it reaches almost 16 cm for the Y coordinate. Moreover, the same Check Point represents the maximum vertical residual, it equal to 2.7 cm, and it is located the furthest from the Ground Control Points. The order of the Check Points in the Table is not random since it is arranged by the location of the Check Points in the drift from the closest to the farthest counting from the location of the Ground Control Points. Thus, it is easily observable that the values of residuals for the Y coordinate are rising with the distance from the GCP. There is one jump noticeable in residuals of coordinate X, which belongs to Check Point number 9. The jump could have been caused by a mismatch of one of the photos where the model's coordinates were extracted.

Figure 5.38 shows that every horizontal vector tends to point in the northwest direction. However, different tendency of the vertical residuals is demonstrable, the Check Points (1-9 and 11) located before the drift's turn go downwards, while the Check Points (10-15) placed just round the corner float upwards. The values of vertical residuals on all of the Check Points are smaller to compare with values of the horizontal residuals.

The model fairly precisely provides the geometry of the drift however, in terms of color representation, it gives worse results. The model's texture is quite dark due to poor light provided by only two LED lamps. Thus, it could impede distinguishing between some geological structures or assessing the presented rock type or its quality. To sum up, to rely on the model's texture, there is a need to employ better lighting conditions or adjust more precisely the camera's settings.

All in all, the 3D model is bending in one direction. The residuals are increasing when the distance from the Ground Control Points becomes larger. By comparing the magnitude of the residuals with the accuracy of surveyed coordinates (± 1 cm), and the precision of extracting the model's coordinates (± 1 cm) it can be stated that the differences are significant (at least those which are representing residuals in the horizontal plane). Thus, based on the research results the indicator of accuracy of mapping with the 3D model could be provided and is approximately equal to ± 16 cm on the 150 meter long drift. However, the results are surprisingly good regarding poor light conditions provided only by two LED lamps compared with lamps mounted on the drilling rig and such a long distance without adding new Ground Control Points. Additionally, the obtained value does not exceed limits of mapping accuracy imposed by the mine, so this method could be applied by updating the mine map without the surveyors' intervention for 150 m.

It is essential to be aware that some jumps in parts of the model could appear, although that could be assessed only with a more accurate method covering the whole area of the model, for instance, a 3D scanning providing dense point cloud.

5.4 Use of 3D models in other disciplines

3D models bring promising solutions which could be applied in many disciplines, not just mine surveying purposes. The potential is also visible by other workers in the mine. In addition, possessing 3D models of drifts could also help miners cope with their daily duties and improve efficiency especially between different departments in a complex mining company. In this chapter, some simple proposals for applications of 3D models will be presented.

5.4.1 Geological mapping and inspection

Geological mapping is crucial in the mining sector especially in mines with a complex geological setting. Folding, faulting, quality variations, and selective excavation of specific layers are some key aspects. When the geological setting is complex, the use of 3D photogrammetry could be advantageous for various reasons, and especially as a basis for making structural analyses.

Layering

The 3D models enable distinguishing between separate layers and lithology in the rock mass. To prepare geological maps the most essential information concerns the spatial location of a geological layer. The basic parameters which describe the orientation or attitude of a geologic feature are called strike and dip. Approximate values of these parameters could be easily calculated with use of measurements on the georeferenced models instead of visiting a mine.

Each single point on the model possesses 3D coordinates which could be extracted by clicking on it. By extracting the coordinates of three points on the desired layer which is presented on the model, it is possible to define a plane. The plane could represent the approximate spatial location of a geological layer. From that plane which is already oriented in the 3D space, the strike and dip could be evaluated. The idea of designing the plane is portrayed in Figure 5.39.

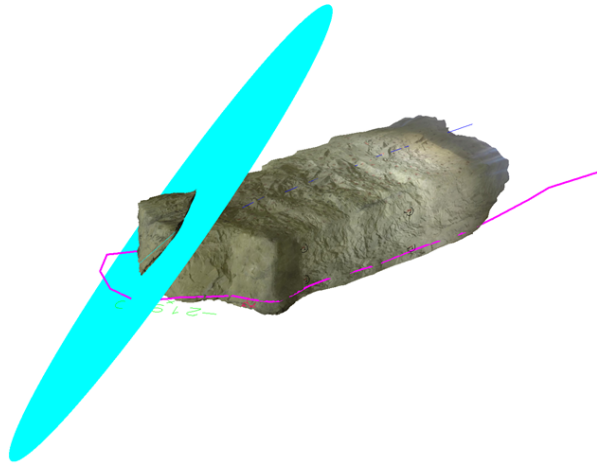


Figure 5.39: Plane portraying approximate course of biotite layer

In addition, georeferenced models enable measuring distance directly on the model's surface as well as the height difference between two defined points. For instance, this procedure could automatically provide information about the thickness of the geological layer.

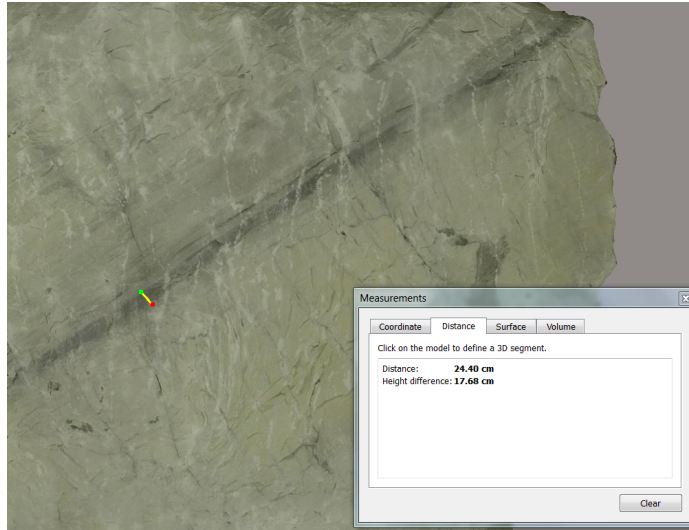


Figure 5.40: Direct measurement of the layer's thickness

Lithology

As long as the light conditions are sufficient, colors presented on models could become more easily distinguished. Based on this information, different colors and textures visible on models could provide elements to assess the rock type (See Figure 5.41). In addition, it could also support characterizing the quality of the rock.

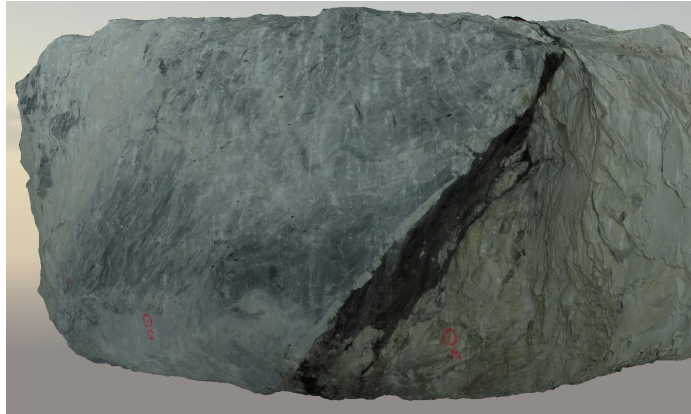


Figure 5.41: 3D models provide information about lithology

Faulting

Faults are geological structures that frequently impede geologists' work. Thus, it is fundamental to predict and interpolate or extrapolate their trajectory. If some unexpected faults appear, they may affect the production cycle and bring financial losses. A good example could be a fault consisting of a biotite layer (See Figure 5.42). When the biotite contaminates the excavated mineral, all the outputs are treated as a waste and cannot be sold to a customer.

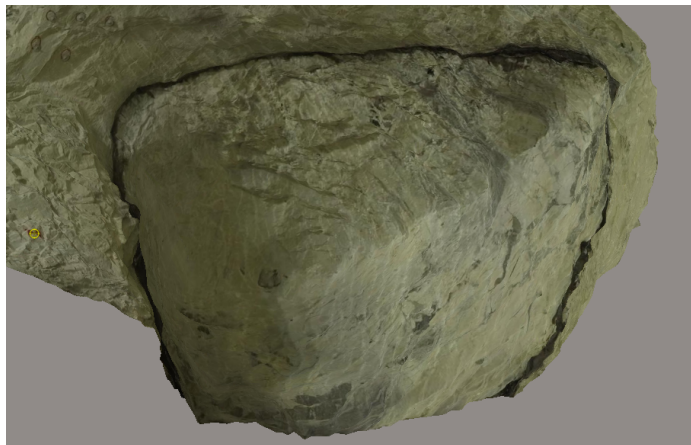


Figure 5.42: Fault consisting of biotite layer

To look on the case globally, by joining together the information about biotite zones with help of models presenting different drifts located within the mine area, it could be possible to interpolate the course of the fault more accurately. This knowledge could be beneficial especially in avoiding those areas during production. Such interpretations are traditionally done by putting together several field maps from the different areas. By applying 3D photogrammetry, this work could be easier and more precise.

Folding

3D models could also enable studying fold structures. This geological feature could be examined by establishing its approximate axial plane as well as the orientation of hinge line. The example acquired in the mine portrays a recumbent fold (See Figure 5.43). Actually, in Figure 5.43 the hinge zone of the fold is visible, which is rather a rare situation.

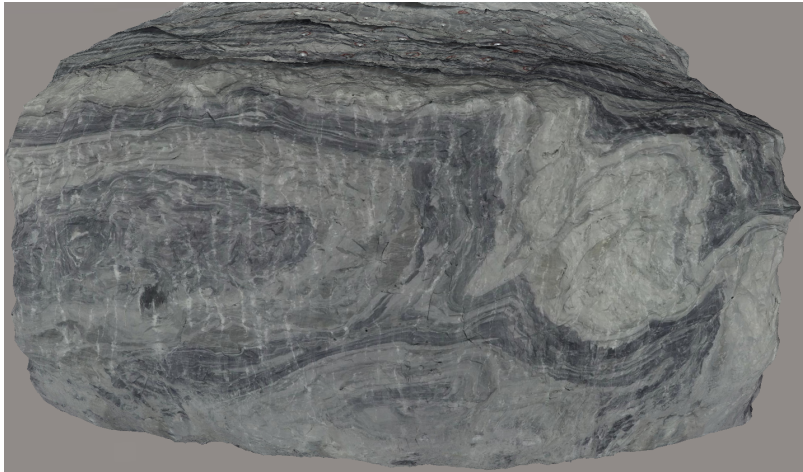


Figure 5.43: Recumbent fold presented on the 3D model

All in all, visibility of geological structures from the outside and inside of models makes it easier to understand, especially if some aberrations appear. Interpretation of the geology becomes more clear while rotating models in 3D view since geologists' skills concerning spatial imagination does not need to be so advanced. Another advantage for geologists could be observing larger areas of a drift instantly at once which is impossible with human eyes during real visits in a mine. Moreover, in a short time it provides a better overview as there is no need to visit specific drifts to gain necessary information.

5.4.2 Documenting rock mechanics problems

Joints, cracks, as well as loosed bolts dangling from a ceiling give first warning signs in terms of work safety conditions. As the level of details presented on 3D models is rather high, it could become a perfect tool for 1) performing analyses (f.ex. joint orientations), and 2) monitoring unintended changes in the drift. The dangerous areas could be easily identified by running through a model (See Figure 5.44). Additionally, by visual comparison of models from different time periods for instance, cracks could become more noticeable when they widen or form any extra joints (See Figure 5.45).

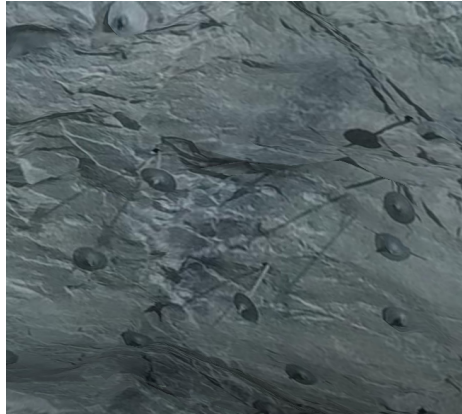


Figure 5.44: Identifying loosed bolts on the ceiling

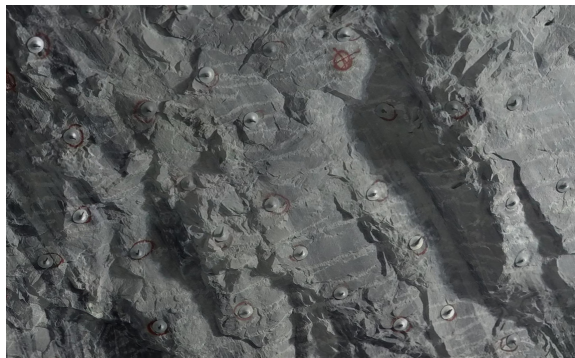


Figure 5.45: Joints clearly visible on the ceiling

Another application of 3D models in underground mines could be used as a tool in the rock mechanics inspection. Since the extensions of pillars and rooms are projected as a balance between safety and efficiency, there are some areas in the mine which demand special surveillance. The most common problem involves the effect of rock mass relaxation. In consequence, pillars tend to compact with time and some parts of the rock fall which effect workplace safety. Thus, it is crucial to obtain precise information and apply it into rock mechanics assessments. At present, the common way of observing changes is conducted by painting or marking the ground area around the pillar or region of interest. Then, if something happens, the amount of rock laying on the ground within the marked area gives an indication concerning the magnitude of changes. Also, the width of cracks measured 3D models could bring a new angle of looking at rock mechanics issues.

The use of 3D models is going to be explained in one example which was captured during research period in mine one. One of the pillars was chosen due to visible rock mechanics issues (some of the cracks were quite wide and some parts of rock were already loosened). It was decided to produce the non-georeferenced model of that pillar. 17 pictures were captured around 5 m from the area of interest in the way

as it is presented in Figure 5.46. The base distance was approximately 1 m. Two LED lamps were situated around 10 m apart from each other and were pointing in the pillar's direction.



Figure 5.46: The way of taking pictures for the pillar's model

The general workload in Context Capture software was applied as it was already described in the thesis (See Chapter 5.2.5). The only difference was that the Ground Control Points were not added into the bundle adjustment process. As a result, the non-georeferenced model was produced and is shown in Figure 5.47.

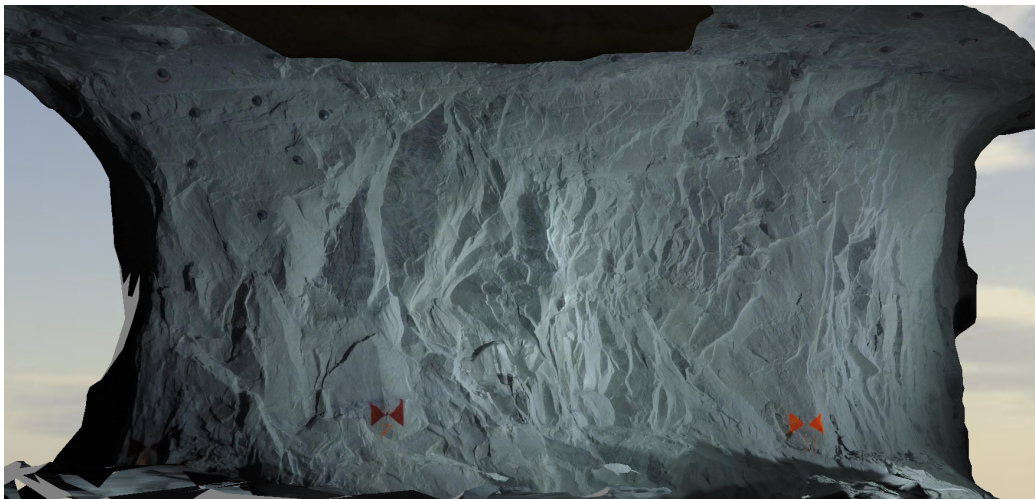


Figure 5.47: Pillar's 3D mesh model

However, as it is visible in the figure, the marks representing three Ground Control Points (the minimum number to georeference a model) were painted on the wall on stable parts of the pillar before the images were captured. This intervention was made on purpose since as long as the pillar is stable, the model could be only archived or used for visual judgments. If some changes within the area could appear then a mine surveyor could measure the Ground Control Points and georeference the

already produced model. Afterwards, the new set of photos presenting the pillar after changes could be captured as a base to build a new georeferenced model presenting the actual situation. Rock mechanics specialists could use those two 3D models to register changes of the pillar by simple comparison. It could be done both ways: by visual comparison or by measurements on the models (for instance, assessing the volume of the changes by applying third part software or identifying the exact place on the pillar where the changes occurred). As joints and cracks on the rock are easily visible, it could also help to predict some unwanted events and especially increase health and safety at the workplace (See Figure 5.48).



Figure 5.48: Loosened rocks stand out from the pillar’s surface

As it is presented in the figures, the model is quite dark due to poor lighting conditions in the mine, but also due to limitations in the camera (the ISO quality on the applied camera is restricted and for this reason the camera requires plenty of light). The photos could have been taken with other settings which light up more accurately the scene or the images could have been enhanced by third party software. Nonetheless, this example was produced only to come up with a proposal of an additional use of 3D models.

However, for more accurate rock mechanics inspection purposes, the accuracy of models itself should be as high as possible to catch even the slightest change in geometry of pillars. Thus, it is recommended to apply more professional DSLR cameras with higher resolution and larger sensor size which could boost the level of details on each model. Additionally, the lighting system should be as powerful as possible to avoid shadows within the area of interest.

5.5 Final comments

The greatest success of this research is that the wrought method of data acquisition in order to generate 3D models from photographs in underground drifts was immedi-

ately implemented by the mine to their daily basic works.

3D models could bring many advantages in the underground mining sector. Especially, in the complex company is considered as kind of organism the communication between different divisions consisting of managers, engineers, miners, planners, health and safety specialists as well as people taking care of logistics and distribution is essential. 3D models would allow actors to persuade necessary improvements or steps, and validate claims to achieve, for instance, investments regarding additional geological drill holes, or implementation of new, more efficient machines, or changing excavating methods. Showing the actors deliberately a part of a mine where some problem appear it would bring better understating since some do not have a real sense of the mine's situation.

In conclusion, the stated tasks proposed by this thesis were partly accomplished. Thus, answering on the first question in the task description: it is possible to prolong 3D model from pictures covering the last part of a tunnel just before drilling and blasting works in order to map exploitation works. The method have come a long way to achieve the goal of taking into account both data acquisition patterns as well as the procedures applied in the software. The improvements and adaptation of the method to different conditions was a quite challenging task, so the experience gained in the test tunnel was invaluable for real time work.

It was observed that the software algorithms properly dealt with distortion caused by the fisheye lens which was essential in reducing the number of photos, while also achieving a sufficient overlap in narrow corridors such as drift or tunnel where the distance to the object is imposed by their extensions. In addition, matching the algorithms applied in the software were also able to cope with different lighting conditions between each set of the photos added into the bundle adjustment. However, different lighting conditions directly affects the accuracy of mapping provided by the model. Thus, it is recommended to employ exactly the same color of light, as well as the number of lamps when acquiring the photos - which will be processed within one bundle adjustment process.

When it comes to the second question stated in the task description concerning the number of sets of pictures which could be joined before a new set of pictures have to be georeferenced unfortunately, low number of acquired sets of photos do not allow to answer it. Higher number of blasts should have been taken in one drift to tell more about the accuracy achieved with a mapping longer part of a drift, while relying only on photo matching. However, based on the results obtained in the research, three sets of photos could give accuracy of mapping close to this which is provided by total station measurements, which gives rather positive expectations for expanding the model with more photo sets.

The additional test conducted in the already excavated 150 m long drift, provided a

kind of accuracy indicator. Based on the achieved results in the thesis, after mapping 150 m with 3D model, the highest value of residuals was equal to 16 cm. Moreover, it is worthy to remind that the Ground Control Points were placed only in the beginning of the model. This value does not exceed the accuracy of mapping imposed by the mine. As a result, this method could be used as an alternative or addition to ordinary surveying. It was also noticed that to obtain more reliable texture on the model, it is recommended to apply an improved lighting system, for instance, by employing lamps mounted on the drilling rig not just using the separate, two LED lamps (See Chapter 5.3). However, as the results show, two LED lamps were sufficient to show the geometry of the drift.

5.6 Future recommendations

As the application of 3D models produced from photographs in underground conditions are in initial research stages, it is recommended to conduct more examinations concerning these topics.

If a mine does not provide light from a rig, it is recommended to use more than just two LED lamps. In addition, to get better model texture a more advanced DSLR camera with a fisheye lens is required. In this sense, the GoPro was not the best option due to some setting limitations.

A more reliable way of assessing the accuracy of models could be performed, for instance, with 3D scanning. This method would give more accurate reference to compare with models obtained by image acquisition. Most importantly, the model could be checked within the whole area, not only on several Check Points as it was performed in this thesis.

Additionally, there could be some studies done concerning the reduction in the number of photos, as well as decreasing the value of overlap between photo sets acquired for every blast in order to get better insight into the accuracy of mapping with 3D models.

A final idea could be to change the method of georeferencing, for example, by increasing or decreasing the number of Ground Control Points, and observing its affect on accuracy.

Bibliography

- AgisoftLLC, 2016. Agisoft PhotoScan User Manual Professional Edition, Version 1.2
URL: http://www.agisoft.com/pdf/photoscan-pro_1_2_en.pdf.
- BentleySystems, 2016. Context capture - quick guide for photo acquisition URL: http://communities.bentley.com/products/3d_imaging_and_point_cloud_software/m/mediagallery/271352.
- CNET, 2016a. Gopro hero4 black specifications. URL: <http://www.cnet.com/products/gopro-hero4-black/specs/>.
- CNET, 2016b. Sony alpha nex-c3 specifications. URL: <http://www.cnet.com/products/sony-alpha-nex-c3/specs/>.
- Colomina, I., Blázquez, M., Molina, P., Parés, M.E., Wis, M., 2008. Towards a new paradigm for high-resolution low-cost photogrammetry and remote sensing .
- Eisenbeiß, H., 2009. UAV photogrammetry.
- Elnima, E.E., 2015. A solution for exterior and relative orientation in photogrammetry, a genetic evolution approach. Journal of King Saud University - Engineering Sciences 27, 108–113.
- Geodetic Systems, I., 2016. The basics of photogrammetry. URL: <http://www.geodetic.com/v-stars/what-is-photogrammetry.aspx>.
- Haugen, S., Ludvigsen, E., 2015. Fra separate fagdisipliner til integrert mineralressursforvaltning i bergindustrien , 19–38.
- Kraus, K., 2000. Photogrammetry. Fundamentals and Standard Processes. Dümmler.
- Mikhail, E.M., Bethel, J.S., McGlone, J.C., 2001. Introduction to Modern Photogrammetry. John Wiley and Sons, Inc.
- Nagai, M., Shibasaki, R., Manandhar, D., Zhao, H., 2002. Development of Digital Surface Model and feature extraction by integrating laser scanner and CCD sensor with IMU , 4–6.

- PAPA-International, 2016. History of aerial photography. URL: http://professionalaerialphotographers.com/content.aspx?page_id=22&club_id=808138&module_id=158950.
- Remondino, F., Barazzetti, L., Nex, F., Scaioni, M., Sarazzi, D., 2011. UAV photogrammetry for mapping and 3D modeling - current status and future perspectives , 14–16.
- Schenk, T., 2005. Introduction to Photogrammetry URL: <http://www.mat.uc.pt/~gil/downloads/IntroPhoto.pdf>.
- Westoby, M.J., Brasington, J., Glasser, N.F., Hambrey, M.J., Reynolds, J.M., 2012. 'Structure-from-Motion' photogrammetry: A low-cost, effective tool for geoscience applications , 300–314.
- Wolf, P.R., Dewitt, B.A., 2000. Elements of Photogrammetry. With Applications in GIS. McGraw-Hill.

Appendices

Appendix A

GoPro calibration report from Agisoft PhotoScan

HERO4 Black (3 mm)
8 images, 4000x3000 pix

Camera type: Fisheye
Pixel size (mm): 0.00173066 x 0.00173066
Focal length (mm): 3

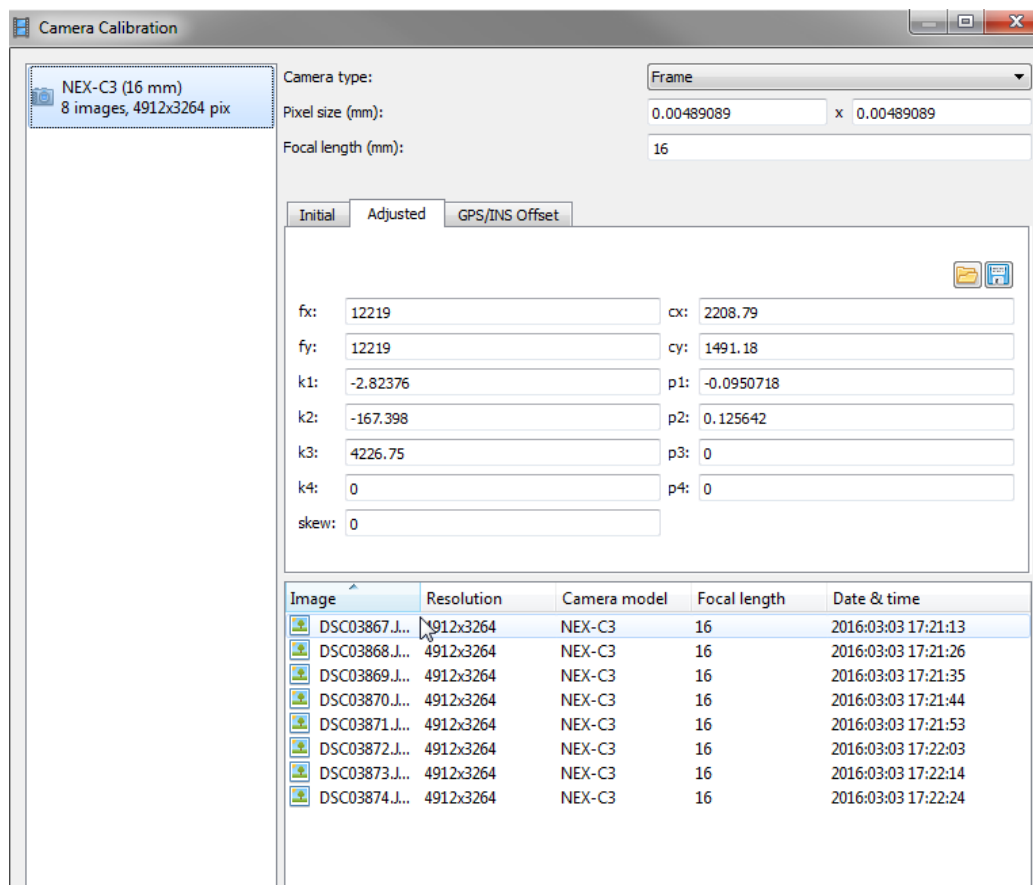
Initial Adjusted GPS/INS Offset

fx: 1378.14 cx: 1925.77
fy: 1378.14 cy: 1452.17
k1: 0.277859 p1: 0.0117093
k2: -0.204114 p2: -0.0273345
k3: 0.0312637 p3: 0
k4: 0 p4: 0
skew: 0

Image	Resolution	Camera model	Focal length	Date & time
GOPR0222.J...	4000x3000	HERO4 Black	3	2016:03:03 16:19:09
GOPR0223.J...	4000x3000	HERO4 Black	3	2016:03:03 16:19:24
GOPR0224.J...	4000x3000	HERO4 Black	3	2016:03:03 16:19:39
GOPR0225.J...	4000x3000	HERO4 Black	3	2016:03:03 16:20:10
GOPR0226.J...	4000x3000	HERO4 Black	3	2016:03:03 16:20:30
GOPR0227.J...	4000x3000	HERO4 Black	3	2016:03:03 16:20:45
GOPR0228.J...	4000x3000	HERO4 Black	3	2016:03:03 16:20:58
GOPR0229.J...	4000x3000	HERO4 Black	3	2016:03:03 16:21:35

Appendix B

Sony calibration report from Agisoft PhotoScan



Appendix C

Report of targets network adjustment in GISLINE software

DATUMPARAMETRE
 System : local
 Lang halvakse [m] : 6377492.018
 Flattrykning [1/f]: 299.1528128500000
 Tangeringsmeridian [deg]: 0.000000000000
 Skalafaktor : 1.000000
 Addisjonskonst. nord [m]: 0.000
 Addisjonskonst. øst [m]: 0.000
 Rotasjon [deg]: 0.000000

INSTRUMENTPARAMETRE
 INSTRUMENT : 1: EDM - 1
 Std.avvik Konstantdel Avstandsavhengig
 Retning : 0.00120 gon 0.0000 gon/km
 Avstand : 0.005 m 0.005 m/km
 Høydeforskjell : 0.000 m 0.020 m/km
 Sentrering Grunnriss : 0.002 m
 Sentrering Høyde : 0.002 m
 Referanseverdier
 Referansetrykk : 760.0 mmHg
 Referansetemperatur : 20.0 C
 Addisjonskonstant : 0.000 m
 Målestokkfeil : 0.000 m/km

TEST AV OBSERVASJONER

DATUM: local

UTJEVNING I 3-D

FRI UTJEVNING

TEST AV OBSERVASJONER - MULTIPPEL T-TEST

Fra	Til		Restfeil	Est.grovfeil	Testverdi
100	1 1	R	-0.00589	0.03897	0.41
100	1 1	D	-0.001	0.001	0.10
100	1 1	dH	0.003	-0.009	1.75
100	1 2	R	0.00396	-0.03040	0.33
100	1 2	D	0.003	-0.003	0.34
100	1 2	dH	0.003	-0.008	1.55
100	1 3	R	0.00920	-0.03347	0.35
100	1 3	D	0.001	-0.002	0.16
100	1 3	dH	0.004	-0.010	2.09
100	1 4	R	-0.00330	0.00906	0.09
100	1 4	D	0.001	-0.003	0.25
100	1 4	dH	0.005	-0.013	2.59
100	1 5	R	0.00000	IKKE KONTROLLERBAR	
100	1 5	D	-0.000	IKKE KONTROLLERBAR	
100	1 5	dH	-0.000	IKKE KONTROLLERBAR	
100	1 6	R	0.00000	IKKE KONTROLLERBAR	
100	1 6	D	-0.000	IKKE KONTROLLERBAR	
100	1 6	dH	0.000	IKKE KONTROLLERBAR	
100	1 7	R	0.00000	IKKE KONTROLLERBAR	
100	1 7	D	-0.000	IKKE KONTROLLERBAR	
100	1 7	dH	0.000	IKKE KONTROLLERBAR	
100	1 8	R	0.01139	-0.02911	0.88
100	1 8	D	-0.001	0.002	0.17
100	1 8	dH	0.000	-0.000	0.01
100	1 9A	R	-0.00000	IKKE KONTROLLERBAR	
100	1 9A	D	-0.000	IKKE KONTROLLERBAR	
100	1 9A	dH	0.000	IKKE KONTROLLERBAR	
100	1 10	R	-0.00334	0.00877	0.53
100	1 10	D	-0.003	0.005	0.42
100	1 10	dH	0.002	-0.004	0.74
100	1 11	R	-0.00152	0.00356	0.22
100	1 11	D	-0.001	0.002	0.16
100	1 11	dH	0.002	-0.005	1.07
100	1 12	R	0.00394	-0.00916	0.58
100	1 12	D	0.000	-0.001	0.05
100	1 12	dH	0.001	-0.002	0.32
100	1 14	R	0.00045	-0.00104	0.10
100	1 14	D	0.001	-0.001	0.09
100	1 14	dH	-0.000	0.000	0.05
100	1 15	R	0.00019	-0.00042	0.04
100	1 15	D	0.001	-0.002	0.18
100	1 15	dH	0.000	-0.000	0.10
100	1 16	R	-0.00093	0.00200	0.19

100	1 16	D	0.001	-0.002	0.17
100	1 16	dH	0.002	-0.004	0.83
100	1 17	R	-0.00121	0.00267	0.34
100	1 17	D	-0.001	0.003	0.22
100	1 17	dH	-0.001	0.001	0.24
100	1 18	R	-0.00038	0.00081	0.10
100	1 18	D	-0.000	0.001	0.07
100	1 18	dH	-0.000	0.001	0.12
100	1 19	R	0.00011	-0.00022	0.03
100	1 19	D	0.001	-0.001	0.10
100	1 19	dH	0.000	-0.001	0.19
100	1 20	R	-0.00214	0.00433	0.58
100	1 20	D	0.001	-0.002	0.18
100	1 20	dH	-0.001	0.001	0.23
100	1 21	R	-0.00074	0.00165	0.25
100	1 21	D	-0.000	0.000	0.04
100	1 21	dH	-0.001	0.003	0.56
100	1 22	R	-0.00104	0.00239	0.36
100	1 22	D	-0.000	0.001	0.07
100	1 22	dH	-0.003	0.006	1.13
100	1 23	R	0.00006	-0.00012	0.02
100	1 23	D	-0.001	0.002	0.13
100	1 23	dH	-0.006	0.010	2.17
100	1 24	R	0.00029	-0.00056	0.09
100	1 24	D	-0.000	0.000	0.01
100	1 24	dH	-0.002	0.003	0.61
100	1 25	R	0.00013	-0.00053	0.07
100	1 25	D	0.001	-0.001	0.12
100	1 25	dH	-0.005	0.009	1.80
100	1 26	R	-0.00070	0.00272	0.37
100	1 26	D	-0.001	0.001	0.08
100	1 26	dH	-0.006	0.010	2.01
100	1 27	R	-0.00019	0.00038	0.07
100	1 27	D	-0.000	0.000	0.03
100	1 27	dH	-0.008	0.014	2.83
100	1 28	R	-0.00256	0.00516	0.99
100	1 28	D	0.003	-0.005	0.42
100	1 28	dH	-0.005	0.008	1.65
100	1 101	R	0.00542	-0.00701	1.79
100	1 101	D	-0.008	0.009	0.90
100	1 101	dH	-0.010	0.010	2.65
101	1 1	R	-0.00049	0.00225	0.29
101	1 1	D	0.003	-0.004	0.38
101	1 1	dH	-0.005	0.009	1.75
101	1 2	R	0.00069	-0.00313	0.40
101	1 2	D	-0.001	0.002	0.15
101	1 2	dH	-0.004	0.008	1.55
101	1 3	R	0.00097	-0.00168	0.35
101	1 3	D	0.001	-0.003	0.21
101	1 3	dH	-0.006	0.010	2.09
101	1 4	R	-0.00025	0.00048	0.09
101	1 4	D	0.002	-0.003	0.24
101	1 4	dH	-0.007	0.013	2.59
101	1 8	R	0.00247	-0.00485	0.88
101	1 8	D	-0.000	0.000	0.03
101	1 8	dH	-0.000	0.000	0.01
101	1 10	R	-0.00171	0.00379	0.56
101	1 10	D	-0.000	0.001	0.06
101	1 10	dH	-0.002	0.004	0.74
101	1 11	R	-0.00072	0.00142	0.22
101	1 11	D	-0.001	0.002	0.18
101	1 11	dH	-0.003	0.005	1.07
101	1 12	R	0.00187	-0.00370	0.58
101	1 12	D	0.001	-0.001	0.11
101	1 12	dH	-0.001	0.002	0.32
101	1 13	R	0.00000	IKKE KONTROLLERBAR	
101	1 13	D	-0.000	IKKE KONTROLLERBAR	
101	1 13	dH	0.000	IKKE KONTROLLERBAR	
101	1 14	R	0.00038	-0.00083	0.10
101	1 14	D	0.000	-0.000	0.03
101	1 14	dH	0.000	-0.000	0.05
101	1 15	R	0.00014	-0.00029	0.04
101	1 15	D	0.001	-0.002	0.18

101	1 15	dH	-0.000	0.000	0.10
101	1 16	R	-0.00074	0.00151	0.19
101	1 16	D	0.001	-0.002	0.16
101	1 16	dH	-0.002	0.004	0.83
101	1 17	R	-0.00174	0.00413	0.35
101	1 17	D	-0.000	0.000	0.02
101	1 17	dH	0.001	-0.001	0.24
101	1 18	R	-0.00054	0.00126	0.11
101	1 18	D	-0.000	0.000	0.02
101	1 18	dH	0.000	-0.001	0.12
101	1 19	R	0.00014	-0.00032	0.03
101	1 19	D	0.001	-0.001	0.10
101	1 19	dH	-0.000	0.001	0.19
101	1 20	R	-0.00299	0.00655	0.58
101	1 20	D	0.001	-0.002	0.13
101	1 20	dH	0.001	-0.001	0.23
101	1 21	R	-0.00181	0.00490	0.25
101	1 21	D	0.001	-0.002	0.13
101	1 21	dH	0.001	-0.003	0.56
101	1 22	R	-0.00254	0.00712	0.35
101	1 22	D	0.001	-0.002	0.20
101	1 22	dH	0.002	-0.006	1.13
101	1 23	R	0.00018	-0.00044	0.02
101	1 23	D	-0.001	0.002	0.12
101	1 23	dH	0.004	-0.010	2.17
101	1 24	R	0.00077	-0.00184	0.09
101	1 24	D	0.000	-0.000	0.01
101	1 24	dH	0.001	-0.003	0.61
101	1 25	R	0.00154	-0.00860	0.11
101	1 25	D	0.000	-0.000	0.00
101	1 25	dH	0.004	-0.009	1.80
101	1 26	R	-0.00397	0.02275	0.29
101	1 26	D	0.002	-0.003	0.33
101	1 26	dH	0.004	-0.010	2.01
101	1 27	R	-0.00182	0.00536	0.07
101	1 27	D	-0.000	0.001	0.06
101	1 27	dH	0.005	-0.014	2.83
101	1 28	R	-0.02684	0.07569	1.01
101	1 28	D	0.000	-0.000	0.03
101	1 28	dH	0.003	-0.008	1.65
101	1 100	R	-0.00079	0.00104	0.26
101	1 100	dH	-0.016	0.017	4.83 *

Tabellverdi=3.44 (Student-t, f=69, alfa=0.0005)

OPPSUMERING ETTER TEST AV OBSERVASJONER:

Kategori	Ant.obs.	Akkumulert (%)
Test/Tabell < 1.0	142	89.87
1.0 < Test/Tabell < 2.0	1	90.51
2.0 < Test/Tabell < 3.0	0	90.51
3.0 < Test/Tabell < 3.0	0	90.51
Ukontrollerbar	15	100.00

STATISTIKK

Antall iterasjoner	:	2
Antall observasjoner retning	:	53
Antall observasjoner avstand	:	52
Antall observasjoner høydeforskjell	:	53
Antall observasjoner	:	158
Antall ukjente grunnrisskoordinater	:	60
Antall ukjente høydekoordinater	:	30
Antall ukjente orienteringsselementer	:	2
Antall tilleggsukjente	:	2
Antall ukjente	:	94
Rangdefekt	:	6
Antall ukjente korrigert	:	88
Antall overbestemmelser	:	70
Feilkvadratsum	:	176.97128547

Beregnet std.avvik p1 vektsheten 1.5900
 Antatt std.avvik p1 vektsheten : 1.0000
 Minst en ukontrollerbar observasjon er funnet

DOKUMENTASJON UTJEVNINGSBEREGNINGER

ADMINISTRATIVE DATA

Oppdrag : Project

DATUMPARAMETRE

System : local
 Lang halvakse [m] : 6377492.018
 Flattrykning [1/f]: 299.1528128500000
 Tangeringsmeridian [deg]: 0.000000000000
 Skalafaktor : 1.000000
 Addisjonskonst. nord [m]: 0.000
 Addisjonskonst. uest [m]: 0.000
 Rotasjon [deg]: 0.000000

INSTRUMENTPARAMETRE

INSTRUMENT : 1: EDM - 1

Std.avvik Konstantdel Avstandsavhengig
 Retning : 0.00120 gon 0.00000 gon/km
 Avstand : 0.005 m 0.005 m/km
 Hrydeforskjell : 0.000 m 0.020 m/km
 Sentrering Grunnriss : 0.002 m
 Sentrering Hryde : 0.002 m
 Referanseverdier
 Referansetrykk : 760.0 mmHg
 Referansetemperatur : 20.0 C
 Addisjonskonstant : 0.000 m
 Milestokkfeil : 0.000 m/km

DATUM: local

UTJEVNING I 3-D

TVUNGEN UTJEVNING

GITTE KOORDINATER [meter]

PUNKT	X	Y	H
100	100.000	100.000	100.000
101	168.856	100.000	

NYBESTEMTE KOORDINATER MED MIDLERE FEIL [meter]

PUNKT	X	Y	H	sX	sY	sH
1	103.360	104.431	101.218	0.005	0.005	0.003
2	103.335	104.439	99.171	0.005	0.005	0.003
3	103.320	99.851	99.168	0.008	0.003	0.003
4	103.317	99.858	101.159	0.008	0.003	0.003
5	109.785	105.155	101.211	0.011	0.007	0.004
6	109.772	105.151	99.179	0.011	0.007	0.004
7	109.787	99.459	99.173	0.012	0.004	0.004
8	109.804	99.465	101.210	0.008	0.003	0.003
9	119.821	103.973	101.583	0.012	0.005	0.004
10	119.793	103.995	99.278	0.008	0.003	0.003
11	119.855	99.435	99.119	0.008	0.003	0.003
12	119.842	99.438	101.134	0.008	0.003	0.003
13	129.579	103.927	101.538	0.012	0.005	0.005
14	129.666	103.527	99.269	0.008	0.003	0.003
15	129.444	99.403	99.154	0.008	0.003	0.003
16	129.430	99.405	101.177	0.008	0.003	0.003
17	141.362	103.889	101.587	0.008	0.003	0.003
18	141.327	103.479	99.286	0.008	0.003	0.003
19	141.382	99.393	99.173	0.008	0.003	0.003
20	141.377	99.397	101.195	0.008	0.003	0.003
21	152.145	103.832	101.579	0.008	0.004	0.003
22	152.230	104.305	99.137	0.008	0.004	0.003
23	152.750	99.358	99.174	0.008	0.003	0.003
24	152.743	99.363	101.216	0.008	0.003	0.003
25	164.472	104.316	101.116	0.006	0.004	0.003
26	164.463	104.314	99.095	0.006	0.004	0.003

27	164.472	99.300	99.107	0.008	0.003	0.003
28	164.434	99.295	101.123	0.008	0.004	0.003
101			98.807			0.001

KORRIGERTE OBSERVASJONER, ANTATT MIDLERE FEIL OG RESTFEIL [meter / gon]

Fra	Til	Observasjon	Antatt M	Restfeil	
100	1 1	R	58.72530	0.02289	-0.02719
100	1 1	D	5.558	0.005	0.003
100	1 1	dH	1.214	0.002	0.003
100	1 2	R	58.99350	0.02109	-0.01457
100	1 2	D	5.546	0.005	0.006
100	1 2	dH	-0.832	0.002	0.003
100	1 3	R	397.12070	0.03109	0.01267
100	1 3	D	3.313	0.005	0.010
100	1 3	dH	-0.836	0.002	0.004
100	1 4	R	397.27950	0.03817	0.00099
100	1 4	D	3.310	0.005	0.010
100	1 4	dH	1.154	0.002	0.005
100	1 5	R	30.86870	0.01157	0.00000
100	1 5	D	11.060	0.005	-0.000
100	1 5	dH	1.211	0.002	0.000
100	1 6	R	30.88100	0.01133	-0.00000
100	1 6	D	11.046	0.005	0.000
100	1 6	dH	-0.821	0.002	0.000
100	1 7	R	396.48330	0.01267	-0.00000
100	1 7	D	9.802	0.005	0.000
100	1 7	dH	-0.827	0.002	0.000
100	1 8	R	396.51420	0.01302	0.01301
100	1 8	D	9.811	0.005	0.008
100	1 8	dH	1.210	0.002	0.000
100	1 9A	R	12.59090	0.00641	-0.00000
100	1 9A	D	20.216	0.005	0.000
100	1 9A	dH	1.583	0.002	0.000
100	1 10	R	12.68230	0.00638	-0.00522
100	1 10	D	20.186	0.005	0.006
100	1 10	dH	-0.724	0.002	0.002
100	1 11	R	398.18670	0.00648	-0.00117
100	1 11	D	19.855	0.005	0.008
100	1 11	dH	-0.883	0.002	0.002
100	1 12	R	398.18850	0.00653	0.00429
100	1 12	D	19.841	0.005	0.009
100	1 12	dH	1.134	0.002	0.001
100	1 14	R	7.52970	0.00442	-0.00010
100	1 14	D	29.865	0.006	0.010
100	1 14	dH	-0.731	0.002	-0.000
100	1 15	R	398.70590	0.00447	0.00028
100	1 15	D	29.440	0.006	0.010
100	1 15	dH	-0.847	0.002	0.000
100	1 16	R	398.71020	0.00449	-0.00084
100	1 16	D	29.426	0.006	0.010
100	1 16	dH	1.175	0.002	0.002
100	1 17	R	5.96650	0.00329	-0.00121
100	1 17	D	41.536	0.006	0.008
100	1 17	dH	1.588	0.002	-0.001
100	1 18	R	5.34380	0.00329	-0.00037
100	1 18	D	41.464	0.006	0.009
100	1 18	dH	-0.714	0.002	-0.000
100	1 19	R	399.06260	0.00330	0.00004
100	1 19	D	41.376	0.006	0.010
100	1 19	dH	-0.827	0.002	0.000
100	1 20	R	399.07140	0.00330	-0.00221
100	1 20	D	41.371	0.006	0.011
100	1 20	dH	1.196	0.002	-0.001
100	1 21	R	4.66720	0.00272	-0.00028
100	1 21	D	52.276	0.006	0.010
100	1 21	dH	1.580	0.002	-0.001
100	1 22	R	5.23260	0.00271	-0.00054
100	1 22	D	52.397	0.006	0.010
100	1 22	dH	-0.860	0.002	-0.003
100	1 23	R	399.22240	0.00269	-0.00014
100	1 23	D	52.745	0.006	0.009
100	1 23	dH	-0.821	0.002	-0.006

100	1 24	R	399.22740	0.00270	0.00009
100	1 24	D	52.738	0.006	0.010
100	1 24	dH	1.218	0.002	-0.002
100	1 25	R	4.25140	0.00231	0.00107
100	1 25	D	64.601	0.006	0.015
100	1 25	dH	1.121	0.002	-0.005
100	1 26	R	4.25050	0.00231	0.00025
100	1 26	D	64.594	0.006	0.014
100	1 26	dH	-0.900	0.002	-0.006
100	1 27	R	399.30650	0.00231	-0.00091
100	1 27	D	64.466	0.006	0.010
100	1 27	dH	-0.886	0.002	-0.008
100	1 28	R	399.30330	0.00231	-0.00325
100	1 28	D	64.425	0.006	0.013
100	1 28	dH	1.128	0.002	-0.005
100	1 101	R	399.99150	0.00220	0.00524
100	1 101	D	68.845	0.006	0.011
100	1 101	dH	-1.184	0.002	-0.010
101	1 1	R	395.70020	0.00228	-0.00127
101	1 1	D	65.628	0.006	0.018
101	1 1	dH	2.416	0.002	-0.005
101	1 2	R	395.69320	0.00228	-0.00014
101	1 2	D	65.657	0.006	0.014
101	1 2	dH	0.368	0.002	-0.004
101	1 3	R	0.14360	0.00228	0.00126
101	1 3	D	65.525	0.006	0.011
101	1 3	dH	0.367	0.002	-0.006
101	1 4	R	0.13730	0.00228	-0.00001
101	1 4	D	65.528	0.006	0.011
101	1 4	dH	2.360	0.002	-0.007
101	1 8	R	0.57360	0.00247	0.00271
101	1 8	D	59.045	0.006	0.010
101	1 8	dH	2.403	0.002	-0.000
101	1 10	R	394.82910	0.00285	-0.00209
101	1 10	D	49.216	0.006	0.010
101	1 10	dH	0.473	0.002	-0.002
101	1 11	R	0.73440	0.00286	-0.00063
101	1 11	D	48.996	0.006	0.008
101	1 11	dH	0.315	0.002	-0.003
101	1 12	R	0.72820	0.00286	0.00196
101	1 12	D	49.007	0.006	0.010
101	1 12	dH	2.328	0.002	-0.001
101	1 13	R	393.65510	0.00344	-0.00000
101	1 13	D	39.473	0.006	0.000
101	1 13	dH	2.731	0.002	-0.000
101	1 14	R	394.28570	0.00345	0.00040
101	1 14	D	39.339	0.006	0.010
101	1 14	dH	0.462	0.002	0.000
101	1 15	R	0.96380	0.00345	0.00013
101	1 15	D	39.406	0.006	0.011
101	1 15	dH	0.347	0.002	-0.000
101	1 16	R	0.96150	0.00345	-0.00075
101	1 16	D	39.420	0.006	0.010
101	1 16	dH	2.372	0.002	-0.002
101	1 17	R	391.05470	0.00474	-0.00103
101	1 17	D	27.759	0.006	0.009
101	1 17	dH	2.780	0.002	0.001
101	1 18	R	391.99670	0.00474	0.00009
101	1 18	D	27.739	0.006	0.009
101	1 18	dH	0.479	0.002	0.000
101	1 19	R	1.40660	0.00478	-0.00006
101	1 19	D	27.471	0.006	0.010
101	1 19	dH	0.367	0.002	-0.000
101	1 20	R	1.39950	0.00479	-0.00320
101	1 20	D	27.475	0.006	0.010
101	1 20	dH	2.388	0.002	0.001
101	1 21	R	385.64790	0.00751	0.00073
101	1 21	D	17.135	0.005	0.009
101	1 21	dH	2.771	0.002	0.001
101	1 22	R	383.87000	0.00749	0.00027
101	1 22	D	17.165	0.005	0.010
101	1 22	dH	0.327	0.002	0.002
101	1 23	R	2.53570	0.00797	-0.00060

101	1 23	D	16.110	0.005	0.008	
101	1 23	dH	0.363	0.002	0.004	
101	1 24	R	2.51660	0.00798	-0.00001	
101	1 24	D	16.116	0.005	0.009	
101	1 24	dH	2.408	0.002	0.001	
101	1 25	R	350.47800	0.02062	0.01968	
101	1 25	D	6.148	0.005	0.005	
101	1 25	dH	2.305	0.002	0.004	
101	1 26	R	350.56040	0.02026	0.01363	
101	1 26	D	6.150	0.005	0.007	
101	1 26	dH	0.284	0.002	0.004	
101	1 27	R	10.09010	0.02752	-0.01153	
101	1 27	D	4.432	0.005	0.008	
101	1 27	dH	0.294	0.002	0.005	
101	1 28	R	10.10400	0.02819	-0.03686	
101	1 28	D	4.469	0.005	0.009	
101	1 28	dH	2.313	0.002	0.003	
101	1 100	R	0.00040	0.00220	-0.00068	
101	1 100	dH	1.209	0.002	-0.016	**

STATISTIKK

Antall iterasjoner	:	2
Antall observasjoner retning	:	53
Antall observasjoner avstand	:	52
Antall observasjoner høydeforskjell	:	53
Antall observasjoner	:	158
Antall ukjente grunnrisskoordinater	:	56
Antall ukjente høydekoordinater	:	29
Antall ukjente orienteringselementer	:	2
Antall ukjente	:	87
Antall overbestemmelser	:	71
Feilkvadratsum	:	330.23369432
Beregnet std.avvik på vektsheten	:	2.1567
Antatt std.avvik på vektsheten	:	1.0000